FEASIBILTY STUDY OF ELEMENTAL RECOVERY

FROM OKLAHOMA PRODUCED WATERS USING

ADVANCED MEMBRANE TECHNOLOGIES


By

MADELYN J. SHAW

Bachelor of Science in Civil Engineering

Oklahoma State University

Stillwater, Oklahoma

2020


Submitted to the Faculty of the
Graduate College of the
Oklahoma State University
in partial fulfillment of
the requirements for
the Degree of
MASTER OF SCIENCE
July 2022

FEASIBILTY STUDY OF ELEMENTAL RECOVERY FROM

OKLAHOMA PRODUCED WATERS USING ADVANCED

MEMBRANE TECHNOLOGIES

Thesis  Approved:

Dr. Mark J. Krzmarzick

Thesis Adviser

Dr. Clint P. Aichele

Dr. David J. Lampert

# ACKNOWLEDGEMENTS

Acknowledgements reflect the views of the author and are not endorsed by committee members or Oklahoma State University.

Name:        MADELYN J. SHAW

Date of Degree: JULY 2022

Title of Study: FEASIBILITY STUDY OF ELEMENTAL RECOVERY FROM OKLAHOMA PRODUCED WATER USING ADVANCED MEMBRANE TECHNOLOGIES

Major Field:    CIVIL ENGINEERING

Abstract:        Hundreds of millions of barrels of wastewater are produced by the oil and natural gas industry every year.  The disposal practices associated with these produced waters (PW) are unsustainable and linked to lowered standards of living in the communities impacted by them. Alternative treatment technologies are typically expensive and inefficient, but membrane distillation (MD) has the unique ability to operate with low-grade heat energy inputs and treat highly saline water to reusable levels with less breakthrough and fouling relative to traditional membrane technologies. A model was developed to predict MD flux values and optimize a system for maximized operational and economical benefit. A bench-scale system demonstrated flux while maintaining low conductivity measurements in the permeate tank, when operating with high-salinity PW solutions. Hydrocarbons and valuable elements solubilized in the PW could potentially provide revenue to offset MD costs. ICP analysis was used to characterize the PW, as well as to analyze the sorbent capacities of silica nanoparticles. Successful uptake by the nanoparticles of high value elements could allow for elemental recovery and reuse. Successful application of a silica-modified membrane relies of the silicas' ability to remain attached to the membrane surface but attempts at quantifying silica loss were indeterminate. ICP instrumentation and sample digestion solutions were analyzed to eliminate error associated with the data collection technique. Experimental results suggest MD has the potential to be successfully implemented on an industrial scale for the treatment of PW. Sorption data shows successful removal of heavier elements, some of which were found in PW samples.  Developing a system composed of a silica-modified inorganic pre-treatment membrane – to remove oil and salts – and a MD system  for further water purification could be an economically feasible treatment system capable of decreasing disposable waste and generating reusable water.

For additional information on referenced technologies and data sets, please refer to Section 1.1 Overview of OCAST Project, for list of project collaborators.

TABLE OF CONTENTS

**Chapter**                                                                                   **Page**

LIST OF TABLES

**Table**                                                                          **Page**

# LIST OF FIGURES

**Figure**                                                                 **Page**

CHAPTER I

INTRODUCTION

**1.1 Produced Water, Rare Earth Elements, and National Security**

In the United States, the Oil and Gas industry has played a large role within cultural and

socioeconomic contexts since the beginning of the oil booms of the eighteen- and nineteen-

hundreds. Millions of people nation-wide are employed by the industry, billions of tax dollars are

contributed by the industry annually, and fossil fuels still provided 69-percent of consumed

energy as of 2020[1,2]. Energy demands continue to rise and, to help maintain a high energy

independence index value, so does US crude oil and gas production[3].

In the early days of oil extraction, most oil was pumped from "conventional" wells. These oils are

liquid at atmospheric temperature and pressure, and the oil wells don't require specialized

technologies to stimulate. They're cheaper and easier to produce – and typically generate less

waste[4]. As conventional sources are depleted, the exploitation of "unconventional" oil sources is

relied upon to meet the rising energy demands. These crude oils are obtained from geologic

formations with such low permeability and porosity that it is not economically feasible to extract

them through a traditional vertical well[4]. Shale gas is produced from fine-grained sedimentary

"shale" formations of low permeability. It often contains high concentrations of petroleum products[5]. The shale oil boom since the early 2000s has led to a drastic increase in hydraulic fracturing and horizontal drilling activity across the United States[6], both unconventional oil techniques.

An unconventional oil well will consume millions of gallons of clean water over its lifespan[7], and will generate a wide array of sludge wastes including drilling fluids, fracturing fluid returns, and produced waters (PWs)[8]. The composition of PWs and other fracking fluids make them difficult and expensive to adequately treat with traditional treatment technologies[9]. PWs are waters located in the formation, either naturally or because of previous injection, that come to the surface with the hydrocarbons and trace elements[10].

In the United States, PWs represent the largest waste stream in the industry[11]. Over 24 barrels of produced oil are generated annually, with an average of almost 10 barrels of waste produced per barrel of oil[10], but can vary from almost 0 to a ratio of 54:1[11]. The most common method of managing oil and gas wastewaters in the U.S. is underground injection[12]. Injection wells are particularly useful in areas with porous, sedimentary rock. When wastewater is injected under a high pressure into these formations, the fluid is able to flow through and fill the voids and spaces, effectively and economically disposing of the unwanted byproduct[9]. However, these disposal practices are being linked to increased seismic activity[13] and other environmental concerns.

Rare earth elements (REEs) are extensively used in private and public sectors including energy, aeronautics, transportation, defense, and consumer electronics. The elements are mined from mineral deposits, which are then refined and processed into metal alloys[14]. There is a growing need as production continues to increase, with only a small number of countries contributing to the production of the resources. As the highly-profitable mineral deposits of REEs are depleted, it is necessary to find economically viable sources and production methods for their extraction to

prevent the collapse of the technology sector[15]. With only a small number of countries producing almost all the world's REEs, U.S. reliance on foreign resources and the difficulty of maintaining good trade relations is a major national security concern[16] (Figure [1]).
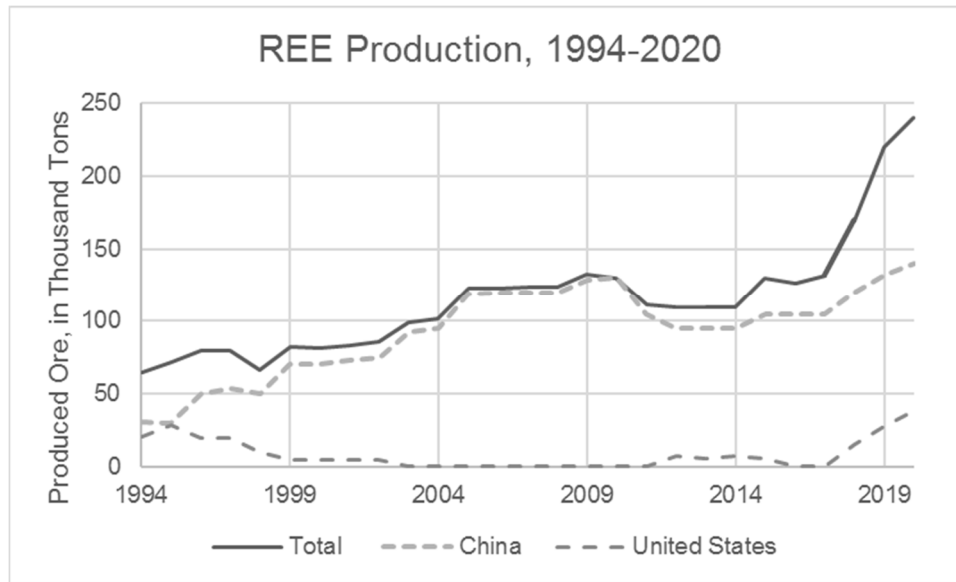


*Figure 1: Almost all REE's are produced from the US and China. Increasing demand of these valuable elements is a point of concern for a variety of industries as well as national security.*

Produced waters from many shale formations in the U.S. have been found to contain trace amounts of high-value metals and REEs. The absorption and recovery of valuable resources[17] from produced waters may provide an opportunity to turn produced water into a profitable and valuable resource, and may also lessen the amount of imported REEs needed in the U.S.

With increased concerns regarding the future of clean and accessible drinking water[18], the responsible handling of oil and gas waters and wastewaters has become a goal for state legislatures and research in the area is being conducted[19-21]. The profit generated from resource recovery may make it economically viable to further purify produced water, alleviating further concerns regarding the responsible management and handling of fresh water sources. Employing waste heat generated during the drilling process, a low-energy input membrane distillation (MD)

system may offer a cost-effective and environmentally responsible alternative to the injection of PWs[22].

## 1.2 Overview of OCAST Project

Increased oil and gas production have consequently led to a dramatic increase in the amount of produced water generated by the industry. Most of the water is treated as waste and is injected into underground reservoirs. Links to increased seismic activity, coupled with water shortages and other issues, make purification and reuse of produced water a potentially lucrative and more sustainable alternative practice (Figure [2]). Additionally, produced water streams can contain valuable elements and metals that can potentially be recovered, further increasing the benefits of a produced water separation system.
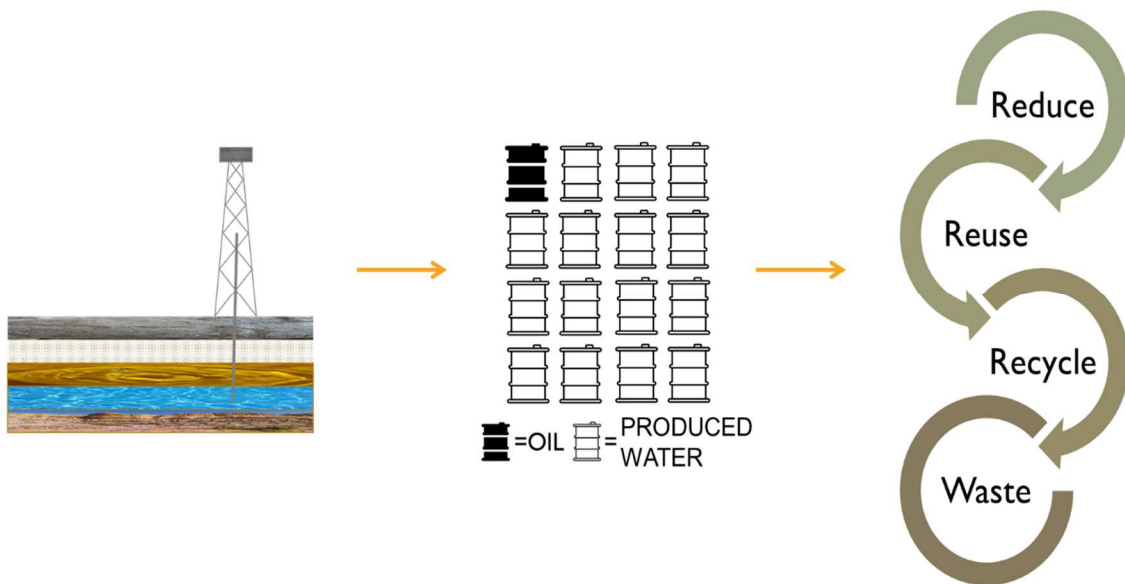


*Figure 2: Unconventional drilling methods produce large amounts of wastewater. Current disposal methods exhibit many social, economic, and ecological concerns. Research is developing ways to decrease waste by-products and improve industry sustainability.*

Working from a grant endowed by the Oklahoma Center for Advancement of Science and Technology (OCAST), a team of Chemical Engineering and Environmental Engineering researchers from Oklahoma State University and Illinois Institute of Technology attempted to

develop a produced water purification system. The two-part system consists of a silica-modified, inorganic absorption membrane, and a direct contact MD system. The inorganic membrane aims to separate residual oil from the produced water stream while the attached silica nanoparticles selectively capture elements on the membrane surface. Both processes potentially yield lucrative retentate streams. The MD unit aims to reduce concentrations of solids to more treatable or reusable levels, drastically reducing the waste stream injected into subsurface formations.

MD was studied under the guidance of Dr. Mark Krzmarzick and Dr. David J. Lampert with the Oklahoma State University Department of Civil and Environmental Engineering. This project was in collaboration with Dr. Clint Aichele and Dr. Seokjhin Kim, both with the Oklahoma State University Department of Chemical Engineering. Research on the separation of oil and water using advanced membrane technologies was conducted by Anirban Ghosh and Diako Mahmodi under the counsel of Dr. Kim and Dr. Aichele. Dr. Aichele further oversaw the sorption experiments, which were designed and conducted by Anirban Ghosh, Michael Miranda, and Songpei Xie. For more information on referenced technologies and results, please refer to related publications by the aforementioned authors.

CHAPTER II

REVIEW OF LITERATURE

## 2.1 Fouling Potential and Characteristics of Sorption Membrane

Membrane processes for the separation of oil and water emulsions have been widely applied to produced water treatments. They have significant advantages over traditional treatment methods— notably high removal efficiency coupled with lower operating costs and energy requirements[23]. High concentrations of salts and dissolved organic matter found in oil and gas wastewaters do make the membranes more prone to fouling[24], thus a membrane with anti-fouling properties may be a feasible way to optimize a membrane system constructed to treat produced water.

Fouling happens when rejected contaminants from the influent flow accumulate on the membrane. Fouling can occur both on the surface or within the pores of the membrane. Contaminants may be organic, inorganic substances, and biological substances. Membrane design and material, as well as the matrix of the feed stream, affect the type of fouling occurring on the membrane, as well as dictate what treatment methods are available to remediate the membrane. If left unaddressed, fouling can over time lead to drastic decreases in flux and[1,2] an increase in membrane pressure. In addition to decreasing system efficiency and increasing operating costs, it also leads to inadequately treated effluent flows and eventual membrane failure[25,26].

Fouling consists of two main parts: pore blockage and the formation of a layer of contaminants

6

on the membrane surface. While pore blockage occurs because of physical properties of the contaminant and the membrane— the size and shape of the contaminant and the membrane pores— the formation of the contaminant layer occurs through physiochemical means. Under neutral conditions, the foulants adhere together through Van der Waals interactions; this forms a small charge. Surface charges present on the membrane surface can interact with the particles to form electrostatic repulsions[27,28]. Fouling can be both reversible and irreversible, with organic fouling and biological fouling typically being more difficult to fully remove[25]. Even with adequate anti-fouling measures, permanent loss in flux has been reported at values as high as an 80 percent decrease[29]. Hydrophilic membranes are less susceptible to fouling under most conditions than hydrophobic counterparts[27,30].

Fouling associated with biological growth and accumulation can lead to the formation of a biofilm, as microbial cells are provided required nutrients and oxygen as the feed solution permeates through the membrane[31]. Biofilms are characteristically more resistant towards environmental stressors, including temperature, pH, and chemical fluctuations. Biological communities must be fully removed to prevent further adaptations and cellular growth on the membrane. This makes biofouling especially challenging to remediate; in addition to causing a severe flux decline, treatment options capable of removing the contamination often lead to severe damage of many membrane materials[29,32,33].

### 2.11 Ceramic Membrane Treatment of Produced Water

The complexity of produced water makes it difficult to treat economically and efficiently. High concentrations of petroleum byproducts and inorganic salts leave membranes more susceptible to organic fouling. Under conditions found in briny feed solutions, the physiochemical interactions occurring between ions changes. Increased fouling and the consequential decrease in permeate flux has been observed in membrane systems while operating with a feed solution containing elevated ionic strength levels[28,34]. The highly charged feed solution weakens the bilayer

electrostatic repulsion and forces acid-base interactions between particles – interactions which are highly susceptible to changes in pH and salt concentration[34–36]. With decreased electrostatic forces, foulants are able to more easily and more densely deposit on a membrane surface[28]. The accumulation of foulants blocks membrane pores and leads to a decrease in permeate flux[37]. PWs can further exacerbate these qualities. Hydrophobic contaminants, such as hydrocarbons contained in produced water, can form a strong bond with the hydrophilic membrane surface, blocking the membrane pores and resulting in a more severely fouled membrane and a large decrease in flux[36,38,39].

Membrane materials and characteristics play a key role in the operational capabilities of membrane systems. The properties of ceramic membranes remediate the issues of chemical and thermal instability that can be caused in a membrane system exposed to high salt and organics concentrations contained in PWs. Though typically reported to be more susceptible to fouling[30], the controlled pore size range and chemical selectivity make them less prone to irreversible fouling with higher reported solids and oil rejection values. Similar to polymeric membranes, ceramic membranes are prone to pore blockage fouling in the presence of oily substances[40]. Though it still decreases the life expectancy of the membrane[40], the physical compositions of the membrane components allow for harsh anti-fouling procedures to be applied that would damage a polymeric membrane[29,41]. Ceramic membranes may be chemically modified to further enhance the membranes' capabilities. Attaching specific polymers and compounds allows for more selective permeability and enhanced oil rejection[40]. Modifying the membrane can also allow for the selective absorption and recovery of pollutants and high-value elements and heavy-metals[17], further improving both effluent water quality and economic feasibility of the system.

In addition to water, hydrocarbons, and trace elements, PWs are also composed of diverse communities of microorganisms. Typically thermo- and halophilic in nature, these bacteria are linked to pipeline corrosion, oil well souring, and membrane biofouling[32,42]. Membrane material

is a pivotal choice in the prevention of the accumulation and growth of microbes on the membrane surface. Unlike polymeric membranes, ceramic membranes can withstand the use of high-temperatures and harsh chemicals for membrane cleaning, making it possible to employ the treatment technologies necessary for the removal of biological fouling[29,43].

## 2.2 Silica Retention on Modified Inorganic Membrane

An aim of the OCAST funded project is to develop a silica-modified membrane capable of extracting high value elements from the concentrated brine of an inorganic, hydrophilic membrane. It is also hypothesized to aid in the separation of water and oil emulsions within produced water samples. Silica is extremely insoluble in water and is thus very hydrothermally stable. When chemically adhered to and treated to a gel on a membrane, it maintains a malleable surface that allows for high control of pore size and flux[44]. These nanoparticles, and additionally the hydrophilicity of the membranes' surface, allow for high control and selectivity of what is rejected by and what ions and compounds pass through the microporous channels. In addition to its potential ability to optimize the efficiency of the membrane process, silica is intrinsically non-toxic, and will be less likely to significantly contribute to human or environmental contamination[45].

Heavy metals have been proven to be toxic to ecosystems as well as human health[46,47]. Increased industrial activities have resulted in a concurrent increase in the concentrations of heavy metals found within surrounding environments. Traditional means of removal have been found to have adverse health effects[48] and high operating costs, thus bioremediation and detoxification of heavy metal contaminated sites is a point of interest[49,50]. Functionalized silica has been shown to facilitate and increase the rate of heavy metal adsorption in biological systems[50]. Similar studies have shown that the inorganic and hydrophilic properties of a silica-modified membrane can improve the efficiency of oil and water separation in acidic and salty brines[51,52], conditions similar to those found within many PWs[8].

Silica is found abundantly in nature. It makes up a large percentage of Earth's crust and can exist in crystalline and amorphous forms[53]. Chemical reactions between water and rock results in weathering - silica dissolves into passing water streams. These groundwater sources contain concentrations of silica ranging from 1- to 30-mg/L[54]. At naturally occurring concentrations, silica is non-toxic to the environment and human health[50]. Higher levels of exposure to crystalline forms of silica via inhalation can lead to a decline of respiratory health and are linked to an increased risk for lung cancer[53]. The dissolved forms of silica primarily found in water sources, as well as low-concentrations of solid forms, has no indication of asserting these risks[45].

As the social need and industrial applications for silica continue to increase[55], several threats to the economy and the environment are posed. There is a limited supply of sand, aggregate, and quartz suitable for industrial purposes available for extraction[56,57]. Any loss of silica from membrane runoff results in a decrease in the available global supply, potentially increasing demand and costs[58]. A large percentage of the United States' quartz supply is import dependant[56], making preservation of silica resources a potential point concern regarding national security. An increased concentration in silica in a water source poses an additional hazard for water treatment facilities downstream. In higher concentrations, silica can scale pipes and equipment[54], and can irreversibly foul treatment membranes, increasing energy and treatment costs as well as decreasing the life expectancy, effectivity, and overall sustainability of the membrane treatment method[59]. Unlike organic counterparts, the high melting point of silicon makes it impossible to burn off build-up[60] from the membranes, leaving even an inorganic water treatment membrane at risk.

Studies using nanocomposite membranes have shown nanoparticles may potentially leach from the membrane's surface[61,62]. This ultimately yields in a permanent reduction in absorption capacity of the modified membrane. This renders any modifications obsolete and results in an unexpected influx of silicon into the permeate water flow[62]. The final effluent flow quality will

display a decrease in quality over time as well as a decreased concentration of waste within the retentate flow. Decreased silica attachment on the surface of the membrane can also potentially render the membrane more susceptible to fouling and damage, as a decreases in flux and antifouling abilities have been observed[63]. Careful incorporation of nanoparticles into the membrane's matrix can help improve dispersion and prevent agglomeration and leaching[63,64]. In addition to the chemical mechanism used to attach nanoparticles to a membrane's surface, additional factors contribute to the amount of nanocomposite material leached from the membrane. Membrane pore size, particle diameter[61], pH, influent solution matrix, and lapsed time[65] have all been shown to affect the amount of nanoparticle runoff occurring in a membrane system. Though small amounts of leaching may be expected at the initial onset of the membrane system[64], continuing and indefinite loss of nanoparticles overtime increases treatment cost and negatively impacts surrounding environments.

*2.21 Inductively Coupled Plasma-Optical Emission Spectrometry*

Decades of research culminated with the introduction of Inductively Coupled Plasma-Optical Emission Spectrometry (ICP-OES) in the 1970s. Since then, it has become one of the premier methods for the determination of trace inorganics over a wide range of sample types and matrixes[66]. ICP-OES uses high energy atoms generated by a plasma torch to collide with atoms found within the analytical matrix. The atoms react by reaching an excited electron state. When cooled back down, the atoms release a wavelength characteristic for its given element. An ICP-OES instrument is able to record and interpret the wavelengths detected into a concentration[67]. Though other atomic absorption methods can be used for trace metal analysis, using ICP-OES instruments offers several advantages and benefits which distinguish it from its peers[67–69]:

- They can simultaneously and sequentially analyze a wide range of elements and many samples.

- They have a wide linear region of analytical curve. This allows for samples spanning a large range of concentrations to be measured sequentially.

- They have low concentration limits and a large concentration range. Most elements have detection limits ranging from <10 parts per billion up to parts per million.

- Heavier metals, such as rare earth elements, can be accurately measured with high precision.

- Samples with high concentrations of dissolved solids can be measured due to the low number of interferences. This makes it possible to analyze wastewaters and digested samples with more complex matrixes.

These functions are achieved primarily through the high temperature of the plasma—estimated at over 8000 Kelvin—as well as other characteristics of the plasma itself. An ICP-OES instrument is composed of five primary units[68,70]: the sample introduction, a light source, a spectrophotometer, a detector, and a data processor (Figure [3]).
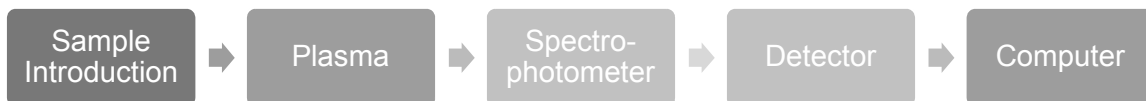


*Figure 3: Process flow diagram for ICP-OES instruments. They are composed of five major systems that operate sequentially.*

The sample introduction system transports the selected sample into the main part of the instrument, where the nebulizer converts the liquid into an aerosol. Most ICP-OES instruments use a pneumatic nebulizer, which uses a high-speed, high-purity argon gas flow to create the aerosol. The sample is introduced to the nebulizer using a peristaltic pump, which minimizes sample contact and decreases risk of contamination[71]. Due to the small size of the tubing and nebulizer, blockages can easily occur if inadequate measures are taken during sample preparation and routine instrument maintenance[72]. This leads to performance and data verification problems, resulting in data having to be discarded and samples having to be remeasured. This can be

avoided by careful sample preparation as well as the selection of a sample digestion method and dilution factor that is proper for the matrixes of the samples.

After nebulization, the sample moves to the plasma, where it is de-solvated and vaporized into individual atoms. Even after nebulization, many droplets are still too large to be injected into the plasma. A spray chamber—placed between the nebulizer and the plasma torch—reduces the influent sample by about 95 percent. Only droplets of >10-microns pass through to the plasma torch. The rejected sample is sent to waste[71].

The plasma torch in an ICP-OES instrument is composed of three quartz tubes that carry the plasma flow, the auxiliary flow, and the nebulizer flow (Figure [4]).

A - Sample Flow (~1 L/min)

B - Auxillary Gas Flow (~1-3 L/min)

C - Cool Gas (Argon) Flow (~7-15 L/min)

D - Radio Frequency Field

E - Induction Region (~10,000K)

F - Preheating Zone

G - Initial Radiation Zone (~8,000K)

H - Normal Analytical Zone (~6,800K)
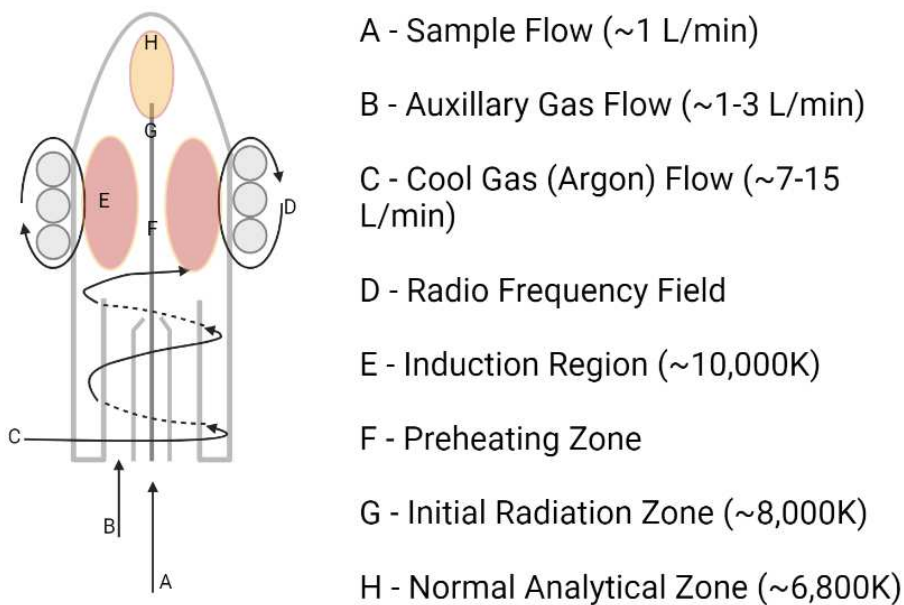
*Figure 4: Schematic diagram of an ICP plasma torch.*

The plasma flow spirals tangentially up and around the auxiliary tube, protecting the outer tube from melting[70]. Between the coolant and the nebulizer flow, the auxiliary flow exists to make sample aerosol introduction to the spectrophotometer easier by pulling the bottom of the plasma away from the injector tube[70,71]. The nebulizer flow contains the aerosol sample and is injected into the plasma through the center of the torch[71].

13

Plasma generation occurs when the argon is introduced to the torch coil by the plasma flow. An electric current is applied to the tip of the torch tube, which creates an electromagnetic field. The field ionizes the argon gas flow. The electron density is high, with the plasma reaching temperatures up to 10,000K[68].  After entering the plasma torch, the ionized atoms from the nebulizer flow are brought to an "excited" electron state due to the high energy of the surrounding system. As the atoms cool down to their "ground" state, they emit radiation as photons. The wavelength emitted by the photon is dependent upon what element it is, with each element having a characteristic wavelength[67] (Figure [5]).
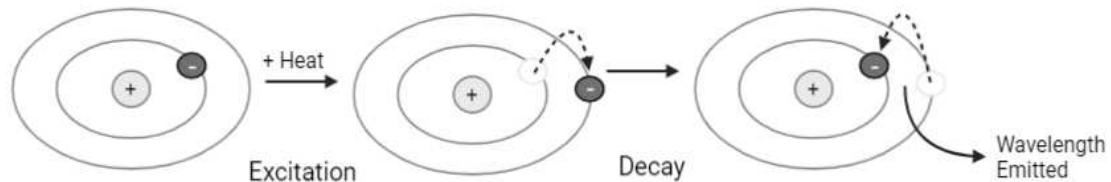


*Figure 5: Elemental atoms are ionized and are heated to an excited electron state in the plasma torch. As the atoms cool, they emit radiation at a characteristic wavelength which is then detected and translated to a concentration by the detector and computer*

The instruments detect and sort the present wavelengths. Most systems' spectrometers use a diffraction grating to disperse the different wavelengths[71]. Diffraction gratings are a series of lines etched onto the surface of a mirror. For ICP-OES instrument operations, this is generally between 600-4200 lines per millimeter. Since only waves of a certain length can be conserved in an associated line, all other wavelengths are destroyed via inference with each other[71]. This allows for the multi-elemental, polychromatic beam emitted from the torch to be separated into constituent wavelengths. Though most useful wavelength emissions for ICP-OES instruments lie between 190 and 450 nanometers, several common emissions lie outside of this threshold. The addition of a "purge gas", usually nitrogen, is necessary to deprive the system of air molecules, as electromagnetic radiation between 160 and 190 nanometers can be consumed by oxygen atoms[71].

Since the mid-1990's, the predominant systems use a solid-state charge transfer device (CTD)—either a charge injection device (CID) or charge coupled device (CCD)—that is designed using an echelle polychromator optical system[70,73]. These systems use multiple optical components. Relative to the traditional diffraction grating, echelle grating has a courser etching pattern that pick up a larger and overlapping spectral window. A second optical unit, either a prism or a second grating with a narrower dispersion, is set up perpendicular to the echelle grating. This unit individually resolves the multiple, overlapping wavelengths by measuring the diffraction order[71,74]. The spectrometer sends photons of a given wavelength to the detector.

The high-order and -resolution processing of the wavelengths warranted by the echelle optical system is often commercially paired with CTDs[71]. A covalent framework of crystalline silicon is used to grow a layer of Silicon dioxide. When the photons of an appropriate wavelength enter the silicon crystal lattice, Si-Si bonds are broken, and an electron is released. This forms a hole in the lattice, called an electron-hole pair[71]. A voltage is applied across the CTD, causing the free electrons to move towards the Silicon dioxide insultation and the electron-holes to move away from the Si-Silicon dioxide interface, leaving a proton depleted area in the structure. The increase in light wavelengths absorbed by the silicon is proportional to the number of electron holes formed. This leads to increased movement of electrons towards the Silicon dioxide, where they are captured on the interface[71](Figure [6]).
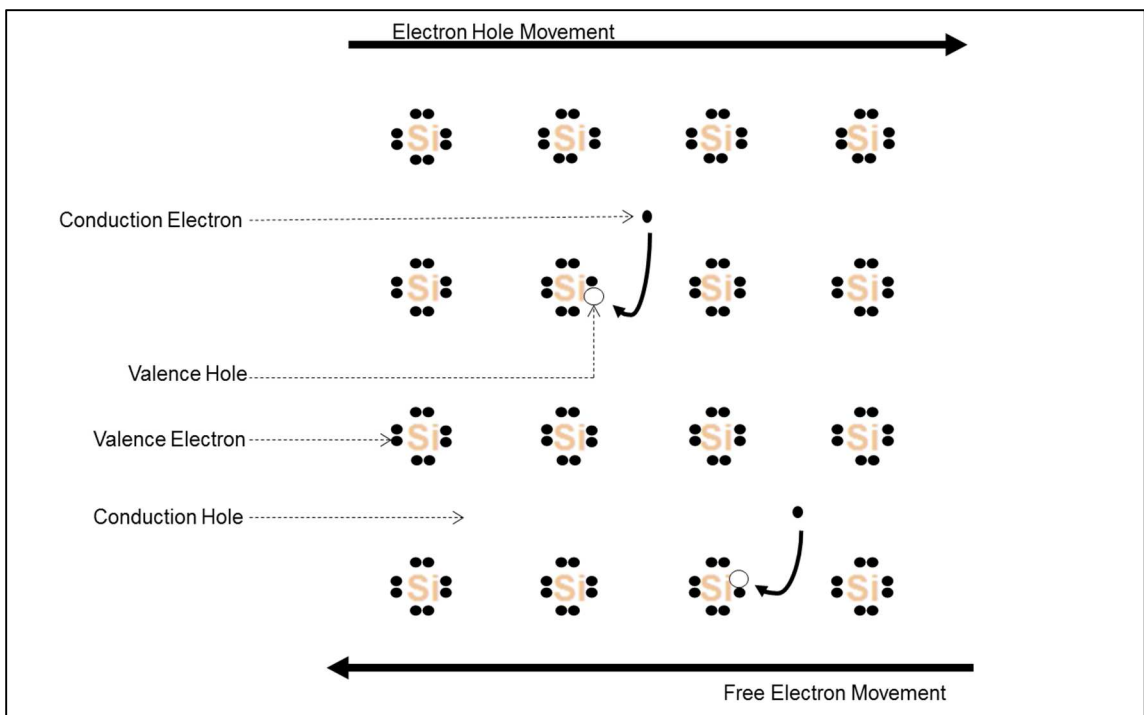
*Figure 6: Electron movement within a Charge Transfer Device (CTD). CTDs can quickly detect and capture electrons onto pixels, which can be converted into a concentration by a computer program.*

One variation of CTDs is the CID, where the high-speed, solid-state microprocessors can detect and read the amount of captured electrons on pixels[70,71]. Each pixel is randomly observed to see the amount of charge that has been collected over time and is then stored on the processor. There are over 250,000 pixels on commercially available detectors, which allows for the detection of wavelengths from 160-900 nanometers, covering the full applicable range of ICP-OES insturments[70,71,73]. As the read-out mode on a CID is non-destructive, there is a relatively large amount of background noise and spectral interference. This can be corrected after data extraction is completed. CCDs work in a similar manner, though there is inherently less background noise due to the nature of the data being destroyed after it is sequentially collected[71].

After the elemental concentrations are determined by the instrument, the results are sent to computer software specially developed to translate the data from the instrument to the analyst. In addition to being able to view the data, the analyst typically controls basic operation features from the software, including power switches, method and sample development, and data manipulation

and interpretation[70]. The system and software work harmoniously to give precise and accurate results of low concentration inorganic analytes.

*2.22 Silica Characteristics and Measurement in Solution*

Traditionally, electrothermal and colorimetric methods were used in the determination of silica concentrations in a liquid sample. However, these procedures can only be used when the dissolved silica occurs at higher concentrations and there are large possibilities for error when confronted with more complex matrixes[75]. An inorganic nonmetal, Standard Method 3120 Metals by Plasma Emission Spectrometry, can be successfully applied for silica detection in cases of lower concentrations and with less interference than other specified silica measurement techniques as specified in *Standard Methods* Method 4500A[75].

Silicon is not found in its free form in nature. It is most commonly found in its crystallized form – $SiO_2$ – and typically exists in aqueous systems as Silicic acid – $Si(OH)_4$[76]. The primary naturally-occurring dissolution reaction[77] for silica in water is seen in Figure [1].

$$SiO_2(s) + 2H_2O(l) \leftrightarrow H_4SiO_4(aq) \qquad\qquad [1]$$
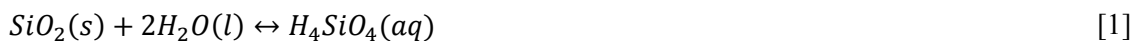
This reaction is only thermodynamically favorable at high temperatures and is minimally influenced by pressure flunctuations[77]; at ambient temperatures, silica oxide is extremely insoluble in water[76].

Silica dioxide's insolubility stems from its large covalent network (Figure [7]). Each silica ion is bridged by an oxygen atom. The energy required to break an Si-O bond is estimated at 452-kJ/mol[78], making it a very stable bond. Any available attractions in water and organic solvents are too weak to overcome the covalent bonds within the structure.

| Bond | Energy (kJ/mol) |
|------|------------------|
| Si-O | 452 |
| H-O | 430 |
| Si-H | 293 |
| H-Cl | 431 |
| Si-Cl | 417 |
| H-F | 570 |
| Si-F | 576 |
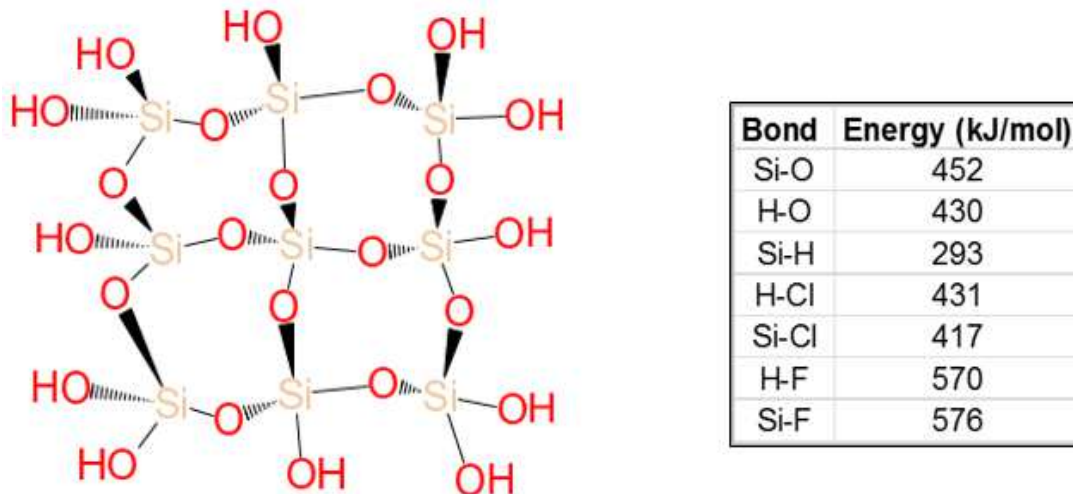
*Figure 7: The lattice pattern of Silica dioxide makes it extremely insoluble. Hydrofluoric acid can be used to solubilize the compound as the Si-F bond is one of the few bonds stronger than the Si-O bonds.*

Even bond energies of acids commonly used for digestion methods, most notably Hydrochloric acid, are too low to cleave the Si-O bond. On the other hand, Si-F has the highest single bond dissociation energy found in nature, predicted at 576.4-kJ/mol[78]. By reacting a sample containing silica dioxide with hydrofluoric acid, the thermodynamically favorable product is silica tetrafluoride[79](Equation [2]). This is a very stable aqueous product.

$$SiO_2 + 4HF \rightarrow SiF_4 + 2H_2O \qquad\qquad\qquad [2]$$

Hydrofluoric acid can be introduced to samples to force the silica dissolution reaction[79]. Due to the highly reactive nature of Hydrofluoric acid on glass and organics, Nitric acid and Perchloric acid must first be introduced to the systems to safely remove organics and excess fluoride ions from digested samples. This protects both human health and equipment mechanics. Guidance for Nitric acid-Perchloric acid-Hydrofluoric acid digestion can be found in *Standard Methods Method 3030I*[75].

Due to the multi-optics setups of most modern ICP-OES systems, a method may be designed to view the plasma "axially", where a mirror looks down the length of the plasma's axis, or "radially", where the optics are set up perpendicular to the longitudinal axis of the plasma. Since

this causes a decrease in the amount of light being analyzed and thus a decrease in sensitivity, it also yields less background noise and matrix interference[80]. Due to the high potential for matrix interference introduced by the acid digestion method, a radial view is recommended when determining the concentration of silicon[81]. Determined detection limits for silicon from one instrument to the next vary drastically, ranging from four parts per billion[75] to about one part per million[81]. Variation can occur from both discrepancies in instrument age, make, and model, as well as variations in experimental design and sample preparation procedures[81,82]. Proper instrument handling and maintenance as well as careful experimental design helps ensure collected data falls within the bounds of a given experiment's detection limits[82].

The ability of hydrofluoric acid to react so readily makes it a potentially dangerous substance to work with. It is highly corrosive and quickly damages cells and tissues, causing potentially serious long-term damage to skin, lungs, eyes, and internal organs. Overexposure can even result in death. To avoid accidental exposure, experimental work with Hydrofluoric acid should be done under a working fume hood and with proper personal protective wear in place, including long pants, closed toed shoes, a lab coat, an acid apron, neoprene glove, and safety goggles, while hair should be tied back. Additionally, a lab spill kit stocked with calcium gluconate for skin spills and an inorganic salt neutralizer for general spills should be easily locatable in the lab[83].

## 2.3 Membrane Distillation for Treatment of Produced Waters

Management of industry produced wastewater is a growing concern related to oil and gas extraction[8,84]. Much of the wastewaters produced during hydraulic fracturing, at volumes of over 21 billion barrels per year, are injected into deep subsurface formations[10]. Evidence correlating fracking with increased seismic activity[13], growing concerns regarding the global clean water supply[18], and limited industry availability of water in the arid regions often home to drilling operations[85,86], contribute to increased research activity for produced water reuse. Cleaned waters can be reused at the beginning of the production process, decreasing the amount of freshwater

required to drill a well— over 65 billion gallons in 2011 and 2012 alone[86]—as well as potentially being used for direct discharge, irrigation, or industrial applications[85].

In accordance with the Clean Water Act[87], management practices for oil and gas waste are mostly dictated by local and state guidelines, with minimal regulation in regards to federal mandates concerning discharge and irrigation permits. To be reused in drilling processes, waters must be desalinated or diluted prior to reinjection. In states where treated PWs have been approved for irrigation, discharge, or other direct potable reuse purposes, which is currently limited to a small but growing number of states[19,88], waters must be purged of any potentially harmful contaminants and adhere to set water quality standards. The high treatment costs associated with removing these high amounts of contaminants is the primary hindrance for increased development and implementation of treatment technologies.

MD is a treatment technology emerging as a forerunner for the treatment of produced water[84]. After adequate pre-treatment optimizing organic removal, MD can effectively treat water of virtually any salinity. The removal of organics and potential retrieval of high-value elements achieved by the silica-modified inorganic membrane used prior to the MD unit is expected to provide both adequate pretreatment and a profit source by which to increase economic viability.

## 2.31 Membrane Distillation Overview

Like most membrane processes, MD relies on a pressure gradient to drive the forward movement of influent liquid. The pressure gradient is driven by a temperature difference between the warm feed flow and cooled permeate. Vapor pressure is allowed to pass through the microporous membrane, leaving behind ions and other rejects. The vapor condenses on the surface of the hydrophobic membrane on the cooled permeate side[89] (Figure [8]).
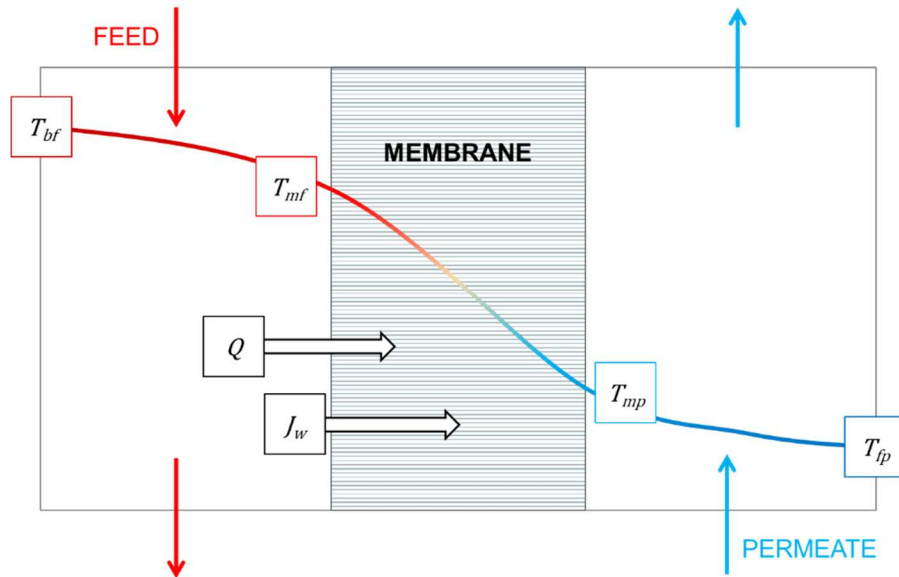
*Figure 8: Membrane Distillation diagram displaying heat and mass transfer mechanisms across the membrane*

Lower operating pressures and a decrease in required input heat energy makes MD more cost effective than traditional membrane operations. Further, due to the minimal chemical interactions occurring between the membrane surface and the feed solution compared to other distillation techniques, more robust materials can be used for the membrane, making it less susceptible to fouling and wetting[89]. This improves the usability and economic benefit when applied to feed flows with more robust matrixes.

The transport mechanism of MD relies on the simultaneous occurrence of heat and mass transfer phenomena. The concurrent occurrence of the two phenomena makes experimental determination of specific values difficult[90].

### 2.32 Driving Mechanisms of Permeate Flux and Dusty-Gas Model

The transport mechanism of MD relies on the simultaneous occurrence of heat and mass transfer phenomena. The concurrent occurrence of the two phenomena makes experimental determination of specific values difficult[90]. Heat transfer plays a large role in the overall permeate flux

occurring across the system, with temperature playing the most significant role in system efficiency[90], ousting even flow rate, feed concentration, and operation time.  Mass transfer in MD is expressed by both convective and diffusive water transport models. Though the vapor pressure gradient drives the mechanism forward, membrane and system characteristics can potentially resist the mass transfer[91,92].

The Dusty-Gas Model (DGM) is used to  describe the transport of multi-component fluids through a porous membrane[89,93] and can be useful for predicting the permeate flux in DCMD systems. It consists of the following models, when applied to MD:

- The Knudsen diffusion model (Figure [9A])—Favored in membranes with pores less than 0.5-$\mu$m[93], this model is used when the free path of the molecules is larger than the diameter of the capillary. In this case, the likelihood of molecular collision with the membrane wall is greater than that of molecule-molecule collision

- Poiseuille's Law or Viscous flow theory(Figure [9B])—the partial air pressure occurring in the systems maintains a constant pressure across the membrane; degassing the feed and permeate flows increases membrane permeability by concurrently decreasing the molecular diffusion resistance and increasing viscous flux[89]

- Molecular diffusion transition (Figure [9C])—represents the movement of the molecules from a region of high concentration to a region of low concentration due to the present pressure gradient. This is the preferred model in MD when collision between molecules is more likely than the collision of a molecule and the cell wall[89,90].
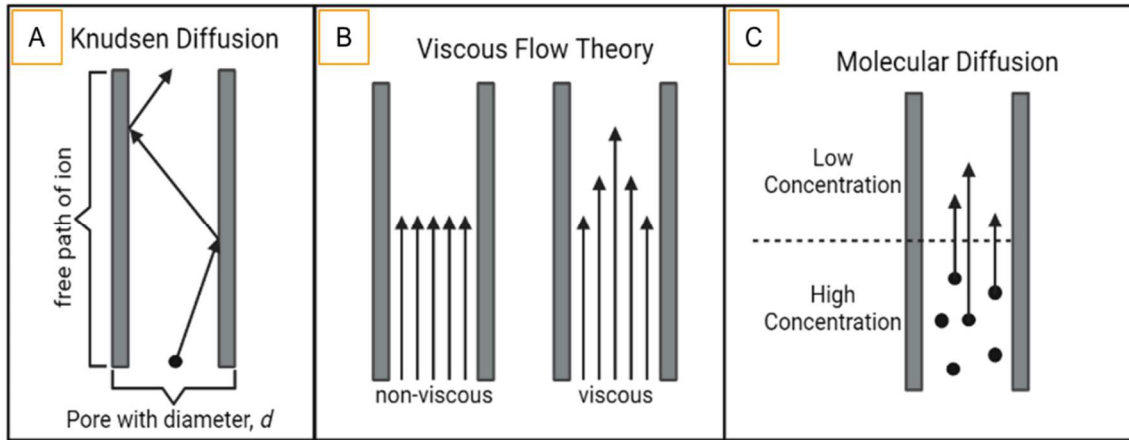
*Figure 9: The Dusty-Gas Model describes the transport of fluids through a membrane through a combination of three transition models.*

Though surface diffusion is factored into the DGM for most applications, it has been found to have no significant impact on the flux rates of DCMD systems and is thus not factored into any developed models[37,94].

In Direct Contact Membrane Distillation (DCMD), two boundary layers exist on the feed side and permeate side of the membrane. Though the permeate boundary layers mass transfer value is assumed to be one, the boundary layer on the feed side of the membrane also has a notable mass transfer value. Film theory is used to quantify the resistance across the boundary layer, where it is assumed that all the mass transfer that is going to happen occurs on a thin film at the interface[93,95] (Figure [10]). The mass transfer coefficient is dependent on which of these conditions are prevalent in the system and can differ drastically based on applied temperature, pressure, membrane characteristics, and operational conditions[92].
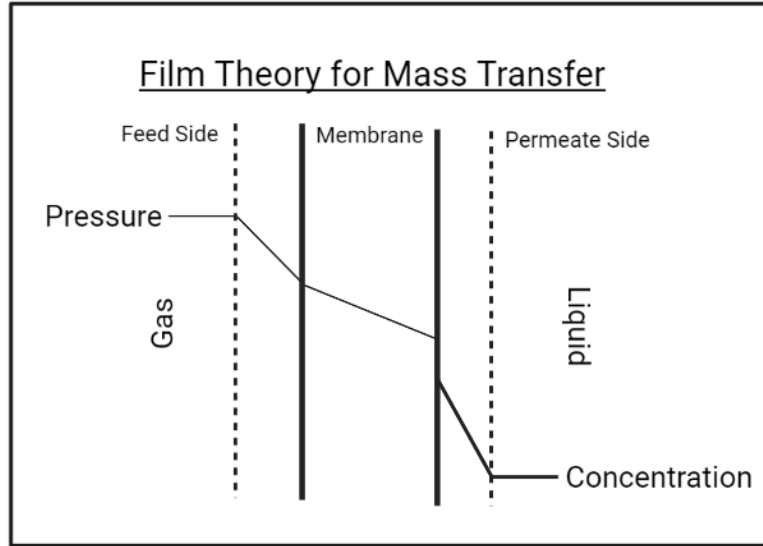
*Figure 10: Film theory is used to describe mass transfer across the membrane. It assumes the mass transfer phenomena shown in Figure [9] all occur across a thin "film" across the interface of the membrane.*

Like mass transfer, heat transfer for DCMD can be divided into three regions, consisting of the two boundary layers and the membrane. The boundary layers exists due to the temperature gradient[91,93]. Each region has convectional heat transfer due to the applied heat and heat transferred across the region due to the simultaneous mass transfer occurring. Heat transfer plays a large role in the overall permeate flux occurring across the system, with temperature playing the most significant role in system efficiency[90], ousting even flow rate, feed concentration, and operation time.

### 2.33 Model Development and Applications

The DGM can be built in any statistical computing coding language. Construction of an accurate model relies heavily on correct implementation of an extensive amount of input variables and constants (Figure [11]).

*Figure 11: The Dusty-Gas Model requires System Inputs that include membrane characteristics and experimental variables. Using programmed data, the model then algorithmically computes outputs relevant data.*

The output values can be graphed in various configurations and allow for the manipulation of multiple input parameters. This allows for graphical analysis for optimized permeate flux conditions, all without extensive bench-scale testing. Though bench-scale systems are helpful, running an experiment to obtain the flux values can be time consuming and expensive, thus the ability to change temperature, flow rate, and even membrane parameters drastically aid in research efforts.

The bench-scale system is still valuable for model validation. Comparing modeled results against measured results helps determine the accuracy and ensuing reliability of the model outputs. They are also useful for the development of model uncertainty as the independent input variables can be measured over the course of the experiment, providing the range of values necessary for the modeling methods.

### 2.34 Distillation Membrane

Membrane design and selection plays a large role in overall system performance. The matrix of the feed solution as well as desired operating temperature, cost considerations, and project goals must be considered when selecting the membrane. When implemented correctly, the membrane should decrease fouling rates, optimize removal efficiency, and should have a relatively high life expectancy[89].

A major concern for membrane systems is the occurrence of "wetting" within membrane pores. Wetting is the phenomena which occurs when the feed solution penetrates into membrane pores[96]. Despite having a relatively large pore size, ranging from 0.01- to 1-micrometer[89], distillation membranes are relatively resistant to wetting due to several characteristics of the system including the membranes hydrophobicity, the narrow pore size distribution, and a large contact angle between the solution and membrane .

Membranes are made from inorganic polymers, constructed in either a single- or multi-layer design. These materials—often polytetrafluorethylene (PTFE), polypropylene (PP), or other commercially available polymers[22,84,97]—are highly hydrophobic and intrinsically repel water. The hydrophobicity, working congruently with adequate pore size and a steep angle of contact between the aqueous solution, the surface of the membrane, and liquid surface tension, results in capillary pressures strong enough to support a vapor-liquid interface at each pore opening[89,96]. Wetting will occur when the liquid entry pressure (LEP) exceeds that of the capillary pressure and can be generically modeled with the Young-Laplace equation[98] (Equation [3]).

$$LEP = \frac{-\beta\gamma_l\cos(\theta)}{r_{max}} = \Delta P_{interface} = P_f - P_p \qquad [3]$$

Where,

- Pore geometry, $\beta$, is a coefficient less than or equal to one,
- Liquid surface tension is represented by $\gamma_l$,
- $\Theta$ is the surface contact angle,
- $r_{max}$ is the pore radius, and
- $\Delta P_{interface}$ is the difference in hydraulic pressures between the feed and permeate sides of the membrane.

As demonstrated in the Young-Laplace equation, decreasing the maximum allowable pore size of the membrane, or increasing the contact angle across the membrane will increase the LEP.

However, flux decreases congruently with a decrease in pore size. Flux is one of the key factors for facilitating the mass transfer across the membrane and must be maintained at a minimum level to operate an efficient MD unit. Membrane thickness and porosity are other components impacting flux. They play significant roles in the mass transfer phenomena, considerably impacting thermal conductivity[93]. Loss of thermal effects are even more pronounced in DCMD configurations.

Membranes are commercially available in both flat sheet and hollow fiber configurations, both of which are applicable to DCMD units. Flat sheet membranes are constructed of sheets of membranes place between spacers that are then inserted between two rectangular membrane cells. Hollow fiber membranes consist of a series of membrane tubes which are permanently placed into a housing unit. Hollow fiber membranes are designed to produce higher flux rates, but the design of the units make them more prone to fouling and are expensive to replace. They are therefore typically operated at lower concentrations, must be cleaned more frequently, and should only be used after extensive pre-treatment[99,100]. Perhaps due to the high contaminant concentrations found in PWs, permeate flux and heat transfer rates have been observed to be significantly higher in flat sheet membrane treatment under various operating conditions when directly compared to each other. Regardless, both flat sheet and hollow fiber membranes produced a high-quality permeate when used in DCMD configurations[100].

### 2.35 System Configurations

Several process flow configurations have been developed. In all configurations, at least one side of the flow is in direct contact with the membrane, and they differ in their methods by which the permeate flow condensates on the other side of the membrane. Figure [12] show four common MD setups[37,89,91], each optimized for specific operations and feed stream matrixes:

- Direct Contact Membrane Distillation (DCMD) —the most basic system design; in DCMD operations both sides of the membrane are in direct contact with liquid phases. The heated flow solution flows across one side of the membrane while the cooled permeate stream flows across the other.

- Air Gap Membrane Distillation (AGMD)—in AGMD configurations, an additional air gap is added between the membrane surface and the cooling plate on the permeate side of the membrane. The additional air layer decreases conductive heat lost across the membrane.

- Vacuum Membrane Distillation (VMD)—in VMD, the driving force for condensation is a vacuum located on the permeate side of the membrane. The vapor is externally condensed in a separate device.

- Sweeping Gas Membrane Distillation (SGMD)—SGMD utilizes a cold sweeping gas phase to pull the vapor molecules away from the membrane and condenses them in a separate device outside of the membrane.
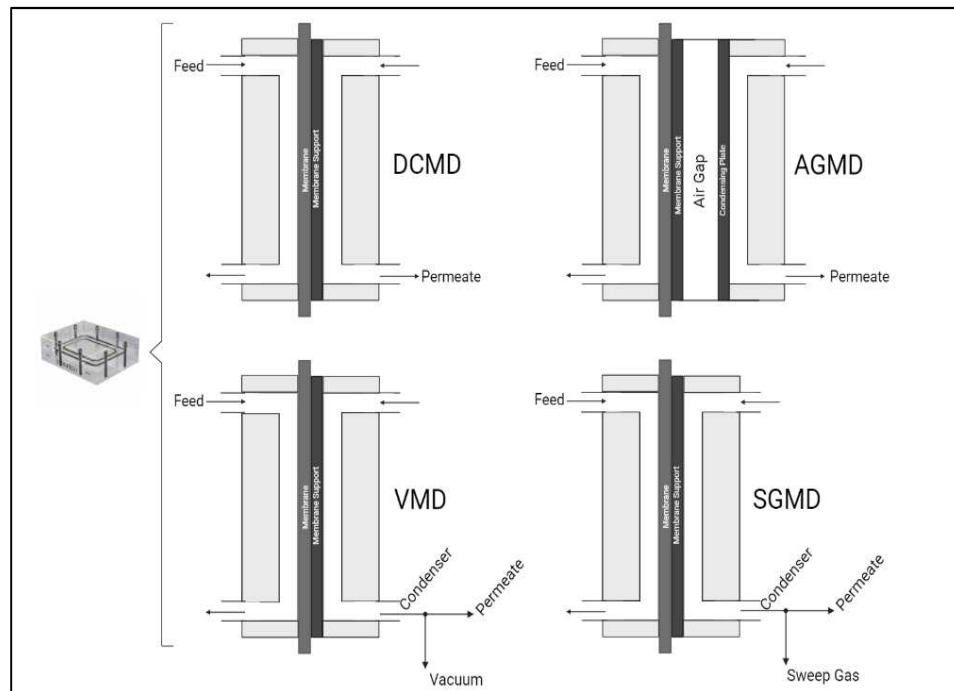


*Figure 12: Common configurations for membrane distillation*

DCMD and AGMD systems are significantly simpler and cheaper relative to their counterparts. Though more complex feed streams may necessitate the use of an external condenser, it is more efficient to condensate the permeate on the surface of the membrane when the permeate stream is water[37]. Applications for each configuration are summarized in Table [1][89,91].

*Table 1: Common applications for membrane distillation configurations*

| MD Configuration | Applications |
| --- | --- |
| DCMD | for aqueous solutions; seawater and brackish water desalination, wastewater treatment, separation and concentration of contaminants |
| AGMD | for aqueous solutions; all DCMD applications, removal of volatile organic compounds |
| VMD | treatment of alcohol solutions, recovery of aromatics, seawater and brackish water desalination, treatment of some industrial wastewaters |
| SGMD | brackish water desalination, removal of volatile organic compounds, azeotropic mixture separation |

DCMD is the simplest model to build and work with at a bench-size scale. DCMD is most efficient when used for desalination and concentration applications[89], such as the treatment of produced water, though other models may potentially work more efficiently for the given process. The construction of a basic, bench-scale DCMD system includes the following primary components: a hot feed tank, a feed pump, a flat sheet DCMD membrane, a permeate pump, and a chilled permeate tank. Temperature regulation systems must be used to maintain constant temperatures within the feed and permeate tanks. The pumps introduce the feed and permeate flows to the membrane allowing for partial temperature and pressure gradients to be implemented, driving the mechanism[97].

In DCMD systems, both the feed flow and permeate flow are in direct contact with the surface of the membrane. As the feed vapor passes through the boundary layer, the condensation is collected directly into the liquid phase, which results is a relatively high permeate flow rate[97]. The high permeate flux rate also makes it a favorable option for scaling up to commercial size. Both flat sheet and hollow-fiber membranes are commercially available for laboratory-scale DCMD systems[89].

Due to the continuous contact between the permeate flow and the warmer feed condensation, there is significantly more heat loss with DCMD units relative to other MD configurations. Additional layers between the feed and permeate provide more extensive insulation, decreasing the latent heat loss, but also yield a decrease in mass transfer efficiency, decreasing permeate flow efficiency[93].

*2.36 Produced Water Applications of Membrane Technology*

Relative to the high pressure of high temperature membrane processes, the low operating temperatures and pressure, less favorable conditions for fouling, and an ability to use waste heat or renewable energy sources[101] make MD an appealing and potentially lucrative option for oil and gas field operations. Its ability to recover hypersaline feed waters makes it even more applicable to shale-gas industry operations[31].

Several key parameters must be known and regulated to achieve optimal results on a MD unit. In addition to the system configuration and membrane selection, other parameters include the flow rate, temperature, and concentration of the influent flow. With more complex feed matrixes come decreased flux[90] and increased risk of membrane wetting and fouling[96], thus monitoring the flow is essential.

PTFE membranes have been used in the MD treatment of produced water based on its high water flux and extremely hydrophobic nature—all necessary for a feasible MD set-up[22,84]. Polyvinylidene fluoride (PVDF) and polypropylene (PP) have also been tested with produced water DCMD setups, but the increased membrane thickness decreases the water fluxes, making it a less favorable option for DCMD treatment operations[22,102]. Characteristics of multiple membranes with the highest flux and conductivity values from their respective experiments were compiled into the Table [2][22,84,102,103].

*Table 2: Common properties of commercial membranes successfully implemented in membrane distillation treatment of produced water.*

| Properties of Commercially Avaliable PTFE Membranes Used with Produced Water | | | | |
|---|---|---|---|---|
| Manufacturer | Sterlitech, USA | Aquastill | --- | Millipore Sigma |
| Model | QM038 | --- | --- | FGLP14250 |
| Structure | Single-layer | Single-layer | Bi-layer | Bi-layer |
| Pore size (µm) | 0.2 | 0.17 | 0.2 | 0.22 |
| Thickness (µm) | 25-50 | 77 | 230-310 | 150 |
| Porosity | 0.64-0.82 | 0.83 | --- | 0.85 |

Though the unsupported, single-layer structure of the Sterlitech and Aquastill membranes make for a much thinner membrane, the supporting nets of the latter two, made of polyethylene (PE) and PP polymers respectively, improve the strength and handling of the membrane[104]. Unsupported membranes typically have a higher LEP as well as an increased temperature tolerance relative to supported membranes[105].

Typical operating temperatures for MD range from 40 to 80 degrees Celsius on the feed side and between 10 and 30 degrees Celsius on the permeate side[22,97]. Temperature and pressure gradients both play major roles in the amount of water flux across the membrane. Less fouling has been reported with produced water when the MD units are operated at a higher feed temperate[22], perhaps due to lower water viscosity[106]. To decrease the energy costs associated with heating the feed solution, methane byproducts may be captured and reused as an energy[107] instead of being burned off as waste.

Due to the high TDS and hydrocarbon concentrations of produced water, system efficiency and effluent quality is low relative to a cleaner feed flow. One experiment reports an 11 percent decline in flux at a 1-ppm oil and grease feed concentration—the maximum reported concentration of real PWs[22]. At a concentration of 0.2-ppm, there were no observable decreases in flux, suggesting that with adequate pretreatment, the MD unit will function at a high operational capacity. A MD's main advantage over other membrane technologies for the treatment of produced water is its ability to treat water with higher total dissolved solid (TDS) concentrations.

Though steady flux declines are observed as the TDS increases, it is still feasibly operational until around 300-g/L[22]. Even taking into account the oil and water emulsions and the high TDS found in PWs, there were high salt and oil rejection rates that yielded a high quality distillate[22]. Other studies have displayed similar results, with permanent membrane degradation due to inorganic fouling and surface adsorption being the main points of concern[84,102,103]. If the final effluent solids concentrations are low enough, the flow may be reused for certain industrial or agricultural applications.

CHAPTER III

METHODOLOGY

## 3.1 ICP Analysis for Testing Membrane Technologies

ICP methods were used throughout various parts of the OCAST project. These instruments can measure soluble ion concentrations in ranges as low as one PPT and were used to test for low-concentration analytes in solution. ICP technologies were useful for determining contaminant concentrations in water and wastewater, as well as for testing the effectiveness of different developing technologies for the treatment of PW.

A PerkinElmer Optima 4300 DV ICP-OES was initially used to measure samples. Additional analysis was performed by a third-party environmental testing laboratory using ICP-MS and ICP-AES instruments. Analysis was performed according to EPA Methods 6010B[108], 6010D[109], and 6020[110].

### *3.11 Sample Digestion Procedures*

All samples must be appropriately digested, accounting for sample matrix and targeted analytes. Samples were digested according to *Standard Methods* Method 3030E: Nitric acid digestion and 3030I: Nitric acid-Perchloric acid-Hydrofluoric acid digestion[75].

Method 3030I was used to determine a membranes' ability to retain modified silica nanoparticles that are chemically attached to its surface. ICP technology was used to measure silica

concentrations in influent and effluent flows. $SiO_2$ is highly insoluble in water, thus the silica

nanoparticles had to be converted into a soluble form for

measurement. Each sample was prepared using Method 3030I, which is capable of dissolving the

compound into solution[79]. HF is responsible for the dissolution of silica and other silicates into

$SiF_4$ via the reactions[79] seen in Equation [4] and [5].

$$SiO_2 + 6HF \rightarrow H_2SiF_6 + 2H_2O \qquad [4]$$

$$H_2SiF_6 + \Delta \rightarrow SiF_{4(g)} + 2H_2O \qquad [5]$$

The addition of $HClO_4$ to the sample was to protect the glass parts and tubing of the ICP

instrumentation from damage. When reacted with excess HF, the $HClO_4$ oxidized to the acyl

halide Perchoryl fluoride $(ClO_3F)$[79] (Equation [6]).

$$HClO_4 + HF \rightarrow ClO_3F_{(g)} + H_2O \qquad [6]$$

The oxidation reaction begins to occur at around 160°C. The gaseous $ClO_3F$ was evaporated out

of the system, removing the residual fluoride ions that could potentially damage the ICP. The

$HNO_3$ additions were made prior to the addition of $HClO_4$. $HNO_3$ decomposes almost all metal

and alloys to nitrates (Equation [7]), diluting the concentration of suspended metals in the

solution. This minimized the $HClO_4$ oxidation reaction[79].

$$Metal + HNO_3 \rightarrow (Metal)NO_3^- + NO/NO_2 + H_2O \qquad [7]$$
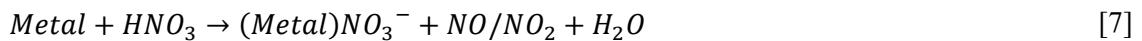
$HNO_3$'s relatively low boiling point requires it be added in two stages to increase contact time

and maximize the oxidation reactions.

The sample constituents measured for water analysis and in adsorption tests were already

solubilized. Thus, the standard Nitric acid digestion (Method 3030E) was used for these

objectives. $HNO_3$ reacts with almost all ions and is fully soluble in water, as seen in Equation [7].

Samples, as well as laboratory standards and rinsing solution, were spiked to 2% $HNO_3$ by volume.

All acids used throughout the process were high-purity, trace metal grade acids that were properly used and stored to minimize contamination. Lower quality materials or contaminated samples could cause matrix interferences and produce poor results.

### 3.12 Instrument Preparation

A standard operating procedure (SOP) for the PerkinElmer Optima 4300 DV ICP-OES. This document was adopted from EPA Method 6010D and aimed to ensure consistent practices on the instrument to minimize operator error. Additional samples were digested and sent to a third-party facility, where elemental scans were done on an ICP-AES (EPA Method 6010B) or an ICP-MS (EPA Method 6020). These testing procedures for the measurement of trace metals are all similar, though each instrument is optimized for slightly different uses. Laboratory calibration standards were made using PerkinElmer Pure IV multi-element standard for ICP applications. Standards were diluted in series using a micropipette to concentrations ranging from 1PPB to 10PPM, depending on the data set. The calibration standards were made according to the procedure outlined in the EPA methods listed previously.

### 3.13 Sample Preparation and Analysis

As a quality control measure, a representative sample from the DI water system used to dilute samples and standards was tested for purity. ICP testing methods require DI water meeting ASTM Type I water specifications as defined in ASTM D1193-06[111]. The sample was tested for the parameters listed in Table [3] using conductivity measurements from the third-party lab, a low-range Hach Total Organic Carbon Reagent set, and an ICP-OES. The samples were digested using Method 3030E and analyzed according to EPA Method 6010D.

*Table 3: Standard Specifications for Reagent Water Type I as described in ASTM D1193-99e1. All parameters are measured at 25˚C.*

| Parameter | Limit |
|---|---|
| Electrical Conductivity, µS/cm | < 0.0560 |
| Electrical resistivity, m$\Omega$-cm$^2$ | > 18.000 |
| Total Organic Carbon, µg/L | < 50.000 |
| Chlorides, µg/L | < 0.0015 |
| Total Silica, µg/L | < 0.0434 |

ICP-OES and ICP-AES technologies were used for the silica retention tests, in accordance with EPA Method 6010. The insoluble nature of the silica nanoparticles ($SiO_2$) in water necessitated the application of Method 3030I to convert all suspended ions into a solubilized state, allowing for a total silica measurement.

Produced water samples were taken from oilfield water processing and treatment site. Metal and salt concentrations in the untreated samples were measured using an ICP-MS (EPA Method 6020). To remove suspended solids and residual oil, 2.5-mL of produced water sample was taken from a well-mixed representative sample. This was centrifuged using Fisher Scientific accuSpin Micro 17 at 13,000-rpm for 10 minutes. The sample was then filtered using a generic 0.22-µm hydrophobic PTFE syringe filter. To ensure elemental concentrations are within the range of the ICP-MS, a micropipette was used to mix 1-mL of filtrate and 9-mL of DI water in a 10-mL centrifuge tube. This was then thoroughly mixed on a Vortex-Genie 2 Laboratory Mixer. The samples were spiked to a 2% $HNO_3$ concentration in accordance with Method 3030E. To better characterize the PW samples, additional tests were performed on undigested samples, and are noted in the **Results and Discussion** section when relevant.

To test the sorption capacity of silica nanoparticles modified in various capacities, sorption tests were conducted using DI water solutions spiked LiCl, $LaCl_3$, and NaCl salts. Solutions were

prepared with various salt concentrations and matrix complexities. The samples were digested

using Method 3030E and measured using an ICP-MS in accordance with EPA Method 6020.

Standard solutions were prepared by adding 20-mg of the selected salts to a 1-L volumetric flask.

DI water was then added to volume. Table [4] shows the weight of each metal ion in solution for

every 20-mg of salt.

*Table 4: Stoichiometric calculations for metal ions in salt solutions*

| 20-mg$^{\text{Lithium Chloride}}$ | $\rightarrow$ | 3.274-mg/L $^{\text{Lithium}}$ |
|---|---|---|
| 20-mg$^{\text{Lanthanum (III) Chloride}}$ | $\rightarrow$ | 11.327-mg/L $^{\text{Lanthanum(III)}}$ |
| 20-mg$^{\text{Sodium Chloride}}$ | $\rightarrow$ | 7.8679-mg/L $^{\text{Sodium}}$ |

When running a sorption test, ICP analysis was ran on before and after samples, as well as at

selected time intervals, to test for metal adsorption efficiency. These solutions were diluted in

series to make calibration standards.

## 3.2 Application of the Dusty-Gas Model for Prediction of Permeate Flux in a Direct Contact Membrane Distillation System

As permeate flux is one metric used to quantify the efficiency of an MD system, it is useful to see

permeate flux plotted against the independent system inputs to determine the optimal operating

conditions for the system. The simulation procedure developed for and presented in this report

was developed in R programming language[112] using the developmental environment RStudio[113].

Primary model construction used the equations outlined in *Flux Prediction in Direct Contact

Membrane Distillation*[114], with additional sources being used where cited.

### 3.21 Preliminary Data Compilation and Required Calculations

Initial efforts focused on defining system boundaries and objectives and establishing all system

inputs. Input variables (Figure [13]) include empirically defined constants, values provided from

manufacturers, values cited in literature, and numbers calculated from cited equations. A complete compilation of symbols and nomenclature can be found in Appendices B and C.
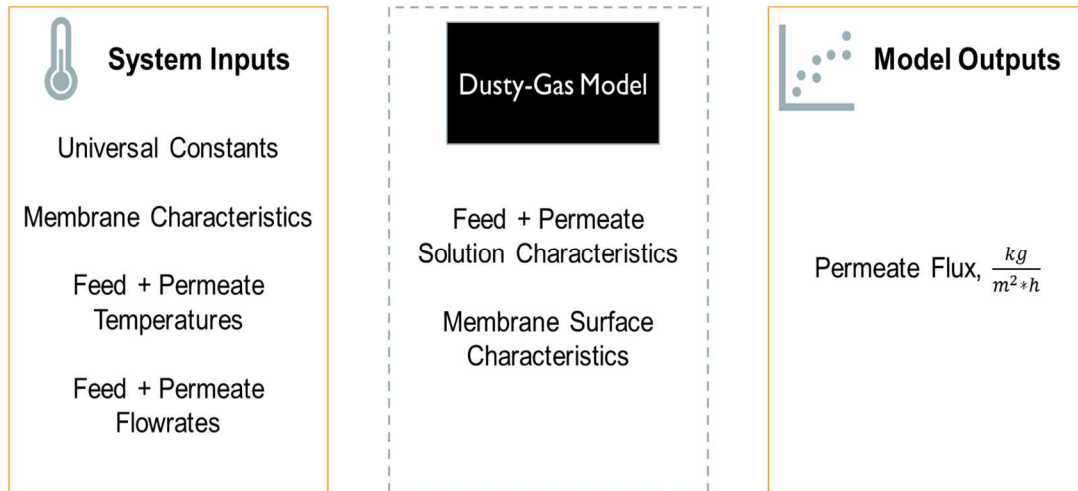


*Figure 13: Established system boundaries and variables for the development of the Dusty-Gas Model.*

The input values include constant and variable values. Constants include set and defined values: the universal gas constant, thermal conductivity values for given materials, and the molecular weight of a solution. Less defined are membrane characteristics, which vary between types of membranes and even display some variance between individual membranes from the same batch. These values are determined either by the manufacturer or experimentally and include the membrane porosity, thickness, pore radius, and membrane length. They are assumed to be uniform as the variances are small and the inclusion of them would significantly increase the complexity of the model. A complete list of numerical values for the system inputs used in this study is in Appendix B. Some input values are not experimentally determined by the manufacturer but can be derived algebraically – these are discussed in Appendix D.

The variable inputs for the model include the temperature and flowrate of both the feed solution and the permeate solution. A working range for each variable is set, which are then used by the model to optimize each variable, and then the system in its entirety. The output of the simulation

yields the permeate flux, as well calculated solutions for membrane and solution characteristics that may be recorded if desired.

### 3.22 Procedure for Flux Simulation

The permeate flux can be predicted by multiplying the overall mass transfer coefficient by the transmembrane vapor pressure difference (Equation [8]).

$$J_w = C_C \Delta P_v \tag{8}$$

The mass transfer coefficient is found using the following approach. The heat transfer coefficient (Equation [9][115]) for both the feed and permeate sides are estimated using the Nusselt number, thermal conductivity, and hydraulic diameter. Since the pore size is assumed to be circular, the hydraulic diameter is equal to two times the pore radius[116].

$$h = \frac{Nu * k}{d} \tag{9}$$

The Nusselt number is calculated using Reynolds number (Equation [10][115]) and Prandtl number (Equation [11][117]).

$$Re = \frac{\rho u d}{\mu} \ , Pr = \frac{\rho C_P}{k} \tag{10] [11}$$

The thermal conductivity values can be approximated using Equation [12][118].

$$k = (-8.354 * 10^{-6}) * T_{bi}^2 + (6.53 * 10^{-3}) * T_{bi} - 0.5981 \tag{12}$$

The equation used to calculate the Nusselt number depends on flow conditions. Flow conditions can be determined using Reynolds number where value of less than 10,000 is categorized as a laminar flow. Under these conditions, the Nusselt number is calculated using Equation [13].

$$Nu = 1.86 \left(Re \ Pr \ \frac{d}{L}\right)^{0.33} \tag{13}$$

Under turbulent conditions (where, *Re* > 10,000), the Nusselt number is calculated as seen in

Equation [14].

$$Nu = 0.023Re^{0.8} \, Pr^{0.33} \left(\frac{\mu}{\mu_s}\right)^{0.14} \tag{14}$$

Using these parameters, all values calculated in this report were classified as laminar, thus

Equation [13] was used throughout the simulation.

To calculate the permeate flux, an iterative approach was built to estimate the transmembrane

temperatures at both the feed and permeate sides[114,119]. The bulk feed and permeate temperatures

were assumed as the initial guess for the membrane surface temperature, and these values were

used to establish the thermal physical properties of water, as well as mass and heat transfer

coefficients[114]. The employed properties of water ($\mu$ and $\rho$) were tabulated for each temperature

value using the hydraulics: Basic Pipe and Open Channel Hydraulics[120] package for R Core

Team. After the initial temperatures for the simulation were assumed, the membrane diffusivity

was estimated using Equation [15][121,122].

$$PD = 0.00001895 * \left(\frac{T_{mf} + T_{mp}}{2}\right)^{2.072} \tag{15}$$

The vapor pressure difference was estimated using a combination of Antoine's equations and the

Clausius-Clapeyron equation, which considers both the temperatures and partial pressures of the

membrane's surfaces (Equations [16]-[18]).

$$\Delta H_v = 1.7535 \left(\frac{T_{mf} + T_{mp}}{2}\right) + 2024.3 \tag{16}$$

$$\frac{dP}{dT} = \frac{\Delta H_v}{R \left(\frac{T_{mf} + T_{mp}}{2}\right)} \exp\left(23.328 - \frac{3841}{\frac{T_{mf} + T_{mp}}{2} - 45}\right) \tag{17}$$

$$\Delta P_v = \left(\frac{dP}{dT}\right)\left(T_{mf} - T_{mp}\right) \tag{[18]}$$

Subtracting Antoine's equation from the ambient air pressure value (101,325-Pa) was additionally used to singularly calculate the partial pressure at the membrane surface (Equation [19]).

$$P_a = 101{,}325 - \left(\exp\left(23.328 - \left(\frac{3841}{\frac{T_{mf} + T_{mp}}{2} - 45}\right)\right)\right) \tag{[19]}$$

Assuming the membrane pores are uniform in size, the overall mass transfer coefficient was calculated using Equation [20].

$$C_C = \frac{1}{R\left(\frac{T_{mf} + T_{mp}}{2}\right)\delta}\left[\frac{3}{2}\frac{\tau}{\varepsilon r}\left(\frac{\pi M}{8\left(\frac{T_{mf} + T_{mp}}{2}\right)}\right)^{0.5} + \frac{P_a\tau}{\varepsilon PD}\right]^{-1} \tag{[20]}$$

The flux value for the initial iteration was then calculated using Equation [8]. The feed and permeate membrane temperatures were calculated with the with Equations [21] and [22].

$$T_{mf} = \frac{\frac{k_m}{\delta}\left(T_{bp} + \frac{h_f}{h_p}T_{bf}\right) + h_f T_{bf} + J_w\Delta H_v}{\frac{k_m}{\delta} + h_f\left(1 + \frac{k_m}{\delta h_p}\right)} \tag{[21]}$$

$$T_{mp} = \frac{\frac{k_m}{\delta}\left(T_{bf} + \frac{h_p}{h_f}T_{bp}\right) + h_p T_{bp} + J_w\Delta H_{vw}}{\frac{k_m}{\delta} + h_p\left(1 + \frac{k_m}{\delta h_f}\right)} \tag{[22]}$$

Using an error function, these new values for the membrane surface temperature are compared to the initial assumed values. When the margin of error is less than 0.1%, the code stops the iterative

function and outputs the final calculated value for the membrane temperature, otherwise the final calculated value is used as the new assumed value for the next iteration.

Through this loop, the model has obtained the values for the mass transfer coefficient and the overall flux value, in addition to the membrane surface temperatures. These are then applied to the output data in their intended capacity.

For potential comparative purposes, the values for the Knudsen Coefficient and the Ordinary (Diffusivity) Coefficient were calculated alongside the combined overall mass transfer coefficient discussed above. These were calculated using Equations [23] and [24].

$$C_K = \frac{2}{3} \frac{\varepsilon r_k}{RT\tau\delta} \left(\frac{8RT}{\pi M_w}\right)^{0.5} \qquad [23]$$

$$C_D = \frac{\varepsilon}{\tau\delta} \frac{PD_W}{P_a} \frac{M_w}{RT} \qquad [24]$$

To calculate the permeate flux for the Knudsen or molecular diffusion models, Equation [20] should be replaced with the selected model's coefficient (Equation [23] or [24]), in the modeling process. The iterative process is summarized in Figure [14].
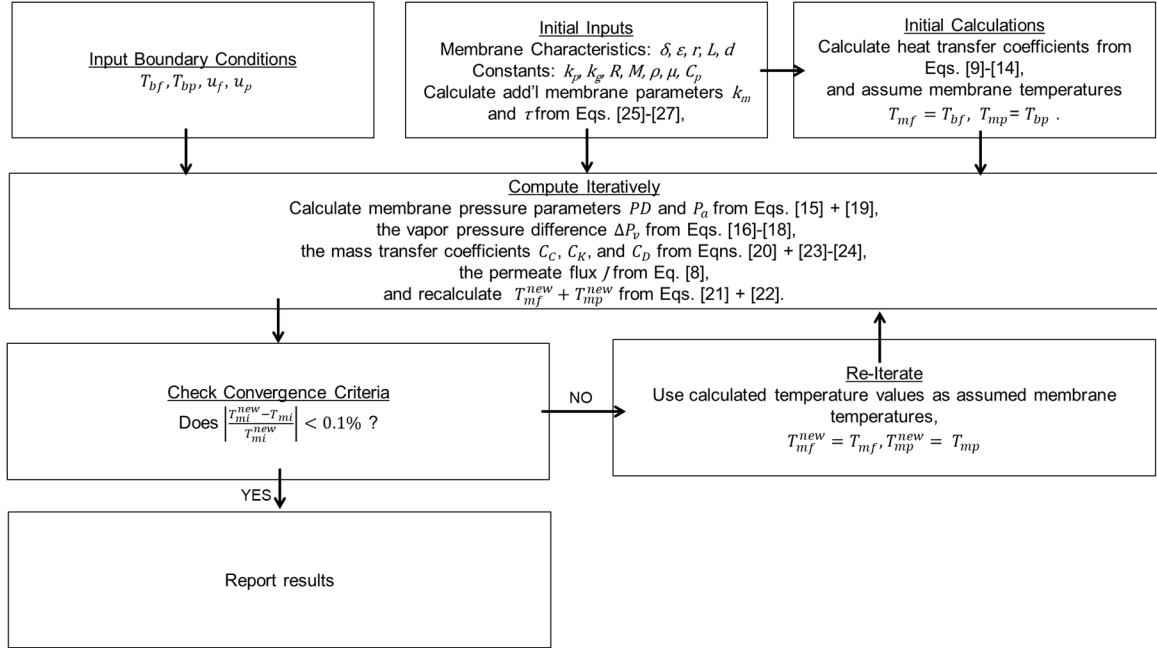
*Figure 14: Flow diagram for the Dusty-Gas Model's iterative procedure for the calculation of permeate flux.*

### 3.23 Saline Feed Solution Model Modification

When the feed solution contains high salt concentrations, such as those found in PWs, Equations [25]-[26] are used to calculate the pressure on the feed side of the membrane[89], in order to provide a more accurate model.

$$P_{f,m} = (1 - x_{water})\gamma P_{f,m}^0 \qquad [25]$$

$$\gamma = 1 - 0.5x_{NaCl} - 10x_{NaCl}^2 \qquad [26]$$

Equation [25] uses the molar concentration of water, $x_{water}$, the activity coefficient for salt in solution, $\gamma$ (Equation [26]), and the membrane pressure of clean solution, $P_{f,m}^0$, to account for the salt concentration in the feed solution. $P_{f,m}^0$ is calculated using Antoine's equation (using the same equation as $P_{p,m}$, seen in Equation [28]) using the feed temperature only. The activity coefficient is calculated using Equation [26] which uses the molar concentration of salt to estimate ionic activity. If working with a saline feed, Equation [19] must be recalculated (Equation [27]).

43

$$P_a = 101{,}325 - \left(\frac{P_{f,m} + P_{p,m}}{2}\right) \tag{27}$$

Where $P_{p,m}$ is calculated using the Antoine's equation (Equation [28]).

$$P_{p,m} = \exp\left(23.328 - \left(\frac{3841}{\frac{T_{mf} + T_{mp}}{2} - 45}\right)\right) \tag{28}$$

### *3.24 Data Processing*

The system predicted values for permeate flux under various input conditions and were

graphically presented using data visualization tools in RStudio and Microsoft Excel. These

figures and analysis are in the **Results and Discussion** section below.

### *3.25 Model Validation*

Model validation allows for the model results to be applied to research efforts. By utilizing

experimental results published in literature[123,124] and applying the studies' input conditions to the

model, predicted permeate flux values will be generated. The permeate flux values predicted by

the model will be plotted against the observed values recorded from experimentation and the $R^2$

value for the dataset will be calculated (Figure [15]).
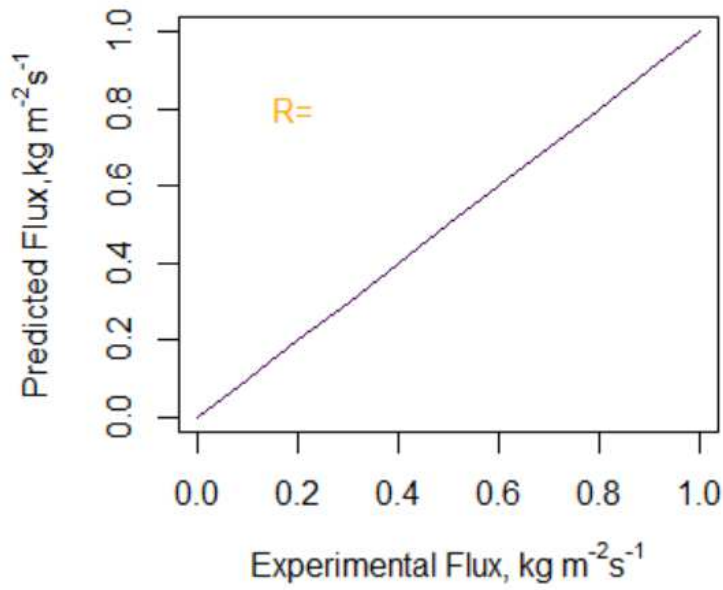
*Figure 15: On a 1:1 graph, consistently high $R^2$ values between the Experimental Flux and Predicted Flux values for selected datasets can be used to validate high model performance. Once model accuracy is demonstrated and the uncertainty set, R2values may help determine the quality of experimental datasets.*

A higher $R^2$ value indicates higher model accuracy and uncertainty valuations can also be set based on the 1:1 graph. This approach can also aid in identifying low quality experimental data, as 1:1 graph may show low statistical similarities between the predicted and experimental flux values for a model that otherwise performs well with datasets.

Using the bench-scale DCMD system discussed in the next section, the characteristics for the system as well as specific experimental conditions, as identified in Figure [13], are uploaded into the model. This allows important values (membrane pressure, surface temperatures, flux prediction, etc.) to be easily collected, and additionally aids in determining the quality of the data. If the graph shows an acceptable level of correlation between the model and the bench-scale system, the model may be used to predict system outputs under a variety of conditions, allowing for an economical and timely way to test the system. The statistical similarities between the model and the system will be reported with all data sets, and the calculated uncertainty values should be considered when making conclusions and recommendations.

## 3.3 Direct Contact Membrane Distillation for the Treatment of Produced Waters

A bench-scale DCMD system was developed according to the process flow diagram identified in Figure [16].
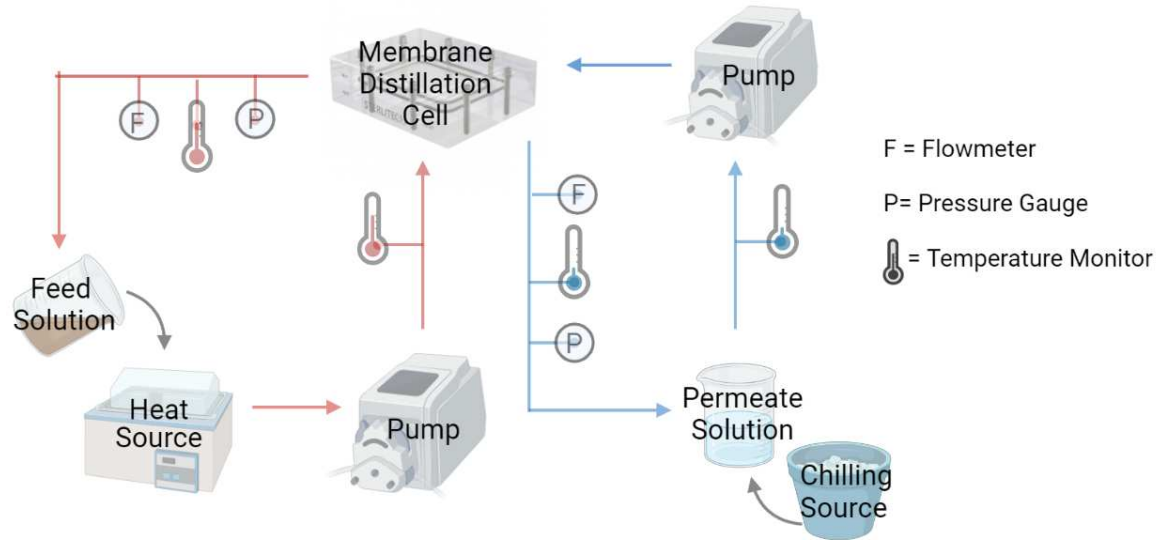


*Figure 16: Process flow diagram for bench-scale Direct Contact Membrane Distillation System*

Temperature parameters should be closely monitored during operation to ensure the selected feed and permeate temperatures are maintained. The permeate flux of the system is calculated by dividing the increase in permeate volume by the total active surface area of the membrane, as seen in Equation [29].

$$J = \frac{measured\ permeate\ flow\ rate}{membrane\ area} \qquad [29]$$

### 3.31 Bench-Scale System and Model Verification

Concurrent with model development, a bench-scale MD system was constructed according to the process flow diagram seen in Figure [16]. Figure [17] shows the DCMD system setup set-up for permeate flux studies, with major components labeled and identified (Table [5]).
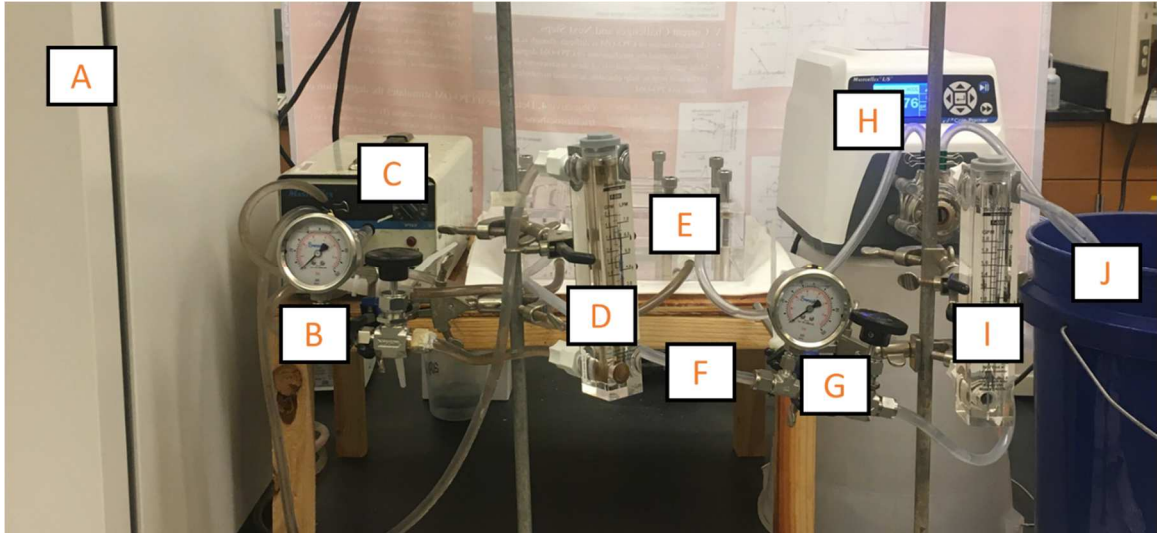
*Figure 17: Set-up of bench-scale membrane distillation system. Major system components are labeled and identified in Table [5] below.*

*Table 5: Membrane distillation system components as identified in Figure [17] above.*

| | |
|---|---|
| A | Feed Solution Heater + Feed Tank |
| B | Concentrate Pressure Gauge + Control Valve |
| C | Feed Pump |
| D | Concentrate Flow Meter |
| E | DCMD Membrane + Cell Assembly |
| F | 3/8" Low Pressure Tubing |
| G | Cooling Solution Pressure Gauge + Control Valve |
| H | Cooling Solution Pump |
| I | Cooling Solution Flow Meter |
| J | Cooling Solution Ice Bath + Permeate Tank |

The makes and models for the parts listed above are in Appendix E.

Sterlitech QL822 membranes were used for all experimental datasets. The membrane is composed of PTFE with a PP netting. The thicker membrane should allow less heat transfer, and the larger pore size should increase the flux rate, while still being within the parameters shown to be effective for MD treatment of PW. Membrane properties provided by the manufacturer are tabulated in Table [6].

*Table 6: Cell geometry and membrane characteristics for the system used in produced water experiments.*

| Symbol | Value |
|---|---|
| $\delta$ | 130-230-μm |
| $\varepsilon$ | 70-85% |
| $K_g$ | 0.29-W/mK |
| $K_p$ | 0.259-W/mK |
| $d_p$ | 0.45-μm |
| L | 0.143-m |
| W | 146-mm |
| H | 1.9-mm |
| A | $2.774 \times 10^{-4}$-m$^2$ |
| $d_h$ | $3.75 \times 10^{-3}$-m |

Due to the large amounts of heat transfer occurring across the membrane, experiments were limited to a duration of ~90 minutes. Feed and permeate flowrates were recorded prior to experimentation. Before and after samples were taken from the feed and permeate solutions to obtain conductivity data points. Feed and permeate temperature values were recorded throughout the duration of the experiment. These recorded values, as well as the membrane characteristics and cell geometry (Table [6]), and more general constants listed in Appendix B were used to obtain a predicted flux curve using the developed model. These outputs can be compared to the overall experimental flux value calculated using Equation [8].

The increase in permeate volume obtained by subtracting before and after measurements of the permeate solution is divided by the membrane area. The permeate weights were measured using a Mettler Toledo ME4001EE balance, which measures up to 4200-g with a tolerance of 0.1-g.

To observe membrane foulants, membrane imaging was done using an AmScope™ 10X-30X Trinocular Stereo Microscope. Each membrane was imaged at a 11.25X and 30X zoom level.

The values in Table [6] were input into the developed model alongside experimentally independent variables and the universal constants (as seen in Appendix B). The flux as predicted

by the model was compared to the flux obtained using experimental data and Equation [8].

Quantitative model analysis performed using root-mean-square error (Equation [30]), model

regression (Equation [31]), and percent error (Equation [32]) calculations will allow the model to

be validated for datasets outside of sample datasets[125].

$$RMSE(\%) = \frac{100}{\bar{O}} \left( \frac{\Sigma_{i=1}^{n}(P_i - O_i)^2}{n} \right)^{1/2}$$

[30]

$$ME = \frac{\Sigma_{i=1}^{n}(O_i - \bar{O})^2 - \Sigma_{i=1}^{n}(P_i - O_i)^2}{\Sigma_{i=1}^{n}(O_i - \bar{O})^2}$$

[31]

$$error(\%) = \frac{|P_i - O_i|}{O_i} * 100$$

[32]

These equations are calculated using Excel[126]. With known model performance values for the

bench-scale system, the model can be used to predict model outcomes for variable input

conditions.

CHAPTER IV

RESULTS AND DISCUSSION

## 4.1 ICP Analysis for Testing Membrane Technologies

Good ICP data relies on the precision and accuracy of the instrument, as well as the quality and purity of all minerals and reagents used throughout the process. Multiple project components required matrix analysis using ICP instruments to test the efficiency, durability, effectiveness, and overall sustainability of various systems. ICP instrumentation, operating procedures, and all constituents used to digest standards and samples were assessed for quality to better ensure trustworthy results.

### *4.11 DI Water Quality Assessment*

All DI water used in experimental procedures was obtained from a RO/DI water system. To determine potential uncertainty values introduced from to the systems from the water source, a DI water sample was digested using Method 3030E[75]. Following EPA Method 6020[110], a third-party environmental testing facility performed an ICP-MS scan on the sample to detect for 29 elements commonly found in feed water. Contaminants with concentrations within the instrument's detection range are listed in Table [7], all others tested for are below the practical detection limit.

| Element | Concentration (mg/L) |
|---|---|
| Boron | 0.0111 |
| Calcium | 0.0611 |
| Magnesium | 0.0015 |
| Potassium | 0.0434 |
| Silicon | 0.0358 |
| Sodium | 0.0626 |

The ICP results show chloride and silica values below the maximum contaminant level allowed

by ASTM D1193-99e1 (Table [7]). Other values tested for compliance are in Table [8].

*Table 8: Results of tests conducted on DI water. All measurements were within the parameters outlined in ASTM D1193-99e1 for Type I water.*

| Parameter | Value |
|---|---|
| Electrical Conductivity, μS/cm | <0.02 |
| Electrical Resistivity, MΩ-cm$^2$ | 121 |
| Total Organic Carbon, μg/L | <0.500 |

All values are well within the values determined to be acceptable in high-purity DI water. In

samples digested with the DI water, the water will not interfere with any analytes being tested for

when measured against a quality control blank. Any error in the measured values would therefore

most likely stem from experimental error or instrumental error.

### 4.12 Silica Retention on Modified Membrane

Samples were taken from the retentate feed of an inorganic membrane treated with modified

silica nanoparticles. DI water was used as a feed solution for the membrane system. The samples

were digested per Method 3030I[75] to dissolve any suspended silica particulate in the sample.

Initial measurements were done on the PerkinElmer Optima 4300 DV ICP-OES using EPA

Method 6010B[109]. The instrument was calibrated using a series of laboratory standards diluted

from SPEX CertiPrep® Claritas PPT® Silicon Standard for ICP to concentrations ranging from

five to 100 PPM. The lower limit, 5 PPB, is generally listed as the minimum detection limit for

silicon on ICP-OES instruments and was thus selected as the low end of the standard range. The

constructed calibration curve is seen in Figure [18].
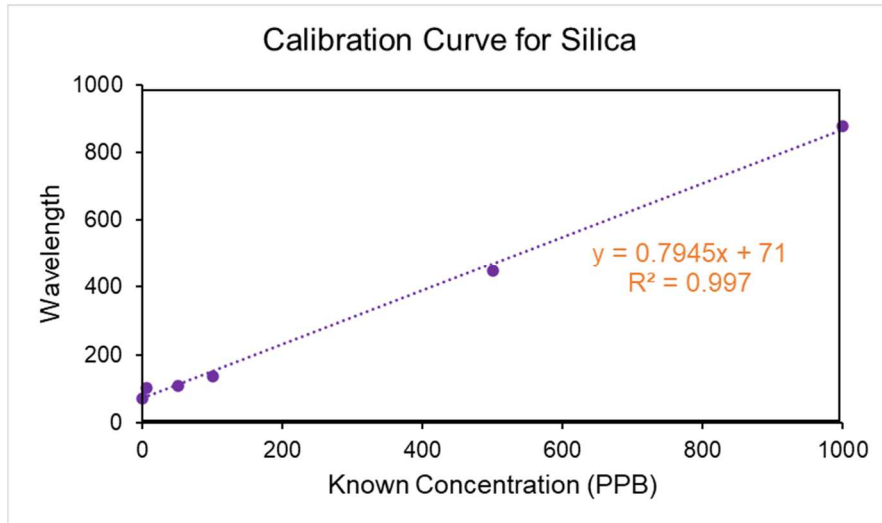


Figure 18:Silica calibration curve constructed from wavelengths measured from laboratory blank and
standard solutions. The Optima 4300 DV ICP-OES was used to measure solutions.

With the calibration curve, the samples were measured estimated to contain the concentration

amounts listed in Table [9].

Table 9: Measured concentration of silica in retentate samples using PerkinElmer Optima 4300 DV ICP-OES
using the calibration curve seen in Figure [18]. The results did not align with previous experiments.
Instrument or sample error was suspected.

| Sample ID | Concentration (mg/L) |
|-----------|----------------------|
| Start     | 155.70               |
| 1 Hour    | 107.29               |
| 3 Hour    | 27.84                |
| 5 Hour    | 79.25                |
| 7 Hour    | 85.23                |

Several aspects of these results were inconsistent with expected outcomes. As the feed solution

for the membrane system was pure DI water, the silica concentration for the initial sample

(Sample ID 'Start' in Table [9]) should be at or near zero after adjusting the calibration curve for

any silica that may be present in the DI water source (Table [7]). Using the linear equation from

Figure [18], the silica concentration in the blank solution is calculated to be approximately 0.0894

mg/L. This is 149.7% higher than the silica measured by ICP-MS as reported in Figure [10]. Furthermore, if the silicon concentration was truly this high, the DI water would not adhere to ASTM standards, shown in Table [3].

Additionally, prior tests ran on retentate runoff showed the largest occurrence of silica runoff in the retentate solution happened at or near the start of the membrane operation. The concentration rapidly decreased as operation continued, as all easily detachable particulate had already washed out. The results presented in Table [9], do not align with this theory, as there is no jump in concentration a the '1 Hour' sample and no steady decrease thereafter. Additionally, the large jump in concentration in the '5 Hour' sample and the continuing increase in the '7 Hour' sample, didn't correspond to the previously observed occurrence.

The same samples were then sent to a third-party environmental testing facility for secondary data analysis. They were measured using the protocols outlined in EPA 6010B[108] for ICP-AES. In addition to sample concentrations, quality control data was also included. Results are in Table [10].

*Table 10: Measured concentration of silica in retentate samples from third-party lab using ICP-MS. The 'Difference' column displays the percent difference between the ICP-MS results shown below and the ICP-OES results from Table [9]. Results were inconsistent with theoretical outcomes. Quality control (QC) data suggests error is due to sample digestion method.*

| Sample ID | Concentration (mg/L) | | Difference (%) |
|---|---|---|---|
| Start | 68.10 | | 128.64 |
| 1 Hour | 43.90 | | 144.41 |
| 3 Hour | 3.63 | | 666.86 |
| 5 Hour | 24.60 | | 222.17 |
| 7 Hour | 21.20 | | 302.03 |
| **QC Blank Concentration (mg/L):** ~0 | | | |
| **QC Spike Recovery (%):** 91 | | | |

These results display a similar trend as the initial measurements, though at much lower concentrations. The reported blank data concentration is reported as being below the instruments

detectable limit, which is well below the maximum limit allowed by ASTM regulations (Table [10]). Meanwhile, the 'Start' sample still measures well above zero, even as the sample is composed only of digested DI water. The spike recovery shows a small percent loss, but still does not create a standard deviation high enough to accommodate for the values seen in Table [9]. The precent increase between the results shown in Table [9] relative to those in Table [10] are displayed in Table [10]. Though the trends are similar, the percent error inconsistencies do not suggest the elevated levels detected by the PerkinElmer 4300 DV ICP-OES are explicitly due to differences in calibration blanks. This is further discussed in the ***ICP-OES Troubleshooting*** section below.

As both sets of data display similar trends inconsistent with previously obtained data, error is likely due to experimental error. The implemented digestion method requires extensive modification and handling of the sample, introducing many pathways for error to enter the system. One possible source occurs during HF introduction, through the reaction shown in Equation [5]. If the solution is not cooled according to Method 3030I, the Silicon ions may evaporate off in its gaseous form, causing an overall loss in the silica concentration.

Silica loss results in decreased system efficiency and increased maintenance costs. The modified silica binds with metals to remove them from solution for later recovery. Loss of silica decreases the sorption capacity of the membrane, lessening the treatment affects. Additional time and money would be required to maintain the system if the membrane is unable to retain silica. There would be added silica recovery and replacement costs, as well as more extensive and frequent membrane rejuvenation procedures.

### *4.13 Produced Water Characterization*

The composition of PW varies drastically depending on several factors, including the shale formation it was extracted from and the age of the well. The salinity, minerals, and residual gas

byproduct can be extremely different, thus characterizing a regions PW was an important step in assessing the viability the membrane system.

Samples obtained from PW processing site in southwestern Oklahoma were found to have elevated levels of many elements commonly found in groundwater sources. Selected few elements of focus are listed in Table [11]. The samples were collected at four different points along the treatment train.

Table 11: Select concentrations of elements present in produced water samples. These elements were highly relevant to various aspects of the OCAST project.

| Element | Concentration (mg/L) | | | |
|---|---|---|---|---|
| Lithium | 5.79 | 5.22 | 5.26 | 5.27 |
| Silicon | 5.83 | 4.89 | 12.9 | 2.68 |
| Sodium | 27200 | 41800 | 45200 | 42500 |
| Location: | Trash Tank | Pre-Injection | Injection Pump | Pipeline |

Though the sedimentation treatment system seems to have negligible effects on the sodium concentrations, the sodium levels are relatively low for PW. At high salinities, the flux rates for MD systems decreases as the sodium concentration increases; the levels contained in these PWs might make the system more efficient and effective versus regions where the salinity can measure in the hundreds of thousands.

Lithium, the element being considered in the sorption tests for potential recovery, is found in the PW, though in small quantities. Desalinating the PW and concentrating the contaminant flow may be necessary to recover large enough quantities of lithium and other valuable elements to make it an economically feasible endeavor.

A techno-economic assessment estimating the viability of using MD for PW on a commercial scale calculated treatment costs for MD both with and without waste heat as an energy source (Table [12])[127].

*Table 12: Cost estimate per volume of feed water using a standard energy source and using industry waste heat.*

| System | Total Cost |
|---|---|
| MD | $5.70/m$^3_{feed}$ |
| MD w/ waste heat | $0.74/m$^3_{feed}$ |

These values are used as generalized treatment costs and can be compared to the market value of Lithium and Lanthanum (Table [13]), the two elements analyzed in sorption tests.

*Table 13: Market costs for elements analyzed as potential cost recovery sources for the treatment system.\*

| Element | Market Value |
|---|---|
| Lithium | $118.15/kg |
| Lanthanum | $7.00/kg |

Due to variances in system designs, the cost values in Table [12] are potentially over-estimates for the system proposed in the OCAST project. If 80% of the Lithium from the Pre-Injection pump was recovered by the membrane and sold at market value, it would recover $0.49/m$^3_{feed}$, showing that higher value elements could contribute significantly to treatment cost recovery, depending on the processing and refinement costs. Lanthanum, having a much lower market value, does not offer as much economic benefit though other elements in its periodic series offer more viable market prices. Many of the other elements detected in the ICP scan have a reasonable market value.

Collecting this information showed that there were valuable elements in the PW, and that they could potentially decrease the overall costs of the PW treatment system by a significant margin. Actual viability could not be determined until after the sorption data was analyzed, as the amount of an element that can be recovered is dependent on the silica nanoparticles capacity to absorb it.

If present at a high concentration, silicon present in the PW could potentially interfere with the modified silica attached to the membrane. However, these ICP scans show levels consistent with normal groundwater levels[53], and should cause minimal interference.

The results for the complete ICP-MS results can be found in Appendix [A].

The PW also contained residual petroleum products (Figure [19]). The Hydrocarbon (TPH) Gasoline Range Organics (DRO) and Diesel Range Organics (DRO) tests were conducted according methodologies outlined in Oklahoma Administrative Code § 252:301-9-38[128].
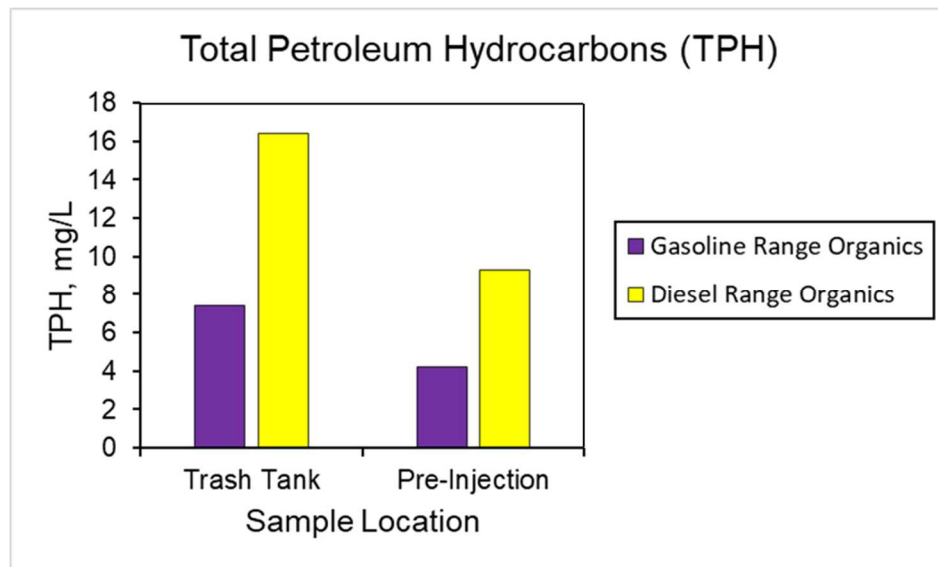


*Figure 19: Hydrocarbon concentrations in produced water samples. Separation of hydrocarbons from the produced water before membrane distillation treatment protects the membrane from increased fouling and decreased flux rates and generates a marketable product.*

As high concentrations of oil damage MD systems and quickly foul the membrane, effective pre-treatment measures must be taken to remove the hydrocarbons. When used before MD, the inorganic membrane used in the membrane system may be able effectively removes almost all residual petroleum. These can then be sold to help offset the cost of the system in addition to the elemental recovery process.

The PW characterization shows the solution is within the parameters of PWs that have been successfully treated using similar techniques in previous studies[51,103]. MD paired with the other treatment mechanisms should desalinate the water enough to be reused as drilling fluids, and potentially even as irrigation waters if technologies are further developed and as state and federal regulations progress.

## 4.14 Silica Sorption Capacity and Rates

The modified silica nanoparticles aimed target various metals and adsorb them out of solution, where they could later be recovered and sold for profit. Sorption tests were conducted to test the capacity of various silicas.

To obtain consistent results, a third-party lab was used run samples on an ICP-MS, using EPA Method 6020. Samples of known concentrations were made using LiCl and $LaCl_3$ salts and DI water (Table [4]) These were sent in for analysis. The known concentrations versus the measured concentrations can be seen in Figure [20]. The discrepancy was used to calculate the standard deviation that is used to account for experimental error. These samples were used to produce the calibration curves for the samples measured in Figures [21] and [22].
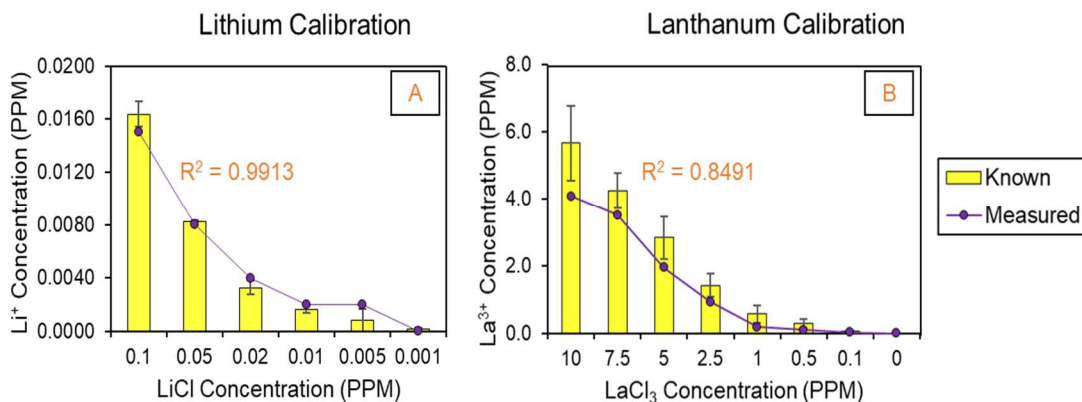


Figure 20: Solutions of known concentrations were sent to a third-party laboratory for ICP analysis. The measured concentrations were generally within the standard deviation calculated using the spike recovery percentage. R2values for the generated calibration curves were above the minimums mandated by EPA Method 3020B.

The calibration curve developed from the measured values yields a high $R^2$ value for Lithium, while the value for lanthanum is significantly less linear. The standard deviation for the lanthanum values was also much larger. However, the results were still accurate enough to give meaningful results for sorption test results. The spike and recovery values for each element was within EPA requirements. Several sorption tests were run with different silica particles that produced varying results. ICP results from a sorption test containing only Lithium in solution can be seen in Figure [21].
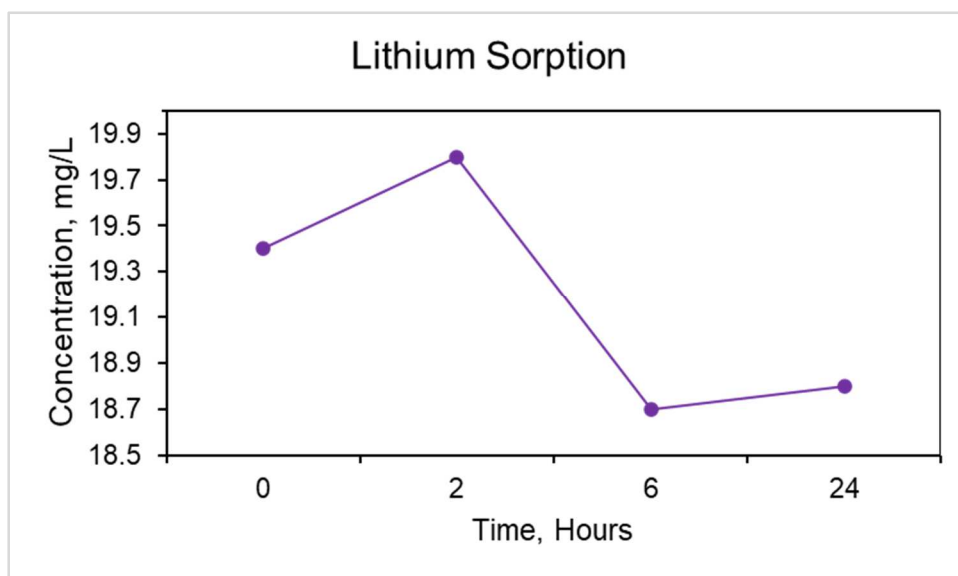


Figure 21: Modified silica nanoparticles were added to an ~20M$^{Li+}$ solution. A sorption test was conducted over a 24-hr period with samples being taken from the solution periodically. ICP analysis of the samples shows minimal reduction in the Li$^+$ concentration over the duration of the experiment.

Lithium concentration consistently remined relatively stable, with minimal removal occurring even over an extended period. Figure [22] shows mixed matrix tests prepared using Lithium, Lanthanum, and Sodium salt. The results were normalized by setting the original 20 PPM concentrations of each ion to 100%, displayed by the dashed orange line, and the columns representing the percent change of the metal ion concentrations after a period of two hours.
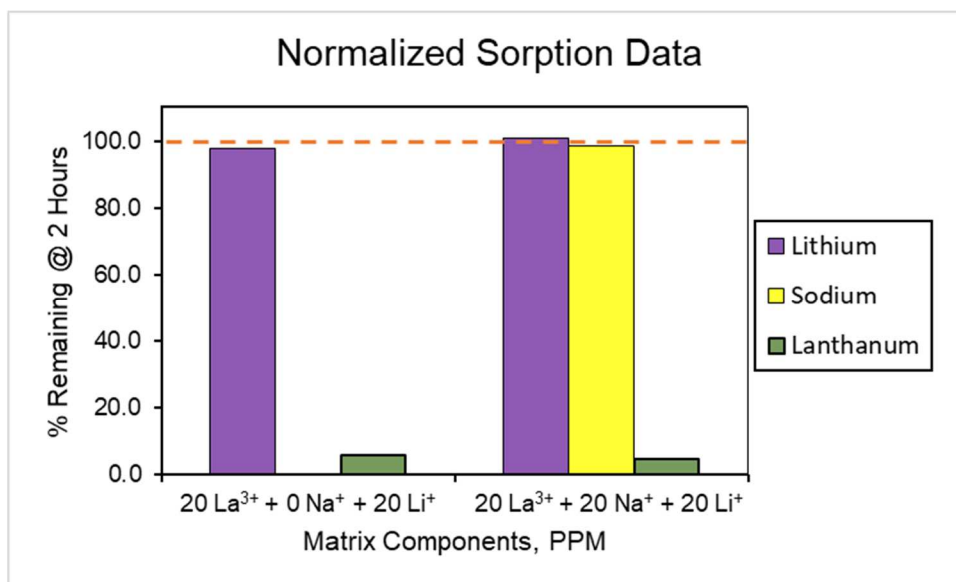
*Figure 22: A sorption test was run with a multi-elemental matrix. ICP result again show minimal decreases in Li⁺ concentrations, which is consistent with previous results. Sodium, another ion with a +1 charge, also had negligible reduction in concentration. Lanthanum has a +3 charge and exhibited significant reduction. The suggests that the silica nanoparticles effectively remove heavier ions from concentration, though it's not effective on lighter elements.*

Lithium removal rates are near zero, consistent with earlier results seen in Figure [21]. Sodium

appears to follow a similar pattern, with only small decrease in the ion concentration being

detected by the ICP. These ions both have a +1 charge and are relatively small and lightweight

molecules. Conversely, Lanthanum is a heavy molecule with a +3 charge. It consistently has a

substantial reduction of concentration in solution in sorption tests. Though the sorption capacity is

low on the smaller ions, it is highly effective on the heavier ion tested. Further testing on

Lanthanum as well as the addition of other heavy metals should be done to better characterize the

nanoparticles' ability to remove the ions from solution.


### 4.15 ICP-OES Troubleshooting

A PerkinElmer Optima 4300 DV ICP-OES was initially used for all ICP data collection, but

recurring hardware problems resulted in untrustworthy data. Common problems commonly

affecting ICP uptime and performance can be sorted into the following categories: poor precision,

carryover, drift, degraded detection limits, accuracy, and sensitivity. The PerkinElmer Optima continues to exhibit many of these issues.

Several system failures and error messages occurred, even when following normal operational procedures, as outline in the SOP developed for the instrument. Appropriate actions were taken to correct problems as they manifested, with major concerns and solutions outlined below.

The instrument began occasionally shutting off during operation, citing the "plasma went out unexpectedly", followed by a list of potential causes. The system was checked for any gas leaks, Nitrogen was added to the system to act as purge gas, and all system parameters were optimized to align with literature. After addressing the suggested solutions and consultation with a local environmental lab, PerkinElmer was contacted to schedule a service visit. Maintenance of the instrument included aligning and cleaning serviceable parts. A buildup of salts on the injector torch was suggested as a possible culprit for the plasma failures and was subsequently cleaned. A cleared spray chamber would eliminate the possibility of poor relative standard deviations (RSD) or carryover problems stemming from a contaminated spray chamber. Removing deposits from the injector torch would again remove this a source of issue.

After the service visit, the plasma ignition problem continued. Furthermore, many of the results that were collected from the instrument had high RSD and weren't reproducible. The ICP also had difficulty creating a calibration curve when too many standard solutions were input as well as if the concentration range was too large, regardless of the fact the these should have been within the range of the instrument.

Figure [23] shows two calibration curves as measured by the PerkinElmer Optima, using the same calibration solutions. Figure [23A] shows the initial standard curve, exhibiting an $R^2$ value of 0.9978 as well as RSD values generally within the 5% tolerance granted by EPA Method 6010D. Samples with reasonably high concentrations of Lithium were measured using the

calibration curve seen in Figure [23], due to high correlation and low RSD of the calibration

(Table [14]). Though the RSD values for all samples were between 3-8%, the measurements were

recorded as being only slightly above the instrument's detection limit. The measurements were

consistent within the set but matched neither the known concentration nor the measurements

taken by the third-party environmental lab. Figure [23B] shows the same calibration set, as

measured one week later. The $R^2$ value suggests minimal linearity, with RSD values ranging

between 47-485%.  These data sets displayed a lack of precision, sensitivity, and accuracy.

Recurring issues of these sorts were the primary reasons results measured by a third-party

laboratory were used for the remaining duration of the OCAST project.
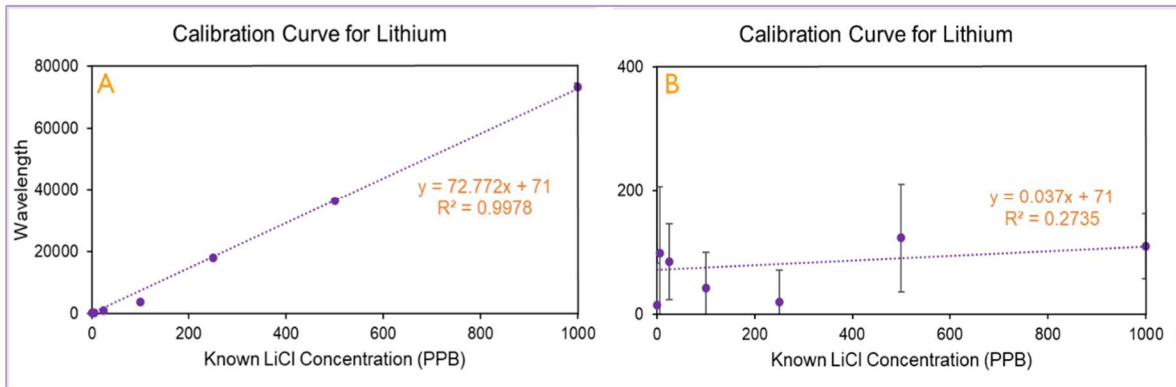


*Figure 23: Two datasets measured by the PerkinElmer Optima and using the same calibration solutions produced drastically different results. Though the curve in [A] met all the necessary requirements as dictated in EPA 6010D to be used for analysis, the reuslts produced by the curve (Table [14]) are incompatible with known data.*

*Table 14: This data was measured using the calibration curve in Figure [23A]. This data is inconsistent with the know concentration and dilutions of the samples and stock solution used, and exhibits some of the recurring issues of the PerkinElmer Optime*

| Sample ID | Concentration (mg/L) | | |
|---|---|---|---|
| | *Known* | *PerkinElmer Optima* | *Third-Party Lab* |
| 20 Li + 10 Na | 3.274 | 0.012 | 3 |
| 20 Li + 20 Na | 3.274 | 0.012 | 3.002 |
| 20 Li + 40 Na | 3.274 | 0.012 | 3.003 |

Further instrumental inconsistencies are seen in the data presented in Tables [9] and [10], located

in the ***Silica Retention on Modified Membrane*** section above. Though the trends are similar, the

percent error inconsistencies do not suggest the elevated levels detected by the PerkinElmer 4300

DV ICP-OES are explicitly due to differences in calibration blanks. In addition to the imprecise

and inaccurate results relative to third-party results and calculated percent differences, the

PerkinElmer Optima also failed to reproduce the initially reported results when remeasured. The

values tended to drift arbitrarily and exhibited continually increasing standard deviations and

RSD values (Table [15]).

*Table 15: The PerkinElmer often yielded data with the necessary quality control boundaries, yet often random values would drift well outside of a reasonable value. At higher ranges, relative standard deviation values should decrease, as the value of the detected wavelengths becomes higher. However, even at high ranges, the RSD values remain relatively high. Moreso, when re-measured, sample wavelengths and concentration proved to be non-reproducible; this fails the quality control tests and voids results.*

| Sample ID | Wavelength | Std. Dev. | RSD |
|---|---|---|---|
| *Calibration Standards* | | | |
| 0 | 71 | 6.54 | 9.21% |
| 5 | 102.76 | 38.95 | 128.40% |
| 50 | 107.48 | 1.81 | 5.02% |
| 100 | 137.06 | 2.11 | 3.15% |
| 500 | 447.12 | 5.28 | 1.40% |
| 1000 | 877.38 | 10.8 | 1.25% |
| *Retentate Samples* | | | |
| 0 | 123777.06 | 2903.2 | 1.83% |
| 1 | 85316.26 | 5489.1 | 5.11% |
| 3 | 22187.54 | 765.21 | 2.75% |
| 5 | 63038.3 | 4492.3 | 5.63% |
| 7 | 67786.38 | 4431.5 | 5.20% |

The poor precision, seen in the high RSD of the samples, was addressed by recalibrating the

detector before each run using the mercury lamp. This reduced the RSDs to less than 5% for most

samples, but there were still high occurrences of drift, degrading detection limits, and accuracy

and sensitivity problems. Literature suggested that these are often consequences of a faulty

sample introduction system. This was addressed by replacing all exterior tubing, which could

have been potentially worn or contaminated, and ensuring the tension on the peristaltic pump was accommodating to a consistent uptake rate. Sample uptake did remain relatively jerky; a worn peristaltic pump may be contributing to poor analysis. With the spray chamber and torch being cleaned, blocked, or corroded RF coils or interface regions could contribute the systems problems. Many of the symptoms of a corroded RF coil align with the issues seen in the PerkinElmer Optima, including degrading and drifting readings, poor accuracy and precision, and premature plasma failure.

The PerkinElmer Optima's inability to produce trustworthy data resulted in the use of third-party contacts to obtain reliable ICP data. Samples are currently being outsourced to a local environmental laboratory that can run appropriately and properly digested samples on ICP-MS, ICP-AES, and ICP-OES instruments. Several laboratories at Oklahoma State University contain ICP sources and could be contacts for future collaborations. ICP-OES sources include multiple laboratories in the Department of Geology. ICP-MS instruments are available through the Department of Civil and Environmental Engineering as well as the Department of Integrative Biology.

**4.2 Application of the Dusty-Gas Model for Prediction of Permeate Flux in a Direct Contact Membrane Distillation System**

*4.21 Simulation Outputs*

MD's high economic potential stems from the system's limited need for a pressure input. With no externally applied back pressure, the pressure exerted on the membrane surface is primarily due to hydrodynamic conditions of the system. These conditions are represented for a given set of conditions via the empirical flux value output by the model. Figure [24] shows a high positive correlation between flux and pressure values.
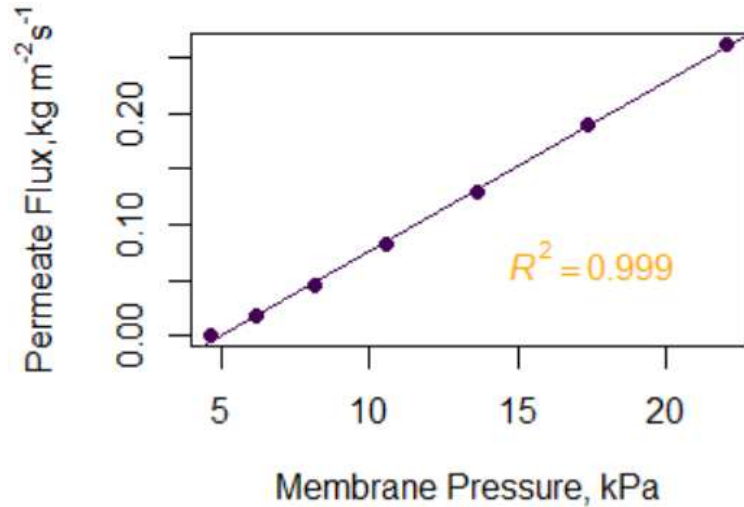
*Figure 24: The relationship between Membrane Pressure and Permeate Flux; membrane pressure and Flux rates were recorded at constant feed and permeate velocities of 0.1754 m/s, a constant bulk permeate temperature of 30˚C, and a bulk feed temperature range of 30-90˚C.*

This is in accordance with Equation [10], which demonstrates an increase in vapor pressure as membrane temperature increases. Membrane temperatures (Equations [14]-[15]) are directly impacted by input flow velocities. Higher system efficiency is observed when the membrane pressure is higher. Optimizing the input variables will yield a higher membrane pressure, and a higher permeate flux. Adjusting the model inputs for various temperature and velocity profiles allow for the subsequent flow to be assessed.

The velocity profile was constructed with a set of flowrates ranging from 0.75 to 2.25 m³/s. Using an inner diameter tubing size of 3/8 in., the velocity range was calculated to be 0.1754-0.2563 m/s. Figure [25] displays the permeate flux at various feed and permeate velocities. Feed temperatures ranging from 40-80˚C (Figure [26A]) and permeate temperatures of 0-40˚C (Figure [26B]) were used to observe the permeate flux rates over a range of input temperature differences.
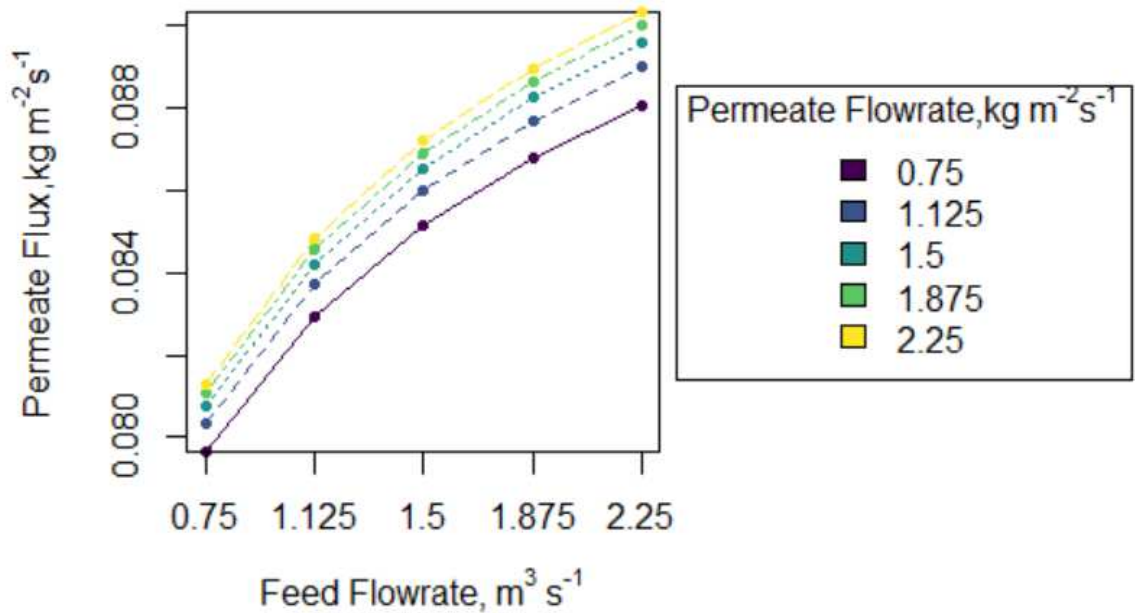
*Figure 25: The effects of the flow rate on the permeate flux. The bulk permeate, and feed temperatures were 30 and 70˚C, respectively.*

Increasing the velocity to either the feed or permeate flow does increase the flux, but the percent increase between the lowest and highest energy inputs is only 12%. The increase can be attributed to an increase in turbulence in the feed channel. This is consistent with the larger observed flux increase attributed to a feed velocity increase verses a permeate velocity increase. Turbulence can be further accentuated with the addition of a spacer, which has been modeled within DGM for MD[22,116].
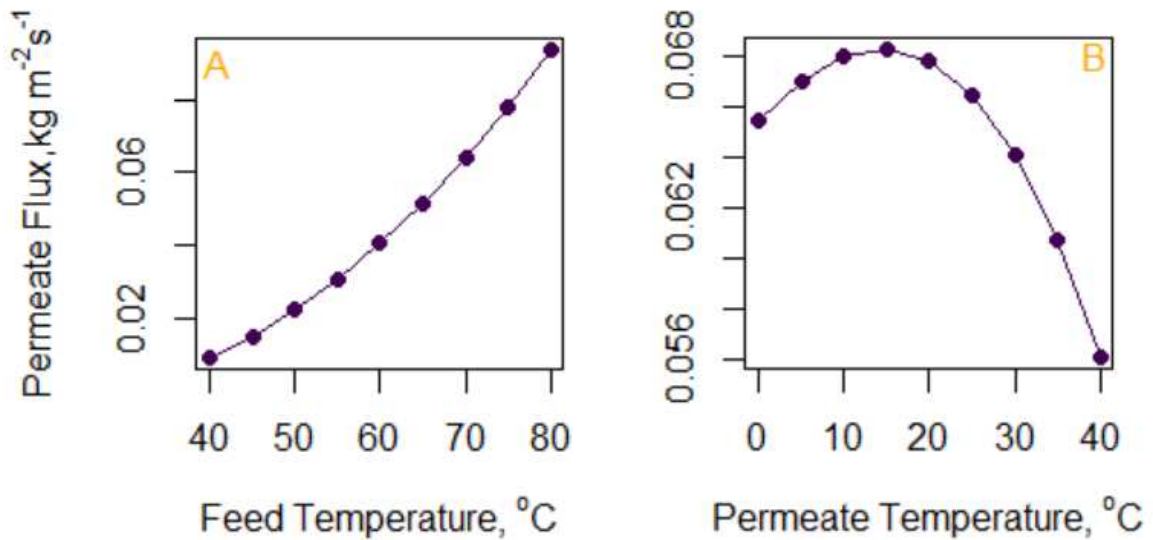
*Figure 26: [A] the effect of feed temperature on the permeate flux; permeate temperature remained at a constant 30˚C, [B] permeate temperature effects on permeate flux; feed temperature was 70˚C.*

Figure [26A] shows a flux increase in response to an increase in feed temperatures. The flux increase happens consistently and in increasing increments as the temperature difference grows larger, in accordance with the Antoine equation, used in Equation [10]. This contrasts with Figure [26B]. This graph does not grow infinitely larger with an increase in temperature difference. It shows there is an optimized permeate temperature of about 15˚C, corresponding to a temperature difference of 55˚C. This optimized temperature difference corresponds to literature[89] and can be further observed at broader temperature ranges in Figure [27]. The highest flux range for given data set is consistently a 40-60˚C temperature range. At high temperatures, the flux rates are seen to decrease as the model calculates the flux values at the highest temperature gradients. This may be due to the limiting flux phenomenon seen in pressure driven membrane systems, where a maximum flux value is reached, even as transmembrane pressure continues to increase[129]. Other factors – velocity, membrane characteristics, environmental factors, etc. – can still improve flux values after the temperature values are optimized. However, as demonstrated, the these factors increase the flux at a slower rate than temperature gradient increases and leave the membrane more susceptible to fouling and wetting[114].
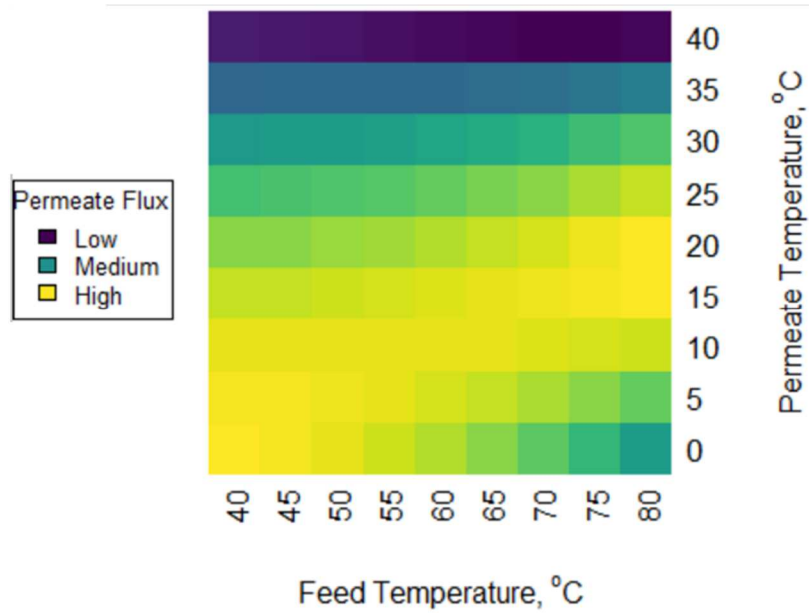
*Figure 27: Heatmap showing relative flux rates over a range of feed and permeate temperatures. The data was normalized along columns. The lowest values were less than 0.002 and the highest values were over 0.09 (kg m$^{-2}$ s$^{-1}$)*
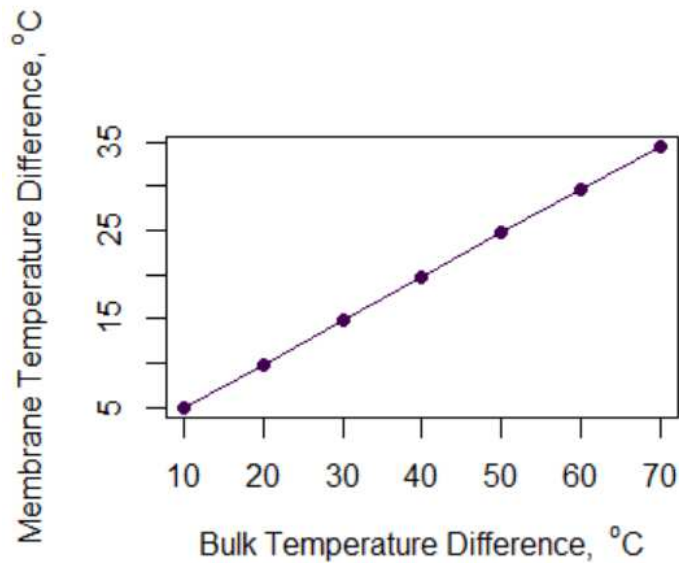


*Figure 28: An increase in the bulk temperature difference directly corresponds to an increase in the membrane temperature difference, increasing mass transfer rates.*

Due to the properties of a DCMD system, higher temperature differences of the feed and

permeate solutions lead to an increase in heat transfer across the membrane (Figure [28]). A

stable temperature gradient is important for the predictable and efficient operation of a DCMD

system[89]. Moreso, in addition to the feed and permeate pumps, the heating and cooling of the input solutions are the most energy-intensive part of DCMD operation. Minimizing these costs even by small margins can drastically improve system economics, making careful temperature selection and management important[130]. To further verify selected input variables for full-scale systems, cost analysis should be conducted to estimate capital and recurrent system costs under variable conditions[131].

## *4.22 Model Validation*

Input variables from a published MD experiment[123] were used to run the developed model. The model outputs, seen in the predicted flux column of the table in Figure [29], were graphed against the experimentally obtained flux rates as reported in the journal. This graphical output can be seen in Figure [29].



| Feed Temperature, °C | Predicted Flux, kg m$^{-2}$h$^{-1}$ | Experimental Flux, kg m$^{-2}$h$^{-1}$ |
|---|---|---|
| 40 | 13.23925 | -- |
| 45 | 19.28969 | 21 |
| 50 | 26.81968 | -- |
| 55 | 36.07749 | 37 |
| 60 | 47.34836 | 49 |

*Experimental data for Model Validation was obtained from Andrjesdóttir et al., 2013
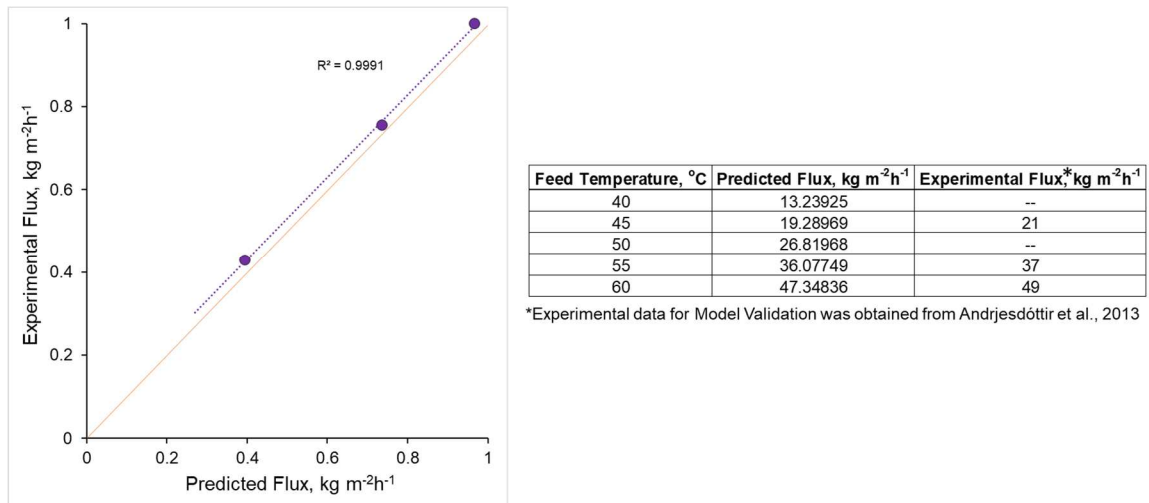
*Figure 29: Experimental results are graphed against predicted flux results that were modeled using identical parameters relative to the experimental environment. Normalizing the values to a factor of one allows the graph to be used to visually interpret the integrity of the model. The results above suggest the model slightly under-predicts real-world values.*

The model and experimental results yield a correlation coefficient of 0.999. The deviation of the data set from the 1:1 ratio line suggests the model consistently under-predicts for all temperature ranges input. The predicted flux versus experimental flux values shown in the table were all

within a 5% margin of error. Similar trends were also present when permeate temperature and flow velocities were varied. This suggests the modified DGM can be useful in predicting permeate flux values when the system is of high-quality and exhibits low temperature and velocity fluctuations.

To test the modification to the membrane pressure calculations added to account for feed solutions with high salt concentrations, results were obtained from a research project using raw PWs as feed solutions. The experimental flux, predicted flux, and the TDS of the solution are shown in Figure [30].



| Data Point | TDS (mg/L) |
|---|---|
| A | 222.6 |
| B | 235.1 |
| C | 140.8 |
| D | 33.3 |
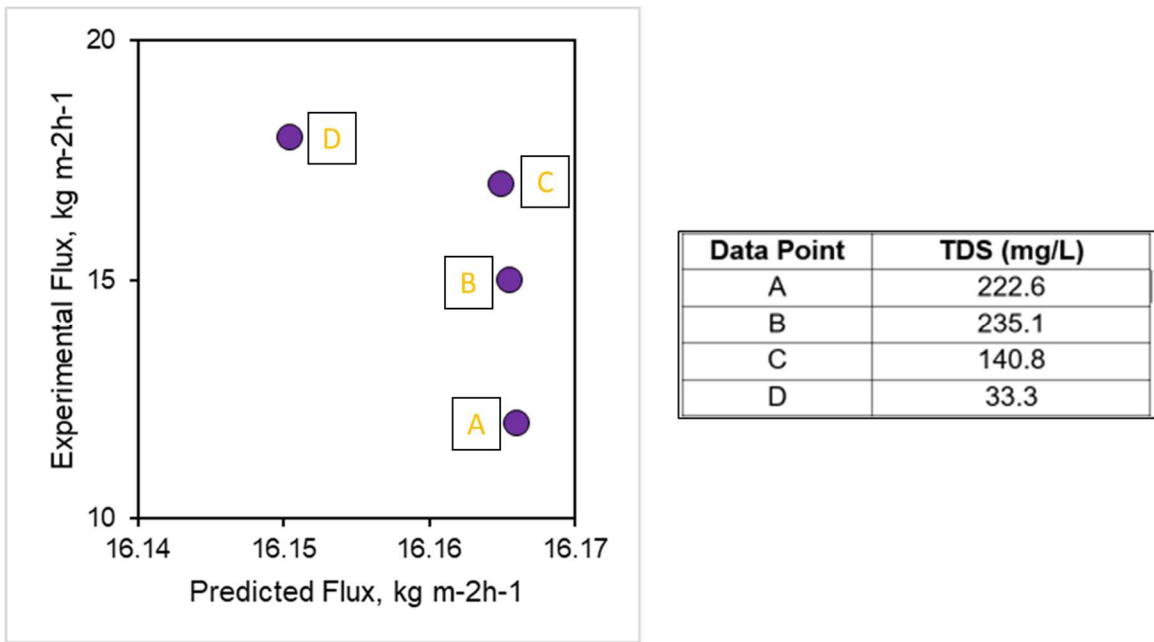
*Figure 30: The membrane pressure parameters in the developed model were modified to account for high salinity fee solutions, as recommended by multiple published sources. Though the salinities of the solutions in the table above varied greatly, the predicted flux values remained relatively constant and did not align with experimental data. The model may need to be further adjusted to better account for highly saline feeds.*

Though the model predictions were all still within reasonable margin of error for the predicted flux – citing a value of around 16 with experimental data displaying results between 12 and 18 – the model poorly accounted for salinity. The experimental results showed higher rates of flux for data point D, which correlates to the relatively low TDS concentration. The model predicted the

lowest flux in the data set for this point, though only marginally lower than other points. A lack of accuracy on this parameter is a weak point for the model. Adjusting the equations to accurately account for highly saline feeds would improve the model's useability for PW applications.

## 4.3 Direct Contact Membrane Distillation for the Treatment of Produced Waters

The data sets below show experimental values obtained from the MD system using various feed solutions, under similar operating conditions. Flux values obtained from the modified DGM are compared to experimental values.

The flow velocities of the feed and permeate pumps remained constant between experiments. Both pumps were set to their maximum velocities. The flowrates ($v_i$) for each pump were averaged to the values seen in Table [16] and these were used to estimate for the crossflow velocities of the feed and permeate (Table [17]).

Table 16: Flow velocity conditions for produced water membrane distillation experiments

| Variable | Value, mL/min |
|----------|---------------|
| $v_f$ | 523.3 |
| $v_p$ | 606.4 |

Table 17: Velocity of the feed and permeate solutions, normalized by dividing by the surface area of the membrane (Table [6]).

| Variable | Value, m/s |
|----------|-----------|
| $u_f$ | 0.0314 |
| $u_p$ | 0.0364 |

For the initial experimental set, the system was operated using a 0.489M NaCl feed solution for a period of 81 minutes. The bulk temperatures of the feed and permeate tanks are shown in Figure [31].
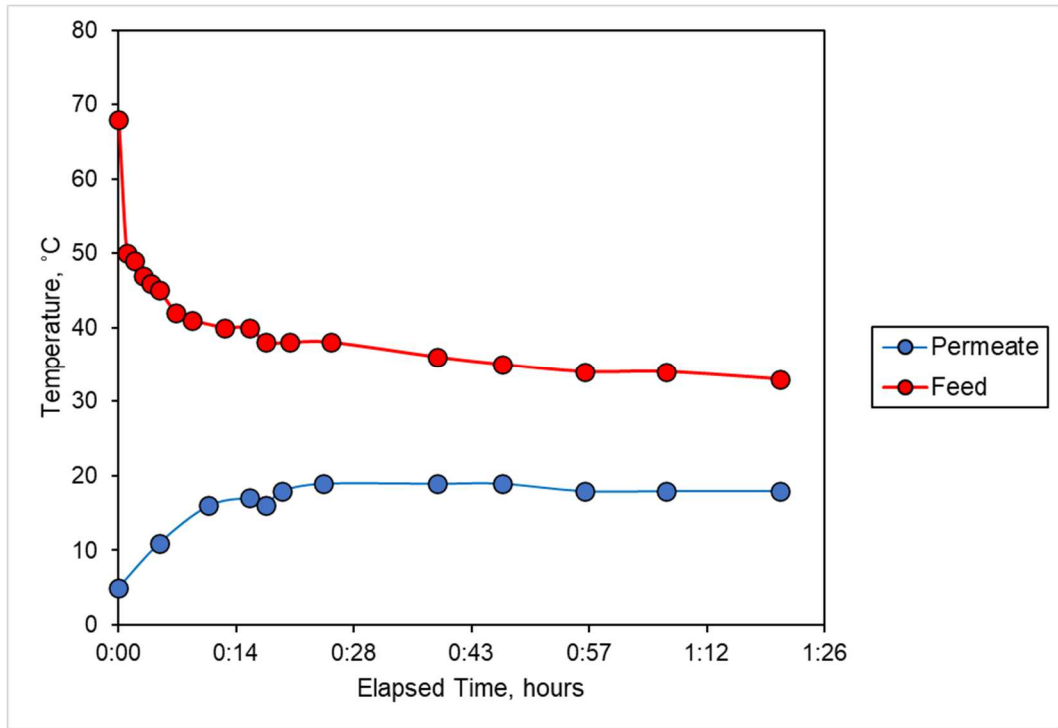
*Figure 31: Temperature profile of the constructed membrane distillation system as reported when using a 0.489$M^{NaCl}$ feed solution.*

Even with temperature maintenance measures in place, heat transfer rapidly occurred across the membrane. Both the feed and permeate temperatures leveled after about 30 minutes, resulting in a bulk temperature difference of around 20˚C. Though some flux should still be observed under these conditions, the rates are extremely low. This can be observed in Figure [27], with one of the lowest predicted flux values occurring at the temperature conditions present at the end of the experimental trial shown in Figure [31].

The change in permeate volume as well as the change in feed volume can be seen in Figure [32].
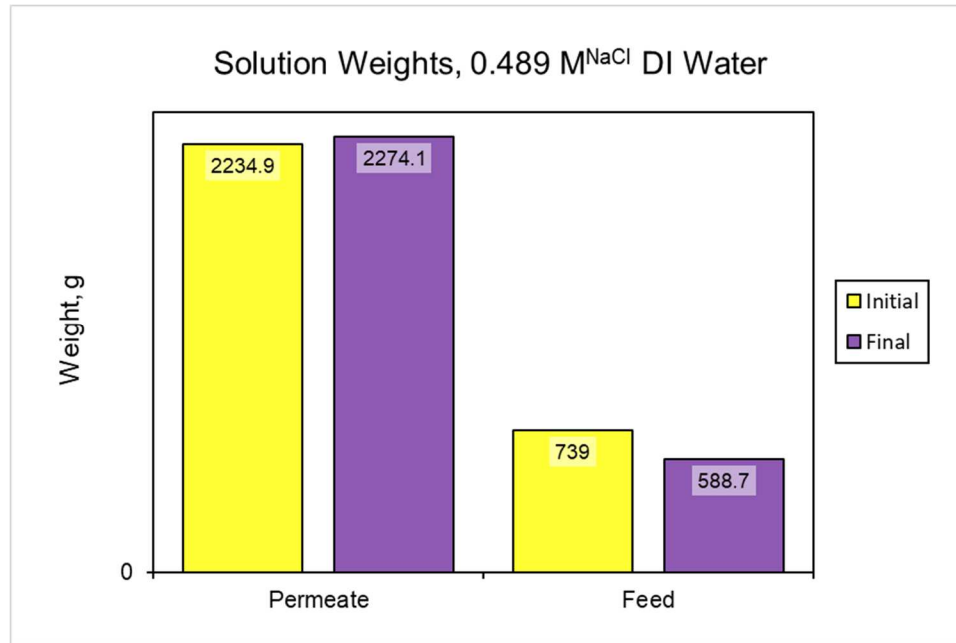
*Figure 32: Initial and final weights of the feed and permeate solutions as recorded when using a 0.489M$^{NaCl}$ feed solution.*

These data points were similarly recorded in subsequent experiments. Two sets of data were collected using PW samples. A cleaner, lighter sample collected from the Pre-Injection (PI) pump was ran first, followed by a rawer sample from the Trash Tank (TT). Figures [33] and [34] show the change in temperature and volumes for these data sets.
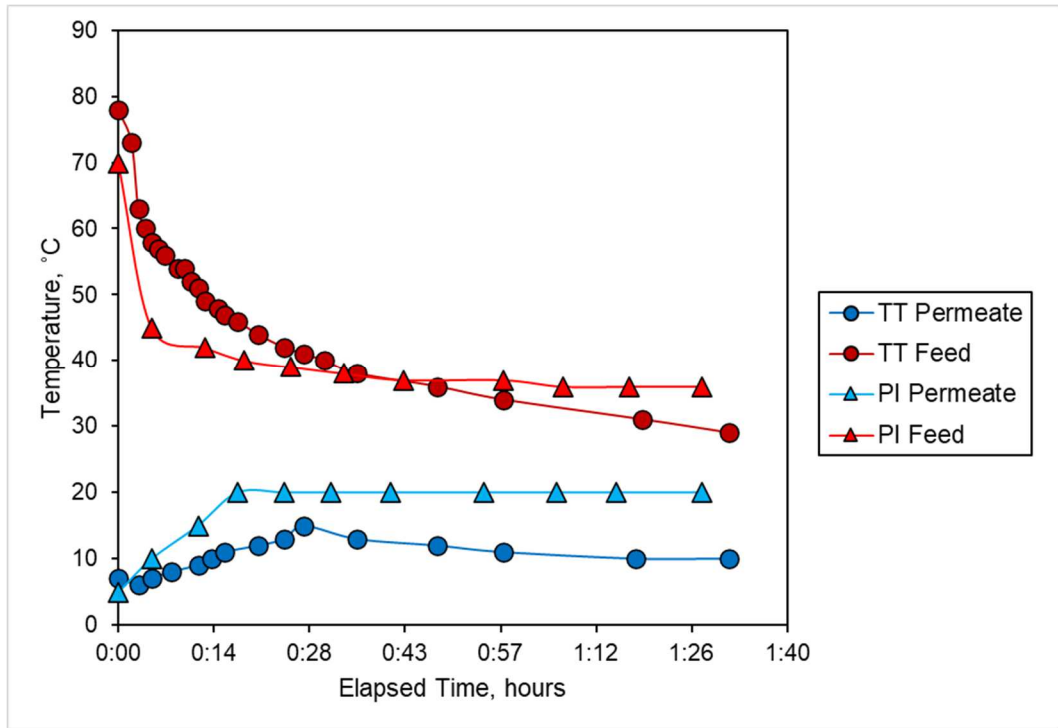
*Figure 33: Temperature profiles for the membrane distillation system when using produced water feed solutions*
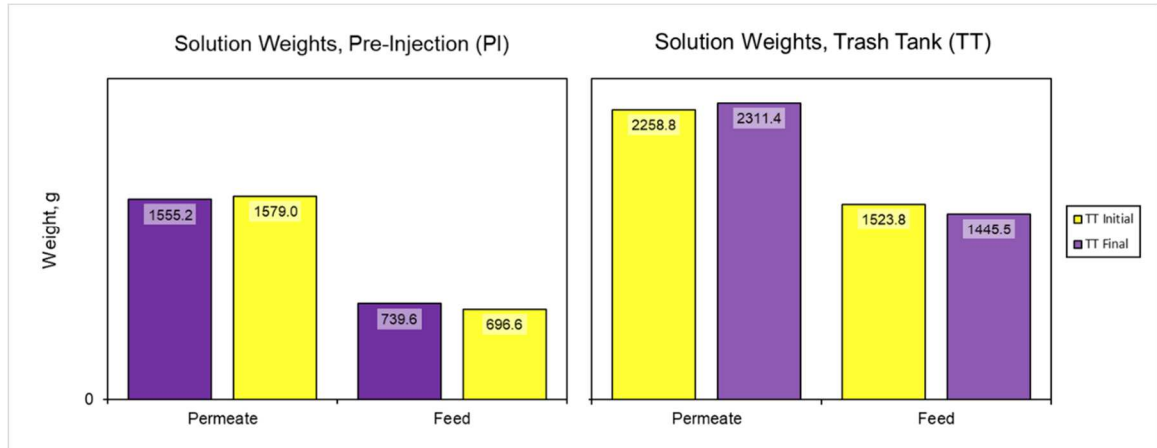


*Figure 34: Initial and final volumes of membrane distillation experiments using produced waters as feed solutions.*

In all three case scenarios, the increase in permeate volume was less than the decrease in the weight of the feed solution. Some discrepancy exists due to significant evaporative losses occurring on the feed side of the membrane. To help quantify these losses, a subsidiary experiment was conducted by heating covered 1000-mL flasks with ~800-mL of water to 75˚C in

the incubator. The flasks were then unsealed and left in the incubator for 90 minutes. The volume

loss ranged from 30-50-mL of water. Though not a perfect representation of the MD system

conditions, this helps account for the excess volume loss in the MD experiment.

Contaminant deposits on the membrane were considered as another potential source for the

weight discrepancy. For the experiment conducted with Pre-Injection feed water, the membrane

was weighed before and after experimentation; the measurements were recorded in Table [18]. It

shows only a marginal weight increase.

Table 18: Initial and final weights for a membrane used during membrane distillation experimentation. The small weight increase suggests low amount of membrane fouling. The losses only slightly help account for permeate volume loss in the system.

| Final: | 2.0-g |
|---|---|
| Initial: | 1.2-g |
| Difference: | 0.8-g |

Though this doesn't help equalize the feed side loss in the system's mass balance, the minimized

contamination does suggest the hydrophobic properties of the membrane allow minimal

contamination and a resistivity to fouling. Table [19] shows conductivity measurements taken

from initial and final feed and permeate samples to test for system efficiency.

Table 19: Conductivity measurements of initial and final solutions of membrane distillation (MD) experiments. Conductivity can be used to estimate treatment effectiveness of the MD system.

| Sample | Initial Conductivity, µS/cm | Final Conductivity, µS/cm |
|---|---|---|
| 0.489M$^{NaCl}$ Feed | 41565 | 41863 |
| 0.489M$^{NaCl}$ Permeate | 2347 | 2356 |
| Pre-Injection Feed | 60775 | 60789 |
| Pre-Injection Permeate | 2387 | 2382 |
| Trash Tank Feed | 39610 | 39643 |
| Trash Tank Permeate | 2321 | 2329 |

The consistent electrical conductivity measurements in the permeate flows show minimal salt

breakthrough of the MD membrane while the increased conductivity in the feed solutions show a

high salt rejection rate by the membrane. These levels were maintained even as the feed solution

purity decreased. Stereomicroscope imaging was used to observe fouling of the membranes operated with various feed matrices (Figure [35]).
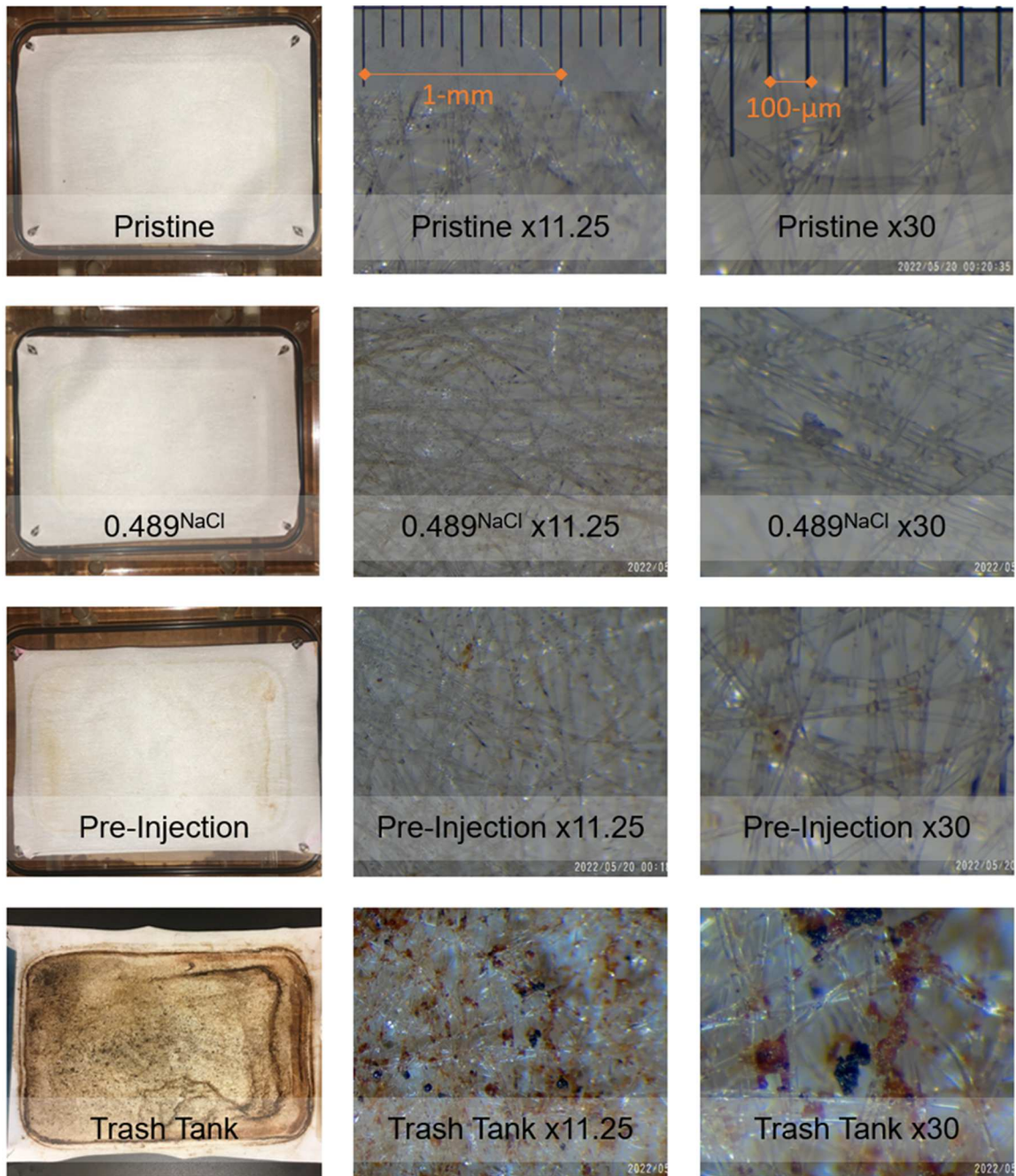


*Figure 35: Images of membrane distillation membranes. The column 1 shows an image taken at normal resolution, columns 2 and 3 are taken with a stereomicroscope at x11.25 and x30 resolutions. Increased fouling can be observed as the complexity of the feed solution matrix increases as the rows go down.*

Increasing amounts of membrane contamination can be observed as the complexity of the feed solution matrix increases. Assuming 100% conversion of the Sodium ion concentrations for the PW feed solutions (Appendix A) to Sodium chloride, the molarity of NaCl was calculated as $0.715M^{NaCl}$ and $0.465M^{NaCl}$ for the Pre-Injection and Trash Tank waters, respectively. Though this is an underestimate of the total salinity of the PW, it seems that the petroleum byproducts (Figure [19]) present in the PW samples affect the membranes more than dissolved salts. While the residual deposited on the $0.489M^{NaCl}$ feed solution membrane appears to be in almost-new condition, with only a few salt crystals visible when zoomed in, the Trash Tank membrane is coated in visible sludge; NaCl concentrations for both feed solutions are comparable. The Pre-Injection membrane, exhibiting a much higher than salinity than the others, has visible contamination that lies between the other sets of data.

The changes in permeate volume (Figures [31] and [33]) and the cross-sectional area of the membrane found in Table [6] were used to calculate the experimental flux for the datasets, shown in Table [20].

Table 20: Experimental flux values calculated from the change in permeate volume and the cross-sectional area of the membrane using Equation [8].

| Dataset ID (Molarity$^{NaCl}$) | Permeate Flux, kg m$^{-2}$h$^{-1}$ |
|---|---|
| $0.489M^{NaCl}$ DI Water | 127.69 |
| Pre-Injection ($0.715M^{NaCl}$) | 58.50 |
| Trash Tank ($0.465M^{NaCl}$) | 123.66 |

The modified DGM model used to model the MD system associates decreased flux rates with increases in salinity, as well as with decreases in the temperature gradient. These values are representative of this. The permeate flux of the $0.489M^{NaCl}$ DI Water solution and Pre-Injection solution are lower than the Trash Tank solution. The more saline Pre-Injection solution has a lower flux rate, even with very similar experimental conditions as the $0.489M^{NaCl}$ DI Water solution.

This data supports published conclusions citing the detrimental effects of hydrocarbons on membrane technologies and emphasizes the importance of an effective pre-treatment. Failure to remove hydrocarbons from the system seems to drastically decrease time to fouling and would increase the maintenance and operation costs associated with an industrial-scale MD system. It may also be beneficial to decrease the salinity of the feed solution during pre-treatment, as even under conditions conducive to faster fouling rates, the lux rates still seem to remain higher due to the relatively low salt concentration.

### 4.31 Model Analysis of Experimental Data

The experimental flux rates reflect the models' assumption that flux is dependent on salinity and a maintained temperature difference. Using the membrane and cell geometries and the operating conditions and temperatures recorded during experimentation, the DGM modified to account for saline feed solutions can be used to predict theoretical pressure and flux rates for each data set. These were compared to the experimental flux values to help pinpoint and calculate experimental errors. The manufacturer provided the membrane thickness and porosity values as a range of values (Table [6]). The values, ranges, and incurred uncertainties as used for the flux predictions are listed in Table [21]. The predicted flux rates over time are in Figure [36].

Table 21: Thickness and porosity values used for the model input. The range of values provided by the manufacturer was used to calculate the amount of error potentially introduced into the system due to variability between membrane batches.

| Symbol | Value | Uncertainty |
|--------|-------|-------------|
| $\delta$ | 180-μm ± 50-μm | 33% |
| $\varepsilon$ | 77.5% | 9.67% |

## Predicted Flux Rates
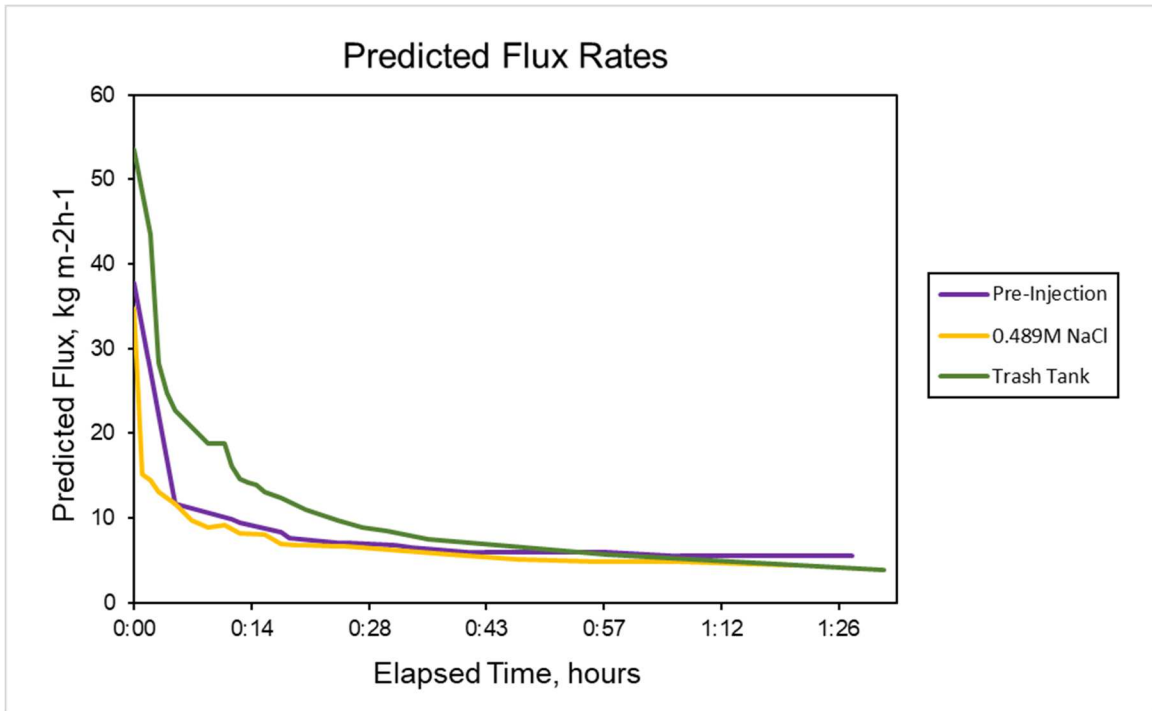


*Figure 36: Flux rates predicted by the model using the same input conditions as the experimental datasets*

There is a large discrepancy between the experimental data and the predicted flux. An averaged permeate flux values was calculated by estimating the area under the curve and dividing by the operational time (Table [22]). This is then converted to the expected increase in permeate volume the model predicts there to be during the operational period, which is seen relative to the experimental volume increase in Figure [37].

*Table 22: Calculated predicted permeate flux volume for membrane distillation experiments.*

| Dataset ID | Predicted Flux, kg $m^{-2}h^{-1}$ |
|---|---|
| 0.489M[NaCl] DI Water | 6.63 |
| Pre-Injection | 7.75 |
| Trash Tank | 14.42 |
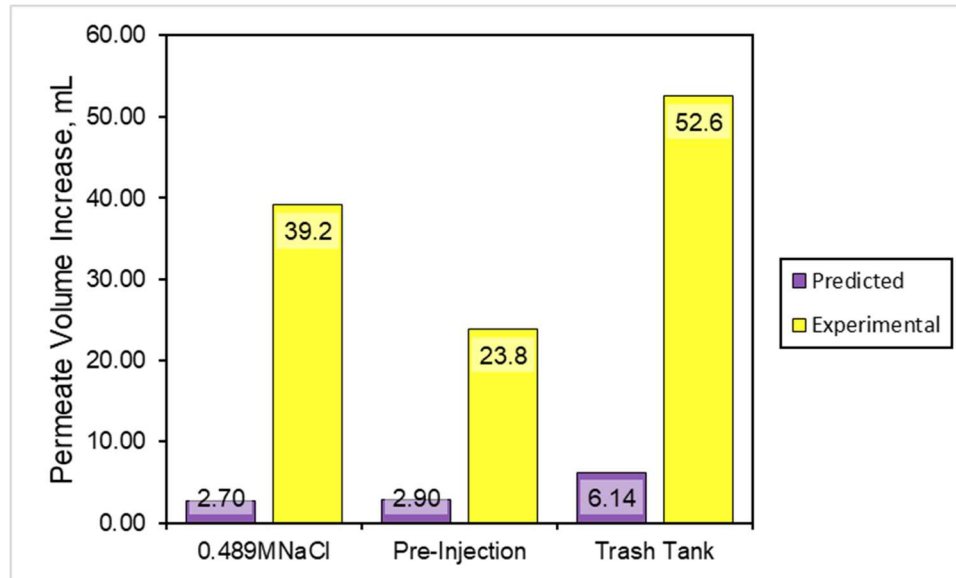
*Figure 37: Predicted flux rate and experimental flux rates. Experimental error and model uncertainty may account for the large discrepancies between the experimental and modeled results.*

All the predicted datasets have significantly lower flux values than measured in their

experimental counterparts. Like the experimental data, the predicted data shows similar trends for

the NaCl and Pre-Injection datasets, while the Trash Tank data set is higher. This reasonably

corresponds to the higher initial temperature difference and slower heat transfer observed during

this trial. Equations [30]-[32] were used to calculate the error in the modeled results, which are

printed in Table [23].

*Table 23: Model evaluation was quantified using the following parameters. Due to the large discrepancies in the experimental and permeate flux values, the model evaluation suggests the model isn't relevant to the datasets.*

| Dataset ID | RMSE, % | ME | Error, % |
|---|---|---|---|
| 0.489M$^{NaCl}$ DI Water | 74.8 | -42.72 | 93.1 |
| Pre-Injection | 61.32 | -11.48 | 87.8 |
| Trash Tank | 91.21 | -532.86 | 88.3 |

The model exhibited extremely high error and regression rates. Though there are known sources

of error in the model – most notably discrepancies in membrane permeability and thickness – it

was previously determined that the model performs reasonably well when modeling published

datasets. The numbers predicted by the model also align reasonably well with experimental

results published in literature. Much of the variation between the numbers may be due to experimental faults. Condensation, pipe volume loss, and air in the system may have all increased the volume in the permeate tank, resulting in an artificially high flux rate. Implementing a better permeate flux measurement and supervision procedure would prevent large increases or decreases occurring at the beginning or end of operation from impacting the overall results. Implementing better temperature regulation systems and optimizing the system per the recommendations of the developed model would further help prevent errors and inefficiencies. Regardless of the discrepancies, both the model and experimental results suggest that MD distillation can successfully be employed for the treatment of saline waters and PW.

CHAPTER V

CONCLUSION

## 5.1 ICP Analysis for Testing Membrane Technologies

ICP analysis was an over the duration of the OCAST project. Multiple ICP technologies were used, with the instrument of best fit being selected based on sample matrix and digestion method.

- The sorption tests digested with this *Standard Methods* Method 3030E showed promising results regarding the uptake of metals from solution, but only for heavier ions. While Lanthanum showed significant reduction in solution concentration, Lithium and Sodium ions were constant (Figure [22]). This sorption method has the potential to be implemented industrially to remove and recover heavier metals from wastewater solutions. For the removal of lighter metals, other methods should be researched. Experiments should be conducted using more complex solutions to determine the sorbents capacity and ability to selectively remove certain ions.

- ICP analysis of PW samples measured amounts of profitable element at levels potentially high enough to economically recover. Concentration or crystallization of the feed solution using MD could increase the recoverability of the compounds, improving profitability. High petroleum byproducts were also detected in PW samples. Adequate pretreatment by the proposed initial membrane is necessary to prevent excess fouling and maintenance costs associated with the MD system.

**5.2 Application of the Dusty-Gas Model for Prediction of Permeate Flux in a Direct Contact Membrane Distillation System**

System optimization requires compromise between maximized flux rates and operational parameters that are sustainable. To make an MD system a beneficial treatment technology, system inputs should be maintainable, environmentally, and economically sustainable, and highly efficient. Outputs from the model yield several key conclusions consistent with theory and previously published literature:

- MD is a pressure driven system—Though the system is not manually pressurized, the transmembrane pressure created by the pressure gradient is the driving force for permeate flux. The permeate flux (Equation [8]) and membrane transfer coefficient (Equation [20]) both exhibit a strong reliance on membrane pressure variables. Figure [24] demonstrates the permeate flux's reliance on a membrane pressure gradient. This strongly aligns with theory and published experimental data.

- The temperature gradient dictates the transmembrane pressure— As summarized previously, the model demonstrates that flux rates are dependent on the transmembrane pressure gradient. This pressure gradient is dependent on the input temperature difference which is configured within the calculation for partial pressure within the membrane (Equation [19]). The Flux versus Input Temperature graphs (Figure [26]) reinforce this conclusion. When the permeate temperature is maintained (Figure [26A]), the flux rapidly increases as temperature difference grows larger, synonymous with an increase in membrane pressure. When feed temperature is maintained (Figure [26B]), the flux eventually begins to decrease as the difference grows smaller. While easing the negative effects of heat transfer (Equation [9]) initially allow for the flux to increase as the temperature difference closes, the flux rates eventually succumb to the decreased transmembrane pressure as the gap continues to close.

- Optimization of the system requires the optimization of the temperature—Once a membrane has been selected, the most important independently controlled factor for both maximized flux rates and economic sustainability is the input temperatures. Though Figure [33] shows an increased temperature difference linearly correlates to an increased temperature difference across the membrane, larger temperature gradients drastically increase the operational costs as the feed and permeate temperatures must be maintained in the presence of increasing heat transfer rates. Higher heat transfer can also increase temperature variability and uncertainty and, at higher temperature differences, can even negate the effects of a pressure increase, resulting in overall lower flux rates (Figures [28] and [29]).

- For maximum system efficiency, additional parameters should also be optimized. Flowrates and membrane characteristics also affect mass transfer across the membrane. The velocity of the solutions is used to calculate Reynolds number (Equation [10]), and thus has a small impact on the heat transfer rates. The heat transfer rate is used for the calculation of the membrane surface temperatures (Equations [21]-[22]), directly impacting the mass transfer rates (Equation [20]). As seen in Figure [25], an increase in permeate flowrate more drastically improves flux rates. This demonstrates that careful considerations should be made when manipulating input variables for system improvements to achieve maximized efficiency and impact. Membrane characteristics – most notably thickness, material, and pore size – also affect transmembrane flux rates. They play a large role in the heat and mass transfer rates but should be selected based on treatment goals and the matrix of the feed solution.

- When used with data from a high-quality MD system, the model can effectively predict the permeate flux rates of the experimental dataset. Figure [29] shows small margins of error between predicted flux and experimental flux when the model is given adequate input parameters and accurate independent variables.

- The model poorly adapts to saline feeds. The addition of the activity equations should account for the transmembrane pressure increase yet fail accurately do so (Figure [30]). Especially with high matrix solutions such as PW the total dissolved solids in the feed solution can well exceed normal levels. Tuning the model to better accommodate this would increase model usability for PW feed solutions.

## 5.21 Potential Model Additions

A more adaptive and responsive model yields higher quality results more closely attuned with realistic system conditions on a consistent basis. Several additions to the model could be made to make a more robust model better suited for MD treatment of PW:

- Spacers are commonly added to increase the space between the feed solution and the membrane surface to increase turbulence. This can improve flux rates without raising energy costs and offers an economic and ecological way to improve system performance. Accurate modeling of this requires the addition of a model that allows the increase in flow velocity to be calculated[116]. The addition of a spacer also modifies the effective channel height on the feed side, resulting in a change in the hydraulic diameter (Equation [24]) on the feed side. Spacers are also available for the permeate side and serve the same purpose and would purportedly use the same equations.

- Inherit uncertainty exists on many of the input variables for a variety of reasons and, even with near perfect management and maintenance practices, are nearly impossible to minimize to insignificant levels. The option to add uncertainty calculations on membrane thickness, flowrate, and temperature values particularly could improve the usability of the model.

**5.3 Direct Contact Membrane Distillation for the Treatment of Produced Waters**

The bench-scale MD system shows promising results for MD treatment of PW. Both the model and the experiments reported measurable flux rates that would translate well to a full-scale system. Several key conclusions include:

- The heat transfer mechanisms negatively impacted the mass transfer. Figures [31] and [32] show operation of the membrane system rapidly decreasing the temperature gradient across the membrane. The flux rates modeled using these temperature profiles show the flux rates decreasing just as quickly. For the system to work on a commercial scale, the temperatures of both the feed and permeate solution must be closely managed and maintained to perpetrate consistent treatment in an economically efficient manner.

- Increases in feed and permeate tank volumes resulted in the Trash Tank trial experiencing slower heat transfer than previous experiments. The larger the tank volume, the lower the temperature fluctuation and energy cost associated with temperature maintenance should be. Temperature maintenance should be less of a concern in an industrially scaled MD system than the bench-scale system.

- Hydrocarbons increase the fouling rates of the membranes. Even over a short period of approximately 90 minutes, oil and other contaminant deposits was much more visible on the membrane for the dirtier feed solutions. Effective and efficient system performance over a longer period rely on effective oil-and-water separation during pre-treatment.

- The MD system produced effectively treated water. The conductivity measurements on the permeate side were approximately the same before and after experimentation. There appears to be little to no salt breakthrough of the membrane, even as contamination can clearly be seen on the surface of the feed side of the membrane.

The experimental flux rates aren't reinforced by the model's predicted values. Though there may be some amount of error in the model, it likely exists in a larger proportion due to errors occurring during the experimental process (i.e., evaporation and condensation, air bubbles, leaks). Several systems modifications could help remediate these failures, as discussed below.

### 5.31 System Modifications

- The bench-scale system needs better temperature management systems implemented before more effective research can be conducted. A system implementing heat exchangers in addition to chillers or recirculators would drastically improve system performance.

- Placing the permeate tank on a scale would allow for the increases volume to be regularly recorded. With the temperature management system described above in place, the ice bath currently surrounding the permeate tank could be removed, allowing for the permeate tank to be placed on a scale.

Overall, the MD system provided evidence to support its claim as an emerging technology for the treatment of PW. The model developed for the MD system should help optimize the bench-scale system and greatly aid in the development of a full-scale system. The ICP results show the silica-modified membranes can successfully remove certain elements from solutions. This potentially increases the economic benefit of the treatment system as the elements may be able to be recovered and sold for profit. These conclusions support the treatment system proposed in the OCAST project as an economically feasible system that may eventually replace the unsustainable practices currently used to dispose of PW.

REFERENCES

1. Economic Impact of Oil and Gas.

2. U.S. energy facts explained - consumption and production - U.S. Energy
   Information Administration (EIA). https://www.eia.gov/energyexplained/us-energy-
   facts/.

3. EIA-914 monthly production report. https://www.eia.gov/petroleum/production/.

4. Conventional vs unconventional resource - Energy Education.
   https://energyeducation.ca/encyclopedia/Conventional_vs_unconventional_resource
   .

5. Shale Gas 101. *Energy.gov* https://www.energy.gov/fe/shale-gas-101.

6. Wang, Z. & Krupnick, A. US Shale Gas Development: What Led to the Boom? 16.

7. *Fact Sheet*. (2016).

8. US EPA, O. Management of Oil and Gas Exploration and Production Waste. *US
   EPA* https://www.epa.gov/hw/management-oil-and-gas-exploration-and-production-
   waste (2016).

9. Fact Sheet for the Underground Injection Control Program in Arkansas.

10. Clark, C. E. & Veil, J. A. *Produced Water Volumes and Management Practices in
    the United States*. 64 (2009).

11. Neff, J., Lee, K. & Deblois, E. Produced Water: Overview of Composition, Fates, and Effects. in *Produced Water: Environmental Risks and Advances in Mitigation Technologies* 3–54 (2011). doi:10.1007/978-1-4614-0046-2_1.

12. US EPA, O. Unconventional Oil and Natural Gas Development. *US EPA* https://www.epa.gov/uog (2013).

13. Keranen, K. M., Weingarten, M., Abers, G. A., Bekins, B. A. & Ge, S. Sharp increase in central Oklahoma seismicity since 2008 induced by massive wastewater injection. *Science* **345**, 448–451 (2014).

14. Canada, N. R. Rare earth elements facts. https://www.nrcan.gc.ca/our-natural-resources/minerals-mining/minerals-metals-facts/rare-earth-elements-facts/20522 (2018).

15. Peiravi, M. *et al.* A Review of Rare-Earth Elements Extraction with Emphasis on Non-conventional Sources: Coal and Coal Byproducts, Iron Ore Tailings, Apatite, and Phosphate Byproducts. *Min. Metall. Explor.* **38**, 1–26 (2021).

16. Gholz, E. Rare Earth Elements and National Security. 20.

17. Khulbe, K. C. & Matsuura, T. Removal of heavy metals and pollutants by membrane adsorption techniques. *Appl. Water Sci.* **8**, 19 (2018).

18. Kummu, M. *et al.* The world's road to water scarcity: shortage and stress in the 20th century and pathways towards sustainability. *Sci. Rep.* **6**, 38495 (2016).

19. Water for 2060 Produced Water Working Group | Oklahoma Water Resources Board. https://www.owrb.ok.gov/2060/pwwg.php.

20. Dolan, F. C., Cath, T. Y. & Hogue, T. S. Assessing the feasibility of using produced water for irrigation in Colorado. *Sci. Total Environ.* **640–641**, 619–628 (2018).

21. California stakeholders push forward on beneficial reuse - Produced Water Society. https://producedwatersociety.com/california-stakeholders-push-forward-on-beneficial-reuse/.

22. Rao, G. & Li, Y. Feasibility study of flowback/produced water treatment using direct-contact membrane distillation. *Desalination Water Treat.* 1–14 (2015) doi:10.1080/19443994.2015.1119753.

23. Sadrzadeh, M., Hajinasiri, J., Bhattacharjee, S. & Pernitsky, D. Nanofiltration of oil sands boiler feed water: Effect of pH on water flux and organic and dissolved solid rejection. *Sep. Purif. Technol.* **141**, 339–353 (2015).

24. Jepsen, K., Valentin Bram, M., Pedersen, S. & Yang, Z. Membrane Fouling for Produced Water Treatment: A Review Study From a Process Control Perspective. *Water* **10**, 847 (2018).

25. Holman, S. R. & Ohlinger, K. N. An Evaluation of Fouling Potential and Methods to Control Fouling in Microfiltration Membranes for Secondary Wastewater Effluent. *Proc. Water Environ. Fed.* **2007**, 6417–6444 (2007).

26. AlSawaftah, N., Abuwatfa, W., Darwish, N. & Husseini, G. A Comprehensive Review on Membrane Fouling: Mathematical Modelling, Prediction, Diagnosis, and Mitigation. *Water* **13**, 1327 (2021).

27. Membrane Fouling by Natural Organic Matters [NOM]: Hydrophilicity or Hydrophobicity of Surfaces or Something else? https://www.linkedin.com/pulse/membrane-fouling-natural-organic-matters-nom-surfaces-mukherjee.

28. Khayet, M. & Mengual, J. I. Effect of salt concentration during the treatment of humic acid solutions by membrane distillation. (2004) doi:10.1016/J.DESAL.2004.07.023.

29. Shams Ashaghi, K., Ebrahimi, M. & Czermak, P. Ceramic Ultra- and Nanofiltration Membranes for Oilfield Produced Water Treatment: A Mini Review. *Open Environ. Sci.* **1**, (2007).

30. Mueller, J., Cen, Y. & Davis, R. H. Crossflow microfiltration of oily water. *J. Membr. Sci.* **129**, 221–235 (1997).

31. Choudhury, M. R., Anwar, N., Jassby, D. & Rahaman, Md. S. Fouling and wetting in the membrane distillation driven wastewater reclamation process – A review. *Adv. Colloid Interface Sci.* **269**, 370–399 (2019).

32. Gruskevica, K. & Mezule, L. Cleaning Methods for Ceramic Ultrafiltration Membranes Affected by Organic Fouling. *Membranes* **11**, 131 (2021).

33. Nguyen, T., Roddick, F. A. & Fan, L. Biofouling of Water Treatment Membranes: A Review of the Underlying Causes, Monitoring Techniques and Control Measures. *Membranes* **2**, 804–840 (2012).

34. Impact of colloidal interactions on the flux in cross-flow microfiltration of milk at different pH values: A surface energy approach - ScienceDirect. https://www.sciencedirect.com/science/article/pii/S0376738810000955.

35. Role of Specific Ion Interactions in Seawater RO Membrane Fouling by Alginic Acid | Environmental Science & Technology. https://pubs.acs.org/doi/abs/10.1021/es8036498.

36. He, Z. *et al.* The effects of salt concentration and foulant surface charge on hydrocarbon fouling of a poly(vinylidene fluoride) microfiltration membrane. *Water Res.* **117**, 230–241 (2017).

37. Alklaibi, A. M. & Lior, N. Membrane-distillation desalination: Status and potential. *Desalination* **171**, 111–131 (2005).

38. Warsinger: Scaling and fouling in membrane distillation... - Google Scholar. https://scholar.google.com/scholar_lookup?title=Scaling%20and%20fouling%20in%20membrane%20distillation%20for%20desalination%20applications%3A%20a%20review&publication_year=2015&author=D.M.%20Warsinger&author=J.%20Swaminathan&author=E.%20Guillen-Burrieza&author=H.A.%20Arafat&author=V.J.H.%20Lienhard.

39. Meyer, E. E., Rosenberg, K. J. & Israelachvili, J. Recent progress in understanding hydrophobic interactions. *Proc. Natl. Acad. Sci.* **103**, 15739–15746 (2006).

40. Faibish, R. S. & Cohen, Y. Fouling-resistant ceramic-supported polymer membranes for ultrafiltration of oil-in-water microemulsions. *J. Membr. Sci.* **185**, 129–143 (2001).

41. Lekkas, P. T. Applied pilot-scale studies on ceramic membrane processes for the treatment of wastewater streams. https://journal.gnest.org/publication/366 (2013).

42. Mnif, S., Chamkha, M. & Sayadi, S. Isolation and characterization of Halomonas sp. strain C2SS100, a hydrocarbon-degrading bacterium under hypersaline conditions. *J. Appl. Microbiol.* **107**, 785–794 (2009).

43. Mulder, M. *Basic Principles of Membrane Technology*. (Springer Netherlands, 1996). doi:10.1007/978-94-009-1766-8.

44. Feng, X. *et al.* Functionalized Monolayers on Ordered Mesoporous Supports. *Science* **276**, 923–926 (1997).

45. Yang, Y.-X. *et al.* Evaluation of the toxicity of food additive silica nanoparticles on gastrointestinal cells. *J. Appl. Toxicol. JAT* **34**, 424–435 (2014).

46. Barbier, O., Jacquillet, G., Tauc, M., Cougnon, M. & Poujeol, P. Effect of heavy metals on, and handling by, the kidney. *Nephron Physiol.* **99**, p105-110 (2005).

47. Sobolev, D. & Begonia, M. F. T. Effects of Heavy Metal Contamination upon Soil Microbes: Lead-induced Changes in General and Denitrifying Microbial Communities as Evidenced by Molecular Markers. *Int. J. Environ. Res. Public. Health* **5**, 450–456 (2008).

48. Waters, R. S., Bryden, N. A., Patterson, K. Y., Veillon, C. & Anderson, R. A. EDTA chelation effects on urinary losses of cadmium, calcium, chromium, cobalt, copper, lead, magnesium, and zinc. *Biol. Trace Elem. Res.* **83**, 207–221 (2001).

49. Aljerf*, L. & AlMasri, N. A Gateway to Metal Resistance: Bacterial Response to Heavy Metal Toxicity in the Biological Environment. *Ann. Adv. Chem.* **2**, 032–044 (2018).

50. Yantasee, W. *et al.* Functionalized Nanoporous Silica for the Removal of Heavy Metals from Biological Systems: Adsorption and Application. *ACS Appl. Mater. Interfaces* **2**, 2749–2758 (2010).

51. Wang, F. *et al.* Highly-efficient separation of oil and water enabled by a silica nanoparticle coating with pH-triggered tunable surface wettability. *J. Colloid Interface Sci.* **557**, 65–75 (2019).

52. Chen, Y. *et al.* Fabrication of Silica Nanospheres Coated Membranes: towards the Effective Separation of Oil-in-Water Emulsion in Extremely Acidic and Concentrated Salty Environments. *Sci. Rep.* **6**, 32540 (2016).

53. Humans, I. W. G. on the E. of C. R. to. *SILICA DUST, CRYSTALLINE, IN THE FORM OF QUARTZ OR CRISTOBALITE*. *Arsenic, Metals, Fibres and Dusts* (International Agency for Research on Cancer, 2012).

54. Groundwater | Dissolved mineral sources and significance. *Default* https://www.ngwa.org/what-is-groundwater/About-groundwater/dissolved-mineral-sources-and-significance.

55. Global Silica Sand Market Report and Forecast 2021-2026. https://www.expertmarketresearch.com/reports/silica-sand-market.

56. Quartz Crystal (Industrial). 2.

57. Dan Gavriletea, M. *Environmental Impacts of Sand Exploitation.Analysis of Sand Market*. 26 file:///C:/Users/MADELY~1/AppData/Local/Temp/sustainability-09-01118-v2.pdf (2017).

58. Porter, R. L. 'Scarcity' in Economic Theory and Policy. *Soc. Sci.* **40**, 22–30 (1965).

59. Sasan, K., Brady, P. V., Krumhansl, J. L. & Nenoff, T. M. *Exceptional Selectivity for Dissolved Silicas in Industrial Waters using Mixed Oxides*. 19 https://www.osti.gov/pages/servlets/purl/1411608 (2017).

60. Silicon - Element information, properties and uses | Periodic Table. https://www.rsc.org/periodic-table/element/14/silicon.

61. Mollahosseini, A., Rahimpour, A., Jahamshahi, M., Peyravi, M. & Khavarpour, M. The effect of silver nanoparticle size on performance and antibacteriality of polysulfone ultrafiltration membrane. *Desalination* **306**, 41–50 (2012).

62. Lee, J. *et al.* Graphene oxide nanoplatelets composite membrane with hydrophilic and antifouling properties for wastewater treatment. *J. Membr. Sci.* **448**, 223–230 (2013).

63. Mahmoudi, E. *et al.* Enhancing Morphology and Separation Performance of Polyamide 6,6 Membranes By Minimal Incorporation of Silver Decorated Graphene Oxide Nanoparticles. *Sci. Rep.* **9**, 1216 (2019).

64. Pandey, J., Mir, F. Q. & Shukla, A. Performance of PVDF supported silica immobilized phosphotungstic acid membrane (Si-PWA/PVDF) in direct methanol fuel cell. *Int. J. Hydrog. Energy* **39**, 17306–17313 (2014).

65. Sprick, C. G. Functionalization of Silver Nanoparticles on Membranes and its Influence on Biofouling. (2017) doi:10.13023/ETD.2017.331.

66. Ohls, K. & Bogdain, B. History of inductively coupled plasma atomic emission spectral analysis: from the beginning up to its coupling with mass spectrometry. *J. Anal. At. Spectrom.* **31**, 22–31 (2015).

67. Inductively Coupled Plasma Optical Emission Spectroscopy (ICP-OES) Information - US. //www.thermofisher.com/us/en/home/industrial/spectroscopy-elemental-isotope-analysis/spectroscopy-elemental-isotope-analysis-learning-center/trace-elemental-analysis-tea-information/icp-oes-information.html.

68. Principle of ICP Optical Emission Spectrometry (ICP-OES) : Hitachi High-Tech GLOBAL. https://www.hitachi-hightech.com/global/products/science/tech/ana/icp/descriptions/icp-oes.html.

69. Bulska, E. & Ruszczyńska, A. Analytical Techniques for Trace Element Determination. *Phys. Sci. Rev.* **2**, (2017).

70. ICP-OES System and Technologies - US. //www.thermofisher.com/us/en/home/industrial/spectroscopy-elemental-isotope-analysis/spectroscopy-elemental-isotope-analysis-learning-center/trace-elemental-analysis-tea-information/icp-oes-information/icp-oes-system-technologies.html.

71. Boss, C. B. & Fredeen, K. J. Concepts, Instrumentation and Techniques in Inductively Coupled Plasma Optical Emission Spectrometry. 120.

72. Ashdown, R. How to Prevent Common ICP-OES Insturment Problems.

73. Solid-state detector for ICP-OES | Analytical Chemistry. https://pubs.acs.org/doi/pdf/10.1021/ac00057a021.

74. How Does an Echelle Spectograph Work? *Oxford Instruments* https://andor.oxinst.com/learning/view/article/echelle-spectrographs.

75. Association, A. P. H. *Standard Methods for the Examination of Water & Wastewater*. (American Public Health Association, 2005).

76. Silicon (Si) and water. https://www.lenntech.com/periodic/water/silicon/silicon-and-water.htm.

77. Rimstidt, J. D. & Barnes, H. L. The Kinetic of Silica-Water Reactions. https://reader.elsevier.com/reader/sd/pii/0016703780902203?token=B1CDEAD5A1EEDECB8CC41731ED8F2AC58C031623BFEA11D061D16D6A401024A45D42A

93EFBF0A9C7A58AE46E0BFE2D12&originRegion=us-east-1&originCreation=20210707171807 doi:10.1016/0016-7037(80)90220-3.

78. Luo, Y.-R. Bond Dissociation Energies.

79. Multi-Agency Radiological Laboratory Analytical Protocols Manual (MARLAP): Chapter 13 Sample Dissolution. (2004).

80. Viewing ICP-OES. http://www.labcompare.com/347303-Viewing-ICP-OES/.

81. Sarojam, P. ICP-Optical Emission Spectroscopy. 11.

82. Yu, L. L., Fassett, J. D. & Lindstrom, A. P. Determination of Si in Standard Reference Material SRM 295x Silica-on-Filter. *J. Anal. At. Spectrom.* **18**, 738 (2003).

83. CDC | Facts About Hydrogen Fluoride (Hydrofluoric Acid). https://emergency.cdc.gov/agent/hydrofluoricacid/basics/facts.asp (2019).

84. Ricceri, F. *et al.* Desalination of Produced Water by Membrane Distillation: Effect of the Feed Components and of a Pre-treatment by Fenton Oxidation. *Sci. Rep.* **9**, 14964 (2019).

85. Guidance to Evaluate Water Use and Production in the Oil and gas Industry. (2014).

86. Hydraulic Fracturing & Water Stress: Growing Competitive Pressures for Water. *Ceres* https://www.ceres.org/resources/reports/hydraulic-fracturing-water-stress-growing-competitive-pressures-water.

87. *National Pollutant Discharge Elimination System. U.S.C* vol. 33.

88. *Frequently Asked Questions About Recycled Oilfield Water for Crop Irrigation.*

89. Lawson, K. W. & Lloyd, D. R. Membrane distillation. *J. Membr. Sci.* **124**, 1–25 (1997).

90. Qtaishat, M., Matsuura, T., Kruczek, B. & Khayet, M. Heat and mass transfer analysis in direct contact membrane distillation. *Desalination* **219**, 272–292 (2008).

91. Kebria, M. R. S. & Rahimpour, A. Membrane Distillation: Basics, Advances, and Applications. *Adv. Membr. Technol.* (2020) doi:10.5772/intechopen.86952.

92. Schofield, R. W., Fane, A. G. & Fell, C. J. D. Heat and Mass Transfer in Membrane Distillation. https://reader.elsevier.com/reader/sd/pii/S0376738800802872?token=90BE818CD5 98A0E5DEB644E99D308E669E2474725FE45A3EE0A331E59D7A8D09EE8DFC 8B2CBD52C55D2AF72B2FD9D6EC&originRegion=us-east-1&originCreation=20210826180506 doi:10.1016/S0376-7388(00)80287-2.

93. Srisurichan, S., Jiraratananon, R. & Fane, A. G. Mass transfer mechanisms and transport resistances in direct contact membrane distillation process. *J. Membr. Sci.* **277**, 186–194 (2006).

94. Caravella, A. Dusty-Gas Model (DGM). in *Encyclopedia of Membranes* (eds. Drioli, E. & Giorno, L.) 604–605 (Springer, 2016). doi:10.1007/978-3-662-44324-8_1737.

95. Film Theory - an overview | ScienceDirect Topics. https://www.sciencedirect.com/topics/engineering/film-theory.

96. Rezaei, M. *et al.* Wetting phenomena in membrane distillation: Mechanisms, reversal, and prevention. *Water Res.* **139**, 329–352 (2018).

97. Francis, L., Ghaffour, N., Alsaadi, A. S., Nunes, S. P. & Amy, G. L. Performance evaluation of the DCMD desalination process under bench scale and large scale module operating conditions. *J. Membr. Sci.* **455**, 103–112 (2014).

98. Young, T. *A Course of Lectures on Natural Philosophy and the Mechanical Arts*. (Taylor and Walton, 1845).

99. Krzeminski, P., Gil, J. A., van Nieuwenhuijzen, A. F., van der Graaf, J. H. J. M. & van Lier, J. B. Flat sheet or hollow fibre — comparison of full-scale membrane bioreactor configurations. *Desalination Water Treat.* **42**, 100–106 (2012).

100. Al-Khatib, A. An Experimental Comparison of Performance Between Flat Sheet and Hollow Fiber Membrane Modules in Direct Contact Membrane Distillation Systems for Desalination of Seawater. (Qatar University, 2016).

101. Introducing: DCMD Test Cells. https://www.sterlitech.com/blog/post/introducing-dcmd-test-cells.

102. Minier-Matar, J., Hussain, A., Janson, A. & Adham, S. Treatment of Produced Water from Unconventional Resources by Membrane Distillation. 9.

103. Kim, J., Kwon, H., Lee, S., Lee, S. & Hong, S. Membrane distillation (MD) integrated with crystallization (MDC) for shale gas produced water (SGPW) treatment. *Desalination* **403**, 172–178 (2017).

104. Fluoropore Membrane Filter | FGLP14250. https://www.emdmillipore.com/US/en/product/Fluoropore-Membrane-Filter,MM_NF-FGLP14250?ReferrerURL=https%3A%2F%2Fwww.google.com%2F.

105. Membrane Distillation (MD) - Flat Sheet Membranes | Sterlitech. https://www.sterlitech.com/membrane-distillation-md.html?utm_source=google&utm_medium=cpc&utm_campaign=smart-

shopping&wtx=GAW&gclid=Cj0KCQjwsZKJBhC0ARIsAJ96n3UdjoYQIPLvmb9

FYmB-o54hXkGsUp5YExVaeEuIaUtMynpZ_Z6fP8kaArgwEALw_wcB.

106. Kestin, J., Khalifa, H. E. & Correia, R. J. Tables of the dynamic and kinematic

viscosity of aqueous NaCl solutions in the temperature range 20–150 °C and the

pressure range 0.1–35 MPa. *J. Phys. Chem. Ref. Data* **10**, 71–88 (1981).

107. Jouhara, H. *et al.* Waste heat recovery technologies and applications. *Therm. Sci.*

*Eng. Prog.* **6**, 268–289 (2018).

108. Test Method 6010B: Inductively Coupled Plasma-Atomic Emission Spectrometry

(ICP-AES).

109. US EPA, O. Test Method 6010D: Inductively Coupled Plasma-Optical Emission

Spectrometry (ICP-OES). https://www.epa.gov/hw-sw846/sw-846-test-method-

6010d-inductively-coupled-plasma-optical-emission-spectrometry-icp-oes (2015).

110. US EPA, O. EPA Method 6020B: Inductively Coupled Plasma - Mass Spectrometry

(ICP-MS). https://www.epa.gov/esam/epa-method-6020b-sw-846-inductively-

coupled-plasma-mass-spectrometry (2019).

111. Standard Specification for Reagent Water. https://www.astm.org/d1193-06r18.html.

112. R Core Team (2020). — European Environment Agency.

https://www.eea.europa.eu/data-and-maps/indicators/oxygen-consuming-

substances-in-rivers/r-development-core-team-2006.

113. RStudio | Open source & professional software for data science teams.

https://www.rstudio.com/.

114. U. Lawal, D. & E. Khalifa, A. Flux Prediction in Direct Contact Membrane

Distillation. *Int. J. Mater. Mech. Manuf.* **2**, 302–308 (2014).

115. Houghtalen, R., Akan, A. O. & Hwang, N. *Fundamentals of Hydraulic Engineering Systems*. (Pearson, 2016).

116. Gustafson, R. D., Murphy, J. R. & Achilli, A. A stepwise model of direct contact membrane distillation for application to large-scale systems: Experimental results and model predictions. *Desalination* **378**, 14–27 (2016).

117. Rahimpour, M. R., Kazerooni, N. M. & Parhoudeh, M. Chapter 8 - Water Treatment by Renewable Energy-Driven Membrane Distillation. in *Current Trends and Future Developments on (Bio-) Membranes* (eds. Basile, A., Cassano, A. & Figoli, A.) 179–211 (Elsevier, 2019). doi:10.1016/B978-0-12-813545-7.00008-8.

118. *W. Kays, M. Crawford, B. Weigand, Convective Heat and Mass Transfer, fourth ed., McGraw-Hill, Singapore, 2005. - Google Search*.

119. Lee, J.-G. *et al.* Performance modeling of direct contact membrane distillation (DCMD) seawater desalination process using a commercial composite membrane. *J. Membr. Sci.* **478**, 85–95 (2015).

120. Maurer, E. & code), I. E. (iemisc. *hydraulics: Basic Pipe and Open Channel Hydraulics*. (2022).

121. Ni, W. *et al.* Simulation Study on Direct Contact Membrane Distillation Modules for High-Concentration NaCl Solution. *Membranes* **10**, 179 (2020).

122. Ali, E., Hadj-Kali, M. & Orfi, J. Understanding and enhancing the direct contact membrane distillation performance by modified heat transfer correlation. *Can. J. Chem. Eng.* **98**, 2599–2617 (2020).

123. Andrjesdóttir, Ó. *et al.* An experimentally optimized model for heat and mass transfer in direct contact membrane distillation. *Int. J. Heat Mass Transf.* **66**, 855–867 (2013).

124. Cath, T. Y., Adams, V. D. & Childress, A. E. Experimental study of desalination using direct contact membrane distillation: a new approach to flux enhancement. *J. Membr. Sci.* **228**, 5–16 (2004).

125. Smith, J. U. & Smith, P. *Environmental Modelling: An Introduction*. (Oxford University Press, 2007).

126. Microsoft Excel Spreadsheet Software | Microsoft 365. https://www.microsoft.com/en-us/microsoft-365/excel.

127. Tavakkoli, S., Lokare, O. R., Vidic, R. D. & Khanna, V. A techno-economic assessment of membrane distillation for treatment of Marcellus shale produced water. *Desalination* **416**, 24–34 (2017).

128. *DEQ Approved Methodologies. 252:301-9-38* (2008).

129. Chen, V., Fane, A. G., Madaeni, S. & Wenten, I. G. Particle deposition during membrane filtration of colloids: transition between concentration polarization and cake formation. *J. Membr. Sci.* **125**, 109–122 (1997).

130. Zhang, J., Gray, S. & Li, J.-D. Predicting the influence of operating conditions on DCMD flux and thermal efficiency for incompressible and compressible membrane systems. *Desalination* **323**, 142–149 (2013).

131. Macedonio, F. *et al.* Direct contact membrane distillation for treatment of oilfield produced water. *Sep. Purif. Technol.* **126**, 69–81 (2014).

132. Wang, C.-C. On the heat transfer correlation for membrane distillation. *Energy Convers. Manag.* **52**, 1968–1973 (2011).

**Appendix A: ICP Scan of Produced Water Samples**

| Location: | Trash Tank | Pre-Injection | Injection Pump | Pipeline |
|---|---|---|---|---|
| Element | Concentration (mg/L) | | | |
| Lithium | 5.79 | 5.22 | 5.26 | 5.27 |
| Aluminum | -- | -- | 2.54 | -- |
| Antimony | -- | -- | -- | -- |
| Arsenic | -- | -- | -- | -- |
| Barium | -- | 7.9 | 12.9 | 9.17 |
| Beryllium | -- | -- | -- | -- |
| Boron | 77.7 | 42.2 | 44.1 | 44.6 |
| Cadmium | -- | -- | -- | -- |
| Calcium | 2910 | 5970 | 6310 | 5880 |
| Chromium | -- | -- | -- | -- |
| Cobalt | -- | -- | -- | -- |
| Copper | -- | -- | -- | -- |
| Iron | 4.59 | 1.2 | 15.6 | 102 |
| Lead | -- | -- | -- | -- |
| Magnesium | 705 | 1820 | 1960 | 1780 |
| Manganese | 1.76 | 1.72 | 1.81 | 1.4 |
| Molybdenum | -- | -- | -- | -- |
| Nickel | -- | -- | -- | -- |
| Potassium | 454 | 385 | 409 | 410 |
| Selenium | -- | -- | -- | -- |
| Silicon | 5.83 | 4.89 | 12.9 | 2.68 |
| Silver | -- | -- | -- | -- |
| Sodium | 27200 | 41800 | 45200 | 42500 |
| Strontium | 229 | 750 | 783 | 723 |
| Thallium | -- | -- | -- | -- |
| Tin | -- | -- | -- | -- |
| Titanium | -- | -- | -- | -- |
| Uranium | -- | -- | -- | -- |
| Vanadium | -- | -- | -- | -- |
| Zinc | -- | -- | -- | -- |

**Appendix B: Input Nomenclature and Values**

| Membrane Characteristic | Symbol | Value | |
|---|---|---|---|
| Membrane Thickness[a] | $\delta$ | 76-152 | microns |
| Porosity[a] | $\varepsilon$ | 0.9 | -- |
| Thermal Conductivity (PTFE) | $k_p$ | 0.29 | W/mK |
| Thermal Conductivity (air) | $k_g$ | 0.259 | W/mK |
| Thermal Conductivity (membrane)[b] | $k_m$ | 0.0551 | W/mK |
| Radius of Membrane Pores[a] | $r$ | 0.1 | microns |
| Length of Membrane[c] | $L$ | 0.142875 | m |
| Tortuosity[b] | $\tau$ | 1.344 | -- |
| Universal Gas Constant | $R$ | 8.314 | $m^3Pa/molK$ |

| Input Variables | Symbol | Value | |
|---|---|---|---|
| Bulk Temperature (Feed) | $T_{bf}$ | 40-80 | ˚C |
| Bulk Temperature (Permeate) | $T_{bp}$ | 0-40 | ˚C |
| Velocity (Feed) | $u_f$ | 0.1754-0.2563 | m/sec |
| Velocity (Permeate) | $u_p$ | 0.1754-0.2563 | m/sec |

| Characteristics of Water | Symbol | Value | |
|---|---|---|---|
| Density[d] | $\rho$ | [d] | $kg/m^3$ |
| Dynamic Viscosity[d] | $\mu$ | [d] | Pa/s |
| Thermal Conductivity[b] | $k$ | See Equation [5] | W/mK |
| Specific Heat Capacity | $C_p$ | 4184 | J/kgK |
| Molecular Weight | $M$ | 18.0152 | g/mol |

[a] values were provided by the membrane manufacturer[105]

[b] values were calculated algebraically but were not included in the body of the report. See Appendix C for more information.

[c] values were determined experimentally.

[d] values are temperature dependent. *Fundamental of Hydraulics Engineering Systems*[115] or other resources may be used to locate necessary values.

**Appendix C: Model and Output Nomenclature, in Order of Appearance**

| Nomenclature | Symbol | Units |
|---|---|---|
| Water Permeate Flux | $J_w$ | kg/m²s |
| Transition Coefficient | $C_C$ | -- |
| Vapor Pressure Difference | $\Delta P_v$ | Pa |
| Heat Transfer Coefficient | $h$ | -- |
| Nusselt Number | $Nu$ | -- |
| Hydraulic Diameter[a] | $d$ | m |
| Reynolds Number | $Re$ | -- |
| Prandtl Number | $Pr$ | -- |
| Membrane Diffusivity | $PD$ | m²Pa/s |
| Membrane Surface Temperature (Feed) | $T_{mf}$ | K |
| Membrane Surface Temperature (Permeate) | $T_{mp}$ | K |
| Change in Heat of Vaporization | $\Delta H_v$ | kJ/kg |
| Intermediate Variable | $\dfrac{dP}{dT}$ | -- |
| Vapor Pressure Difference | $\Delta P_v$ | Pa |
| Partial Pressure of Membrane | $P_a$ | Pa |
| Knudsen Coefficient | $C_K$ | -- |
| Ordinary Coefficient | $C_D$ | -- |

[a] values were calculated algebraically but were not included in the body of the report. See Appendix C for more information.

## Appendix D: Other Equations

The input values are used within the model to calculate the values necessary for the permeate flux simulation procedure. The membrane's thermal conductivity is modeled using the Equation [33][114] where $K_p$, is the conductivity of the membrane material and $K_g$ is the conductivity of the gas filling the membrane. Typical conductivity values for MD range from 0.04-0.06 W/m*K, which can be used as a logic check point for the model[132].

$$K_m = \varepsilon K_g + (1 - \varepsilon)K_p \qquad [33]$$

An alternative equation commonly employed for the calculation of the thermal conductivity of the membrane is seen in Equation [34][114,116].

$$K_m = \left[ \frac{\varepsilon}{K_g} + \frac{(1 - \varepsilon)}{K_p} \right]^{-1} \qquad [34]$$

Membrane tortuosity is an estimate of the average ratio of the actual flow path through the membrane compared to shortest possible flow path. It was estimated using the correlation defined in Equation [35][93]. The high membrane porosity of the implemented membrane results in a relatively low tortuosity value and improves the overall flux rates.

$$\tau = \frac{(2 - \varepsilon)^2}{\varepsilon} \qquad [35]$$

The hydraulic diameter of the membrane channel is calculated using Equation [36][116]. This value normalized the channel to a "characteristic length" allowing it to be used the same way around pipe would be.

$$d = \frac{2b_{eff}w_{ch}}{b_{eff} + w_{ch}} \qquad [36]$$

where $b_{eff}$ is the effective channel height and $w_{ch}$ is the channel width.

## Appendix E: Membrane Distillation System Components

| Direct Contact Membrane Distillation Materials | |
|---|---|
| *Component* | *Manufacturer and Model* |
| Feed Tank | Pyrex® 2000-mL Erlynmeyher Flask |
| Feed Pump | Masterflex® L/S® 7520-00 Variable Speed Standard Pump Drive with Masterflex® L/S® Model 7035-21 Standard Pump Head |
| Cooling Solution Tank | Pyrex® 2000-mL Erlynmeyher Flask |
| Cooling Solution Pump | Masterflex® Varible Speed Pump Model 7553-30 with Masterflex® L/S® Model 7018-21 Standard Pump Head |
| Concentrate Control Valve | Hy-Lock® 316SS High-Pressure (<6000 PSI) Pressure Relief Valve for 3/8" Tubing + Fittings |
| Cooling Solution Pressure Control Valve | Hy-Lock® 316SS High-Pressure (<6000 PSI) Pressure Relief Valve for 3/8" Tubing + Fittings |
| Concentrate Pressure Gauge | Swagelok® PGC Series Pressure Gauge, 0-100 PSI with 316SS Connection |
| Cooling Solution Pressure Gauge | Swagelok® PGC Series Pressure Gauge, 0-100 PSI with 316SS Connection |
| Concentrate Flow Meter | Blue-White® F-550 Panel Mount Flowmeter, 1-10 GPM |
| Cooling Solution Flow Meter | Blue-White® F-550 Panel Mount Flowmeter, 1-10 GPM |
| DCMD Cell Assembly | Sterlitech Direct Contact Membrane Distillation Cell, Acrylic |
| DCMD Membrane | Sterlitech QL822 Membrane |
| 3/8" Low Pressure Tubing | Generic PTFE Tubing |
| Feed Solution Heater | Fisherbrand™ Isotemp™ Microbiological Incubator + Nalgene® 5-Gal LLDPE Cylindrical Tank with Spigot |
| Cooling Solution Chiller | Generic 5-Gal bucket w/ Ice Bath |

VITA

Madelyn J. Shaw

Candidate for the Degree of

Master of Science

Thesis:     FEASIBILTY STUDY OF ELEMENTAL RECOVERY FROM OKLAHOMA
PRODUCED WATERS USING ADVANCED MEMBRANE
TECHNOLOGIES

Major Field:    Civil Engineering

Biographical:

   Education:

      Completed the requirements for the Master of Science in Civil at Oklahoma State
      University, Stillwater, Oklahoma in July 2022.

      Completed the requirements for the Bachelor of Science in Civil Engineering at
      Oklahoma State University, Stillwater, Oklahoma in May 2020.

   Experience:

      Graduate Research Assistant at Oklahoma State University, Stillwater, Oklahoma from
      July 2020-June 2022

      Graduate Teaching Assistant at Oklahoma State University, Stillwater, Oklahoma from
      January 2021-May 2022

      Undergraduate Research Assistant at Oklahoma State University, Stillwater, Oklahoma
         from August 2018-May 2020

   Professional Memberships:

      Chi Epsilon

      American Society of Civil Engineering